EXCITED STATE ELECTRONIC STRUCTURE, EXCITATION ENERGY TRANSFER, AND CHARGE SEPARATION DYNAMICS IN VARIOUS NATURAL AND ARTIFICIAL PHOTOSYNTHETIC SYSTEMS CONTAINING ZINC AND MAGNESIUM CHLORINS

by

BHANU NEUPANE

M.S., TRIBHUVAN UNIVERSITY, 2003

AN ABSTRACT OF A DISSERTATION

submitted in partial fulfillment of the requirements for the degree

DOCTOR OF PHILOSOPHY

Department of Chemistry
College of Arts and Sciences

KANSAS STATE UNIVERSITY
Manhattan, Kansas

2011

Abstract

This dissertation reports the low temperature frequency domain spectroscopic study of three different natural pigment protein complexes and one artificial antenna system. The main focus of this work is to better understand electronic structure, excitation energy transfer (EET), and electron transfer (ET) dynamics in these systems that could have impact on achieving higher efficiency in future artificial solar cells.

In the first part of this dissertation, electronic structure and EET pathways in isolated intact CP43′ protein complex, which is isolated from Cyanobacterium *synechocystis* PCC 6803 grown under iron stressed conditions, are investigated using low-temperature absorption, fluorescence, fluorescence excitation, and hole-burning (HB) spectroscopies. This work suggests that, in analogy to the CP43 complex of PSII core, CP43′ possesses two quasi-degenerate low energy states, A′ and B′. The various low-temperature optical spectra are fitted considering an uncorrelated EET model. This work suggests that for optimal energy transfer from CP43′ to PSI, the A′ and B′ state chlorophylls belonging to each CP43′ should face towards the PSI core.

The second part of dissertation reports the photochemical HB study on novel Zinc bacterial reaction center (Zn-RC) from *Rhodobacter sphaeroides* and its β-mutant (Zn-β-RC). This study shows that ET in the two samples is similar; however, the quantum efficiency of charge separation in the mutant decreases by 60 %. This finding suggests that the coordination state of the H_A site zinc bacteriochlorophyll does not tune the active branch ET. Simultaneous fits of various optical spectra using experimentally determined inhomogeneity provides more reliable electron phonon coupling parameters for the P870 state of both RC samples.

In the last part of this dissertation, EET in a novel artificial antenna system (ethynyl linked chlorophyll trefoil, ChlT1) is investigated. EET time in ChlT1 is ~2 ps. ChlT1 in MTHF/ethanol glass forms four different types of aggregates, A1-A4. The EET time in A1 and A2 type aggregates slows down only by a factor of 5 and 7, respectively. This study suggests that ChlT1 and its aggregates can be used as efficient antenna systems in designing organic solar cells.

EXCITED STATE ELECTRONIC STRUCTURE, EXCITATION ENERGY TRANSFER, AND CHARGE SEPARATION DYNAMICS OF VARIOUS NATURAL AND ARTIFICIAL PHOTOSYNTHETIC SYSTEMS CONTAINING ZINC AND MAGNESIUM CHLORINS

by

BHANU NEUPANE

M.S., TRIBHUVAN UNIVERSITY, 2003

A DISSERTATION

submitted in partial fulfillment of the requirements for the degree

DOCTOR OF PHILOSOPHY

Department of Chemistry
College of Arts and Sciences

KANSAS STATE UNIVERSITY
Manhattan, Kansas

2011

Approved by:
Major Professor
Ryszard Jankowiak

Copyright

Abstract

This dissertation reports the low temperature frequency domain spectroscopic study of three different natural pigment protein complexes and one artificial antenna system. The main focus of this work is to better understand electronic structure, excitation energy transfer (EET), and electron transfer (ET) dynamics in these systems that could have impact on achieving higher efficiency in future artificial solar cells.

In the first part of this dissertation, electronic structure and EET pathways in isolated intact CP43′ protein complex, which is isolated from Cyanobacterium *synechocystis* PCC 6803 grown under iron stressed conditions, are investigated using low-temperature absorption, fluorescence, fluorescence excitation, and hole-burning (HB) spectroscopies. This work suggests that, in analogy to the CP43 complex of PSII core, CP43′ possesses two quasi-degenerate low energy states, A′ and B′. The various low-temperature optical spectra are fitted considering an uncorrelated EET model. This work suggests that for optimal energy transfer from CP43′ to PSI, the A′ and B′ state chlorophylls belonging to each CP43′ should face towards the PSI core.

The second part of dissertation reports the photochemical HB study on novel Zinc bacterial reaction center (Zn-RC) from *Rhodobacter sphaeroides* and its β-mutant (Zn-β-RC). This study shows that ET in the two samples is similar; however, the quantum efficiency of charge separation in the mutant decreases by 60 %. This finding suggests that the coordination state of the H_A site zinc bacteriochlorophyll does not tune the active branch ET. Simultaneous fits of various optical spectra using experimentally determined inhomogeneity provides more reliable electron phonon coupling parameters for the P870 state of both RC samples.

In the last part of this dissertation, EET in a novel artificial antenna system (ethynyl linked chlorophyll trefoil, ChlT1) is investigated. EET time in ChlT1 is ~2 ps. ChlT1 in MTHF/ethanol glass forms four different types of aggregates, A1-A4. The EET time in A1 and A2 type aggregates slows down only by a factor of 5 and 7, respectively. This study suggests that ChlT1 and its aggregates can be used as efficient antenna systems in designing organic solar cells.

Table of Contents

List of Figures

List of Tables

Acknowledgements

First, I would like to thank all my teachers and mentors at school, college, and work for their advice, and also encouraging me for higher studies.

I am very thankful to my advisor Professor Ryszard Jankowiak for his consistent advice, support, and through input during my graduate study. I am very proud to be one of his first graduate students after he moved to K-state.

I would like to thank Graduate Committee Members Professor Daniel Higgins, Professor Viktor Chikan, and Professor Robert Szoszkiewicz for their valuable suggestions and comments. I also like to thank Professor James Edgar "Chairperson of examining committee" for being easily available for the final exam. I would like to thank all the K-state Chemistry faculty members for their direct/indirect support during my graduate study. I would like to thank Earline Dikeman "Director of Undergrauate Laboratories" for assisting for teaching undergraduate labs, Brenda Luther (Chemical Hygeine Officer) for making aware of all safety related issues, all ladies in Chemistry office for your various help, and technical staffs (Ron Jackson, Tobe Eggers and Jim Hodgson) for fixing various problems in lab.

I am very thankful to "Dr. Jankowiak former group members" especially Dr. Nhan C. Dang (Now in Los Almos National lab) for sharing his lab expertise while working with him during first two years of my graduate study, and Mike Reppert (Now in MIT) who all the times guided me in using his *Spectralab* algorithm for fitting various optical spectra. I cannot forget to thank "Jankowiak recent group members" Dr. Ximao Feng, Khem Acharya, Mukund Koirala, Adam Kell, Lin Chen, all being very helpful and smiling.

Finally, I am very indebted to my parents for their persistent encouragement, support and love. I am also grateful to my brothers and sisters for loving me, my dear wife 'Amita' for being always on my side, and little son 'Aryav' for being a quiet boy.

Dedication

To my parents

(Mother Mina Neupane and Father Thaneswor Neupane)

Chapter 1 - Introduction

1.1. An overview of natural photosynthesis

Photosynthesis is one of the most complicated and an important process on Earth and it provides food, fuel and oxygen. There are two types of photosynthesis: oxygenic and anoxygenic. In oxygenic photosynthesis the overall photosynthetic process completes with the release of molecular oxygen. Higher plants, cyanobacteria, and algae are the organisms that carry oxygenic photosynthesis.[1-3] It is the oxygenic photosynthesis that sustains most of the life on Earth. In contrast, in anoxygenic photosynthesis, for example in purple bacteria, the photosynthetic process does not release molecular oxygen.[4] In all photosynthetic organisms, the basic process of energy transduction is similar and involves: 1) absorption of photons by light harvesting (LH) antenna complexes, 2) transfer of excitation energy to reaction center (RC) complexes, 3) charge separation across the membrane, and 4) the creation of a proton gradient to drive ATP synthesis.[5,6] This overall process of energy transduction is called the primary process or light reaction of photosynthesis. It is believed that insight obtained from the study of primary process of photosynthesis could find applications in future solar cells.

1.1.1. Oxygenic photosynthetic apparatus

The overall process of photosynthesis in higher plants, algae and cyanobacteria is catalyzed by four multi-subunit protein complexes: photosystem II (PSII), photosystem I (PSI), the cytochrome b_6f complex, and F-ATPase.[7] These protein complexes are embedded in thylakoid membranes inside the chloroplast and they work in concert. The basic arrangement of these four protein complexes is shown in Figure 1-1. Photosystems I and II form super-complexes with Chlorophyll (Chl) *a/b* containing peripheral LH complexes. The nature of the peripheral LH

complexes vary from organism to organism and also on growth conditions.[8] In higher plants, the trimeric LH complex II, CP26, and CP29 are three important peripheral pigment-protein complexes associated with PSII whereas the tetrameric LH complex I (Lhca1-4) protein is associated with PSI.

The minimum PSII assembly required to catalyze light driven water oxidation, also called the PSII core, consists of central D1/D2/cytb559 RC pigment-protein surrounded by CP47 and CP43 core pigment-proteins along with some external non-pigment containing proteins.[9] The PSII core

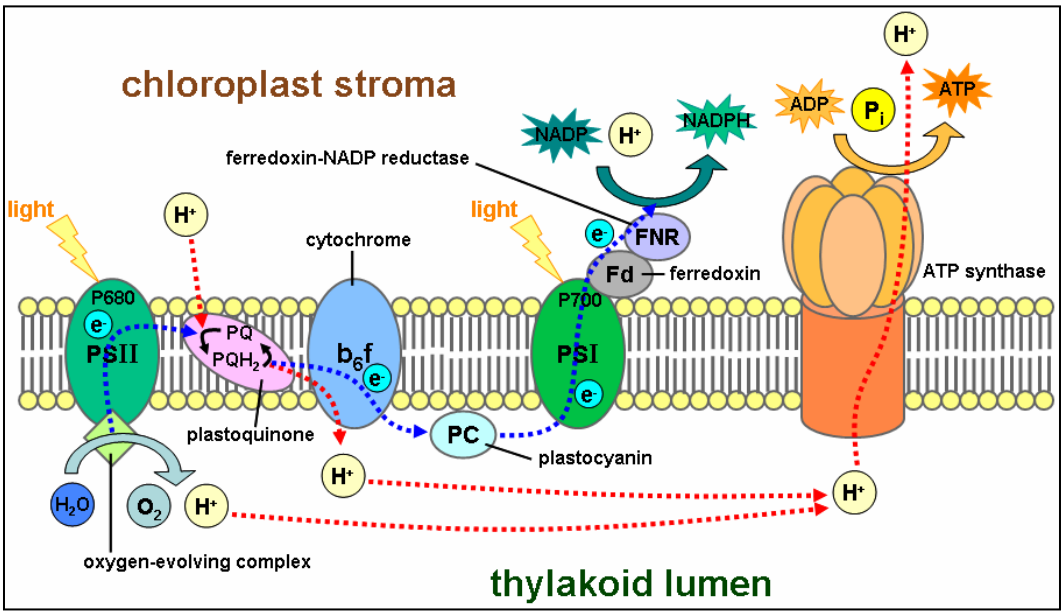

Figure 1-1 Organization of photosynthetic units in thlakoid membrane of plants.[10]

complexes of higher plants, algae and cyanobacteria are dimeric and structurally very similar.[11] The central part of the PSII core consists of D1/D2 hetrodimeric RC protein each having five transmembrane helices. Two Chl *a* containing proteins, CP43 and CP47, flank the D1 and D2 proteins on each side. The arrangement of pigments in each PSII core monomer is shown in Figure 1-2 (frame A). These pigments are roughly arranged in two layers on the stromal and lumenal sides of the membrane with at least one Chl acting as a linker between the layers.[12]

Recent high resolution crystal structures of cyanobacterial PSII core[13,14,15] confirm that RC proteins contain six Chl *a* (special pair Chls: P_{D1} and P_{D2}, two accessory Chls: Chl_{D1} and Chl_{D2}, and two peripheral Chls: $Chlz_{D1}$ and $Chlz_{D2}$), two pheophytin *a* ($Pheo_{D1}$ and $Pheo_{D2}$), two plastoquinones (Q_A and Q_B), two β-carotene molecules and one non-heme iron. These cofactors, as shown in Figure 1-2 (frame B), are involved in energy and electron transfer processes and are arranged in approximate C_2 symmetry. The number of Chl *a* molecules in CP43 and CP47 proteins are 13 and 16, respectively making total of 35 Chl *a* in each PSII core monomer.[13,14,15]

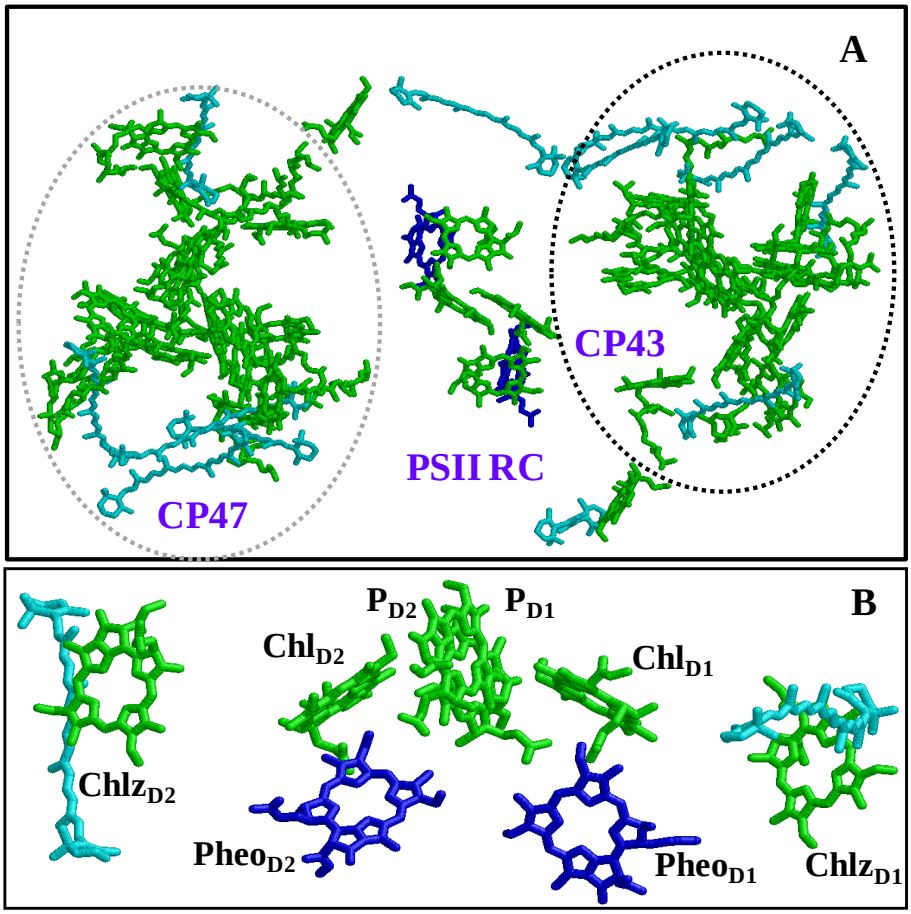

Figure 1-2 Arrangement of pigments in PSII core (A) monomer.[13] Pigments are color coded with Chls green, carotenoids cyan, and Pheos blue. Pigments belonging to CP47 and CP43 proteins are shown inside gray dotted and black dotted ovals, respectively. (B) The pigments belonging to D1/D2 RC proteins. For clarity the alkyl tails of Chls and Pheos pigments belonging to RC proteins are truncated.

The trimeric Photosystem I is another giant pigment-protein complex with each monomer consisting of around 12 protein subunits. The high resolution crystal structure of PSI[16] reveals that each monomer contains 96 Chls, 2 phylloquinones, 3 Fe_4S_4 clusters, and 22 carotenoids. Light captured by the antenna system of PSI is efficiently transferred to the PSI core. The primary charge separation in the PSI core is initiated from the excited chlorophyll dimer P700 and the electron moves along the electron transfer chain consisting of A_0 (Chl a), A_1 (phylloquinone), and three iron sulfur clusters F_X, F_A and F_B as shown in Figure 1-3. Electrons from F_B, in the stromal side, are transferred to ferredoxin (Fd) and further transferred to $NADP^+$ reductase. The oxidized P700 is reduced by electron transfer from cytochrome c6. Electrons are fed to cytochrome c6 from PSII via a pool of plastoquinones (Pc) and the cytochrome b6/f complex.[16] The terminal electron acceptors in PSII RC and PSI RC are quinones and Fe-S clusters, respectively. Due to this reason PSI RC and PSII RC are sometimes referred to as type I and type II RC, respectively.[16]

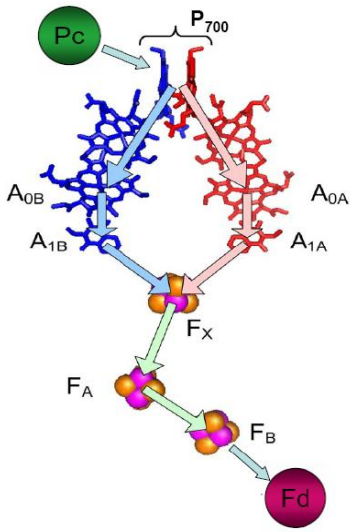

Figure 1-3 Arrangement of cofactors in PSI core. Cofactors belonging to chains A (shown as red) and B (shown as blue) are labeled by subscripts A and B, respectively. For clarity the long alkyl tail of Chl is truncated.

Cyanobacteria are the most abundant species of bacteria and provide most of the global oxygen demand via oxygenic photosynthesis. Like in higher plants, the overall photosynthetic process of cyanobacteria is catalyzed by two photosystems: PSII and PSI. Phycobilisomes are the only external peripheral LH antenna found in cyanobacteria under normal growth conditions. When grown in an iron limited environment, cyanobacteria express one additional protein, IsiA, around PSI so as to make a super-complex[17]. Crystal structure of this supercomplex is not known yet. However, electron microscopy images of this super-complex show that closed ring 18 IsiA proteins surround the trimeric PSI (see Figure 1-4).[18] Each IsiA protein is believed to be very similar to the CP43 protein of PSII core and also referred to as CP43′.[19] Additional details of PSI- CP43′ supercomplex as well as motivation for the study of isolated CP43′ complex are provided in Chapter 2.

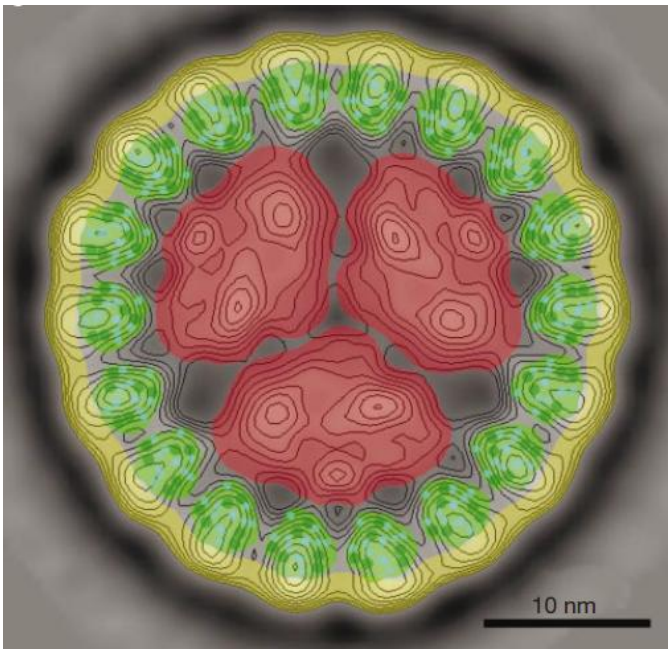

Figure 1-4 Electron microscopy image of PSI-CP43' complex.[18] The central part depicts the trimeric PSI (red) surrounded by a ring of 18 mer CP43' proteins.

1.1.2. Anoxygenic photosynthetic apparatus

Green sulfur bacteria, purple bacteria, green filamentous bacteria, and heliobacteria are the classes of anoxygenic photosynthetic bacteria. Purple bacteria are the most diverse, simple and highly studied group of anoxygenic bacteria. *Rhodobacter sphaeroides* (formerly named as *Rhodopseudomonous sphaeroides*) is one of the most commonly studied species of purple bacteria.[20,21] Like the oxygenic photosystem, the purple bacterial photosystem comprises an antenna system and reaction system. The antenna system of purple bacteria, which contain bacteriochlorophyll (BChl) and carotenoid (Car) as pigments, is complicated and, in general, consists of LHII and LHI. LHI directly surrounds the RC and is also called the B875 complex, where the number 875 refers to the Q_y (0, 0) room-temperature absorption maximum. LHII is far from RC and helps to transfer energy to the RC via LHI.[20,21] A model of the arrangement of LH complexes and RC complex of *Rhodobacter sphaeroides* is shown in Figure 1-5.

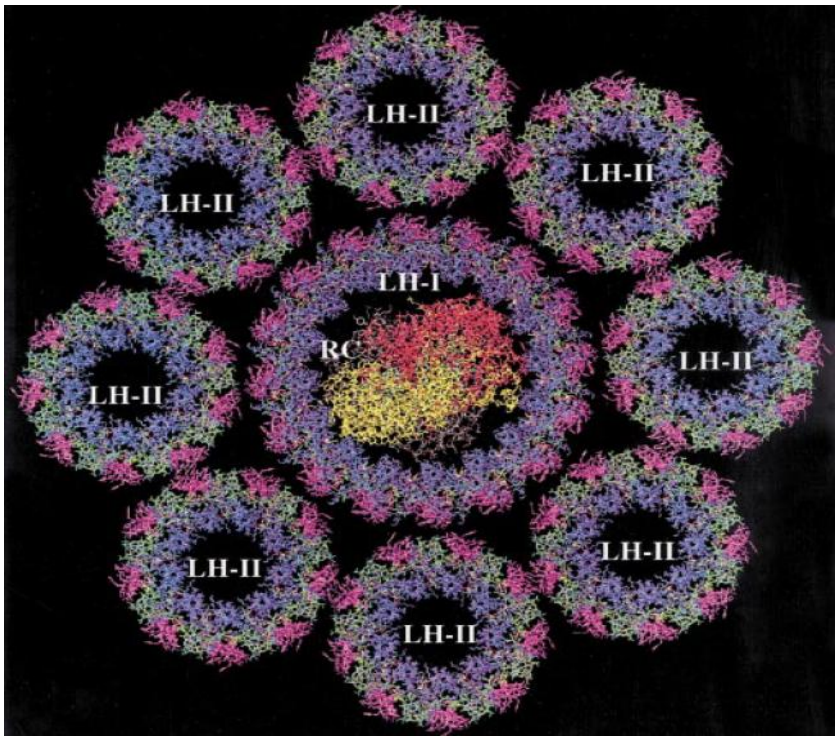

Figure 1-5 Modeled arrangement of photosynthetic units of *Rhodobacter sphaeroides*.[20]

LHII is also referred as the B800-850 complex as it absorbs maximally at 800 and 850 nm. LHII consists of two concentric cylinders of α and β polypeptides. BChls in these polypeptides are organized to form two distinct rings. The inner ring (B850) comprises eighteen BChls but the outer ring (B800) consists of nine BChls.[21] LHI also contains concentric cylinders of α (inner) and β (outer) polypeptides (typically 15 pairs) but here BChls are arranged so as to make single ring (B875). LHI, being much larger than LHII, encircles the RC.

The reaction systems of purple bacteria are well characterized. The reaction center protein of *Rhodobacter (Rb.) sphaeroides*, as revealed by high resolution crystal structure[22-25], consists of three subunits conventionally referred to as H (heavy), M (medium) and L (light). However, these designations were made before the true mass of these subunits was determined and the mass in decending order follows as: H>L>M. These subunits bind ten cofactors that are arranged in approximate C_2 symmetry. These cofactors, as shown in Figure 1-6, are: i) strongly coupled bacteriochlorophylls (BChls) referred to as special pair dimers P_A and P_B, ii) two weakly coupled monomeric BChls B_A and B_B, called accessory Chls, iii) two bacteriopheophytins (BPheo) molecules H_A and H_B, iv) two quinones molecules Q_A and Q_B along with a nonheme iron are present in the cytoplasmic part of the RC, and v) a carotenoid (Car) molecule that is present close to B_B. In Chapter 3, spectroscopic properties of a novel RC from Rb. sphaeroides RC that contains Zinc Bacteriochlorophyll in all P, B and H sites (called Zn-RC) and its beta mutant (Zn-β-RC) are investigated. The detail motivation for the study is provided in Chapter 3, but here only a general introduction of bacterial RC will be provided.

Light absorbed by antennae protein cofactors is funneled to the RC cofactors. In RC, EET (H to B to P) involves equal participation of A and B branch cofactors. Absorption of photons by

special pair leads to electron transfer from P* (excited P) to H_A via B_A. Finally, electron reaches the Q_B via Q_A. ET in wild type RC involves, only A branch cofactors. The oxidized P870 (P^+) is reduced by the water soluble cytochrome (*cyt*) *c2* complex. A second light induced electron transfer process, after uptake of two protons, changes Q_B to QH_2 (ubiquinone). QH_2 is mobile and is used by the *cyt bc1* complex (along with RC) in translocating the proton across the membrane.[26,27]

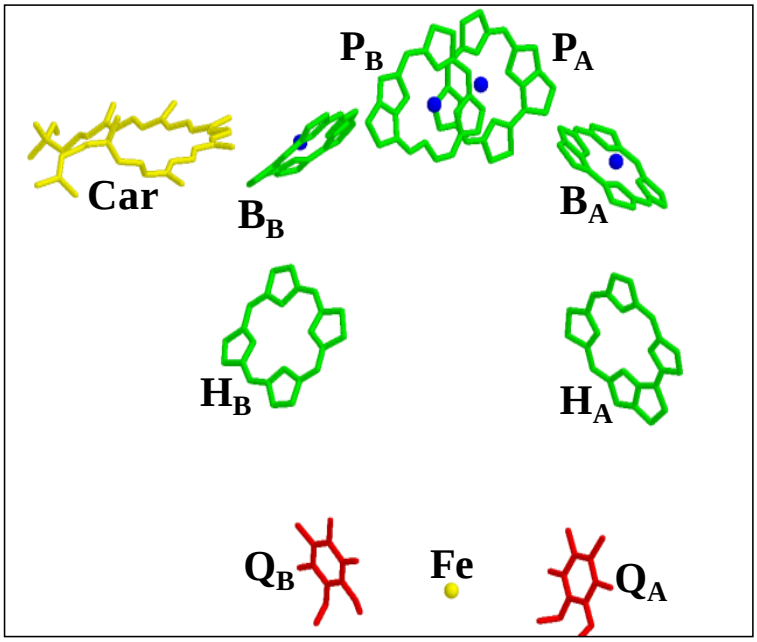

Figure 1-6 Cofactor arrangement in *Rb. Sphaeroides* RC, modified from 2.0 Å crystal structure (PDB ID 3I4D). Cofactors involved in EET and ET are shown in different colors: Car yellow, BChl (Mg atoms shown as blue sphere) and BPheo green, and ubiquinones red. For clarity, alkyl tail of ubiquinones and BChls and all other side chains of BChls are truncated.

1.2. Artificial photosynthesis

The primary process of natural photosynthesis is very efficient with photon to charge separation efficiency close to 100 %.[4-6] The natural photosynthesis process is optimized in all respects: frequency, space, and time. The natural photosynthetic antennas are organized such that they can absorb and transfer the excitation energy optimally. The RC is also optimized in a way that forward electron transfer is much faster than back transfer, thus minimizing charge recombination. Also the ET in the RC takes place through a well defined path so as to minimize recombination. In these respects, natural photosystems are highly optimized solar cells. In recent years, inspired by natural photosynthesis, a number of research groups (to mention a few [28-31]) are involved in designing solar cells based on synthetic molecules. Current efficiency of such solar cells, as compared to natural photosynthesis, is very low.[32] A number of factors need to be optimized to increase their performance. The right choice of donor-acceptor pair, photo-stability, their relative orientation, and proper design of interface are some of the important factors.[33] The ideal donor molecule should have a very high extinction coefficient, broad spectral coverage that matches the solar spectrum, and should be photo-stable.[33]

Chlorophyll trefoil (ChlT1) investigated in this work (see Chapter 4) is an example of a synthetic antenna. This molecule has three identical Zn-Chl subunits linked with rigid linkers, see Figure 1-7. ChlT1 can be used as artificial antenna (donor molecule) and in the presence of a suitable acceptor can be used to make photovoltaic devices. ChlT1, in suitable solvents, forms different aggregates with multiple picosecond EET pathways possible, thus mimicking natural antenna systems.

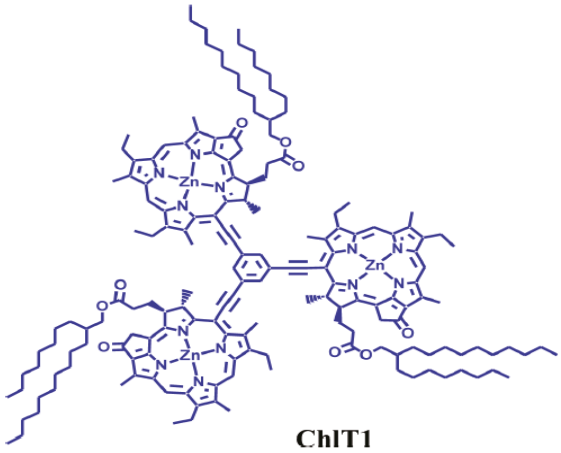

Figure 1-7 Structure of chlorophyll trefoil (ChlT1)

1.3. Excitonic interaction

This thesis work does not include modeling of various low temperature optical spectra taking excitonic effects into account. However, to understand the optical spectra, it is important to know the basic aspects of excitonic interaction and the modeling theory. So, a brief description of excitonic interaction and an approach to modeling the optical spectra is presented here. In photosynthetic proteins, chromophores are held sufficiently close so as to lead coupling (coulomb, exchange etc.) between them. Due to this coupling, the electronic transition is delocalized over multiple chromophores leading to the formation of delocalized/mixed states called excitonic states. The excited state Hamiltonian in such system is defined as[34]:

$$H = \sum_{n}(\varepsilon_n + d_n)|n\rangle\langle n| + \sum_{n,m} V_{nm}|n\rangle\langle m| \qquad (1\text{-}1)$$

where $|n\rangle$ denotes the localized monomer states, ε_n is the average transition energy of monomer energy, d_n is the offset energy due to diagonal site excitation energy disorder, and n refers to the number of pigments. The matrix H is symmetrical about the diagonal and has $n \times n$ dimension

with site energies in diagonal elements and $V_{n,m}$ coupling in the off diagonal. When the matrix is diagonalized, it gives excitonic energies (E_α) and wavefunctions

$$|\alpha\rangle = \sum_n c_n^{(\alpha)} \, |n\rangle \ . \qquad (1\text{-}2)$$

Since overlap is neglected, $\sum_n \left|c_n^{(\alpha)}\right|^2 = 1$. The excitonic transition dipoles can be calculated as:

$$\vec{\mu}_\alpha = \sum_n c_n^{(\alpha)} \, \vec{\mu}_n \qquad (1\text{-}3)$$

where $\vec{\mu}_n$ is the transition dipole of monomer pigment *n*. The absorption spectrum of the α^{th} exciton state, neglecting the phonons and intramolecular vibrations, is given by:

$$\mathrm{d}_\alpha(\omega) = \left\langle \left|\vec{\mu}_\alpha\right|^2 \, \delta(\omega - \omega_{\alpha 0}) \right\rangle_{\mathrm{dis}} \qquad (1\text{-}4)$$

where $\omega_{\alpha 0}$ is the energy of the α^{th} exciton state and $\langle ... \rangle_{dis}$ denotes an average over disorder in site energies.[34] The net absorption spectrum is given as the sum over the absorption for all excitonic states after convolution with the appropriate single-site absorption spectra. The oscillator strength of each pigment for each excitonic band, also called as occupation number, is determined by $|c_{\alpha n}|^2$.[34]The extent of delocalization depends on the coupling element 'V_{nm}'. The coupling can be calculated in various approximations. If the molecules have no net charges and their center to center distance is larger than the molecular dimensions then the dipole-dipole coupling contributes mostly to the V_{nm}. For a dimer (1,2), the simplest case, it is (in dipole-dipole approximation) given by:[35]

$$V_{12} = V_{21} = \frac{\vec{\mu}_1 \cdot \vec{\mu}_2 - 3(\vec{\mu}_1 \cdot \vec{r})(\vec{\mu}_2 \cdot \vec{r})}{R^3} \qquad (1\text{-}5)$$

where $\mu_{i\ (i=1,2)}$ is the dipole moment of monomers, $\vec{r} = \frac{\vec{R}}{|R|}$ is unit vector in the direction of $\vec{R}$, and R distance between their centers. The coupling matrix *V* is symmetric with n×m dimensions and the sign of the V_{nm} coupling element depends on the relative orientation of the transition dipole moment vectors of the monomer involved. The transition energies of upper (U) and lower (L) excitonic components are given by:

$$\lambda_{L/U} = \frac{\varepsilon_1 + \varepsilon_2 \pm \sqrt{(\varepsilon_1 - \varepsilon_2)^2 + 4V_{12}{}^2}}{2} \tag{1-6}$$

where ε_1 and ε_2 are transition frequencies (site energies) of the monomers in the absence of coupling. The number of excitonic components (excitons) equals the number of monomers involved in the coupling. The distribution of the oscillator strength between the lower and upper excitonic states depends on the relative orientation of the transition dipoles of monomers.[35]

1.4. Mechanisms of excitation energy transfer in photosynthetic systems

The mechanism of EET in photosynthetic complexes depends on the extent of coupling (*V*) between donor-acceptor (D-A) molecules and is categorized as either incoherent or coherent.[36,37] If the ratio of *V* to the disorder (Δ, inhomogeneous broadening) is much less than 1, i.e. $V/\Delta \ll 1$, then the EET is considered an incoherent hopping process between independent, localized D-A states. Such type of EET process can be modeled with Förster[38] and Dexter[39] theories. If the coupling between D-A states is very strong in comparison to disorder i.e. $V/\Delta \gg 1$, then the initial excited state is delocalized and EET is thought to be a wave-like coherent process.[40]

Förster theory of EET is applicable in the weak coupling regime. For the weak coupling case, the intra-and inter-molecular relaxation processes take place on much faster time scales than the EET process. The transfer rate constant ($k_{1\rightarrow 2}$) is given by Fermi's Golden Rule rate expression:

$$k_{1\to 2} = \frac{4\pi^2}{h}\left|V_{1,2}\right|^2 \rho(E) \tag{1-7}$$

where $\rho(E)$ is the Franck-Condon (FC) weighted density of states, h is Planck's constant, and $V_{1,2}$ is the coupling matrix between the D-A states. Density of states is given by:

$$\rho(E) = \int_{E=0}^{\infty} dE G_D(E) G_A(E) \tag{1-8}$$

where $G_D(E)$ and $G_A(E)$ are normalized line shape functions for donor and acceptor molecules. Förster showed that $\rho(E)$ and coupling matrix $V_{1,2}$ are related to absorption spectrum of acceptor $\varepsilon_A(\omega)$ and fluorescence spectrum of donor $f_D(\omega)$. The most commonly used form of the Förster equation is:

$$k_{1\to 2} = \frac{9\kappa^2 c^4 \phi_D}{8\pi n^4 \tau_D R^6} \int_{\omega} \varepsilon_A(\omega) f_D(\omega) \frac{d\omega}{\omega^4} \equiv \frac{3}{2}\frac{\kappa^2}{\tau_D}\left(\frac{R_0}{R}\right)^6 , \tag{1-9}$$

where R_0 is Förster radius which is the distance at which EET is 50% efficient, R is D-A distance, n is the refractive index, τ_D and ϕ_D are the life time and quantum yield of the donor molecule in the absence of the acceptor, κ is the orientation factor that gives information on the relative orientation of donor and acceptor.[41] Depending on the orientation, κ ranges from -2 to 2 and for randomly oriented chromophores it is 2/3.

Förster EET, also called through space EET, considers Coulomb or direct interaction and is valid when R is greater than the molecular size (R in the range 1-10 nm). However, for closely spaced chromophores (R<1 nm) electronic wave function overlap (exchange interaction) needs to be considered. In this case, the EET is called Dexter (through bond) mechanism. Exchange interaction falls off approximately exponentially with R i.e., stronger distance dependence as compared to R^{-3} dependence (with R^{-6} distance dependence of EET rate) of Coulomb interaction.

Förster EET permits EET only between the state of same spin multiplicity (i.e., singlet-singlet and triplet-triplet), however, Dexter EET does not have any spin restriction. The photoprotective carotenoid reaction that quenches triplet Chl states can only be explained by Dexter EET.[42]

If the coupling between the D-A is very large, as stated earlier, there is the formation of new excitonic states which are the superposition of locally excited states. In this case, EET takes place between the locally excited states that belong to the same exciton. This means excitation oscillates back and forth between D-A local states just like a wave.[35,43] However, such oscillation persists for short time after the creation of initial excited state.[44] Such coherent transfer exists when the transfer time is much faster than inter- and intra-molecular relaxation processes so that the locally excited states do not go out of phase so quickly.[42,41] Relaxation of a higher exciton state to a lower state takes place by exchanging energy with the bath. This relaxation process results in net transfer of energy. Exciton bath coupling that is characterized by the spectral density of states which defines which frequencies of the bath are available to relax.[41]

Recent two dimensional photon studies[45-47] have shown that electronic coherence (even at room temperature) in photosynthetic proteins persists as long as 400 fs, so coherent EET, which is believed to be much efficient than incoherent EET, should play a significant role in energy transfer process in photosynthesis.

EET in photosynthesis complexes can be measured at room and low temperature by using time domain approaches like photon echoes and transient absorption spectroscopy, and at helium temperature using spectral hole burning (HB). Time domain approaches, which measure time variation of absorption or emission or echo signal, need a laser having lifetime shorter than the time scale of EET. EET time in time domain approach is obtained from the fit of kinetic traces. However, EET time determination by HB do not need fast laser but needs a laser having

linewidth much narrower than homogeneous line width. Approach to determine EET from HB is shown in Chapter 4.

1.5. Nature of biological electron transfer

Fermi Golden rate equation stated in Eq. 1-7 can also be used to explain ET between weakly coupled donor-acceptor states. The modified form of Eq. 1-7 is expressed as[48]:

$$k_{et} = \frac{4\pi^2}{h}|V|^2 FC \qquad (1\text{-}10)$$

where V is the quantum mechanical matrix element that describes the coupling between D-A electronic wavefunctions, FC is the Franck-Condon weighted density of states which is basically the overlap integral between the D-A vibrational wavefunctions of equal energy. The electronic coupling varies exponentially with the D-A distance R as[48]:

$$V^2 = V_0^2 \exp(-\beta R), \qquad (1\text{-}11)$$

where V_0^2 refers to maximum coupling. Marcus showed[49] that FC in the Eq. 1-10 can be expressed as:

$$FC = (4\pi\lambda kT)^{-1/2} \exp-[(-\Delta G^o - \lambda)^2/4\lambda kT] \qquad (1\text{-}12)$$

where λ is reorganization energy which is the energy required to distort the equilibrium geometry of donor state to acceptor state equilibrium geometry without ET, ΔG^o is the standard Gibbs free energy change which is basically the free energy difference between D-A states, T is temperature in K, and k is Boltzmann constant. The ΔG^o related to donor oxidation potential (V^{ox}) and acceptor reduction potential (V^{red}) as:

$$\Delta G^o = F(V^{ox} - V^{red}) + C \qquad (1\text{-}13)$$

where F is Faraday constant and C represents the coulomb attractive energy[50].

In general, λ increases with increase in polarity of the environment of D-A centers.[48] Quantum corrected Marcus-type expression[51] and semi-classical[52] expressions are also proposed for FC. The classical Marcus equation useful to explain the nature of biological electron transfer. From Eq. 1-12 it is apparent that the FC becomes maximum when $-\Delta G^o = \lambda$. Combined result of Eq 1-10 and 1-12 shows that ET rate has Gaussian dependence on $-\Delta G^o$ having width of $\sqrt{2\lambda kT}$. The ET increases with $-\Delta G^o$, with maximum rate obtained at $-\Delta G^o = \lambda$ (called activation less transfer) and the rate decreases for $-\Delta G^o > \lambda$ (called inverted regime). At the inverted regime, some vibration energy/excitation is needed to reach the D-A curve crossing. The Marcus equation is particularly suitable for the regime $\hbar\omega << kT$. This regime can only explain the role of low frequency solvent mode or outer sphere effect to the ET. If high frequency intermolecular modes are to be included (for example, intramolecular ET), i.e. for the case $\hbar\omega >> kT$, the classical Marcus equation is to be quantum corrected to allow for the possible tunneling effect.[51] In this case, the Gaussian curve becomes slightly asymmetrical and carries a width of $\sqrt{\lambda\hbar\omega}$.[48]

A bacterial RC has been studied by a number of groups as a model system to understand the nature of ET in biological systems.[48,53-58] Pump probe experiments in various BRCs has demonstrated that decay of primary electron donor state is biexponential (with ~ 2 ps and 6 ps componets observed at room temperature, and ~1 ps and 10 ps components observed at helium temperature[50,57]), weakly excitation wavelength dependent, and is 2-3 times faster at helium temperature. Three different models are porposed to explain the experimental ET kinetic data: inhomogeneous model, nonequilibrium excited-state model, and reaction diffusion model.

Inhomogeneous model suggests that RC has many static (as compared to time state of ET) conformational substates/conformers that lead to Gaussian distribution of ΔG^o.[54,59,60] If this is the case, there should be strong excitation wavelength dependent ET kinetics. This model

simply suggests that incorporation Gaussian distribution of ΔG^o in the classical Marcus equation is enough to explain the observed kinetics.

Nonequilibrium excited-state model suggests that ET occurs from vibrational hot state. This model introduces time dependent reorganization energy and also assumes that multiple vibrational modes are important for ET.[53] According to this model, the initially prepared nuclear state strongly affects the ET. If this true, there should be strong wavelength dependent ET kinetics.

Above mentioned models cannot explain the weak excitation wavelength and unusual temperature dependent ET kinetics. To explain these experimental observations, reaction diffusion model is porposed recently.[57,58] In this model, ET is limited by a search of protein conformational space having least or zero activation energy i.e., search of nearly $-\Delta G^o=\lambda$ regime. At high temperature because of large thermal energy, right after excitation, protein explores all possible conformational substates before productive conformational space is reached. At low temperature, unproductive conformational diffusions are excluded, so that productive conformational state is reached earlier. This explains the faster ET observed at helium temperature.[57,58] Since ET is controlled by protein dynamics, there should be, as observed experimentally, a weak excitation wavelength dependent ET kinetics. This model incorporates fast and slow (as compared ET kinetics) protein motions and protein dielectric relaxation function, Cp(t), in the classical Marcus equation. This function can be indirectly measured by monitoring tryptophan absorption changes during the ET.[57,58]

ET time can be measured either by time domain approaches or by frequency domain approaches like photochemical hole burning (PHB). Time domain approach requires fast laser having lifetime shorter than the time scale of ET. But in PHB one needs laser having line width,

in frequency scale, much narrower than the homogeneous line width. The approach to determine ET time by using PHB is shown in Chapter 3.

1.6. Homogeneous line shape, zero phonon line, and electron phonon coupling

Based on the Heisenberg uncertainty principle, the homogeneous line width (Γ_{hom}) of an optical transition of chromophores/impurities residing in solid matrices (crystals, glasses, protein), even at T= 0 K, possesses characteristic relaxation time T_1 which is expressed as:[61]

$$\Gamma_{hom} = \frac{1}{2\pi c T_1} \tag{1–14}$$

where Γ_{hom} is the homogeneous line width (full width at half width of Lorenzian line shape) in cm^{-1}, c is the speed of light in cm/s. The typical Γ_{hom} width (full width at half maximum, fwhm) at 0 K ranges 10^{-4}-10^{-3} cm^{-1} and corresponds to a T_1 of ~10^{-7}-10^{-8} s.[61]At higher temperatures (T>0 K) thermally activated phonon modes of the matrix change the phase of the initially excited electronic state (dephasing) so that the time dependent part of the electronic wave function, $\exp(iE_{ex}t2\pi/h)$, carries an additional random phase factor, resulting in a shortening of the excited state lifetime. Thus, at higher temperatures, Γ_{hom} carries additional uncertainty broadening and is expressed as[61]:

$$\Gamma_{hom} = \frac{1}{\pi c T_2} = \frac{1}{2\pi c T_1} + \frac{1}{\pi c T_2^*} \tag{1-15}$$

where T_2 is total dephasing time and T_2^* is pure dephasing time.

The homogeneous line shape of the transition in which no matrix phonons are created or destroyed is called the zero-phonon line (ZPL). The ZPL originates either from pure electronic or vibronic transitions. For transitions that are accompanied with net creation or destruction of

phonons, a broad continuous band is observed on the high/low energy side of the ZPL in the absorption/fluorescence spectrum. This is called the phonon side band (PSB). The intensity of the PSB is determined by the geometry change of chromophore molecule in ground and excited states and can be explained by the Franck-Condon principle.[61] For weak electron-phonon coupling, the equilibrium geometry change in ground and excited states, Δq_i, is very small, and the opposite is true for strong coupling as shown in Figure 1-8. Note that Figure 1-8 assumes linear electron-phonon (el-ph) coupling (i.e. $\omega_i^g = \omega_i^e$). The single site spectrum, as shown in Figure 1-8, consists of ZPL and PSB and the very simple form is expressed as:

$$L(\omega,T) = \phi_{ZPL}(\omega,T) + \phi_{PSB}(\omega,T) \tag{1-16}$$

where the first term corresponds to the ZPL and the second corresponds the PSB. The detailed form of single site spectrum is provided in Chapter 3. At low temperature (T=0 K), the ZPL possesses a Lorenzian width that originates from uncertainty broadening. However, interaction with matrix two level systems and el-ph coupling causes the ZPL width to increase with temperature.[62-64] Linear el-ph coupling explains the formation of PSB only, so to explain this behavior one has to assume quadratic el-ph coupling. The temperature dependence of homogeneous linewidth is expressed as: $\sim T^{1+\mu}$ with $\mu \sim 0.3$ below 5 K.[41,61,65,66]

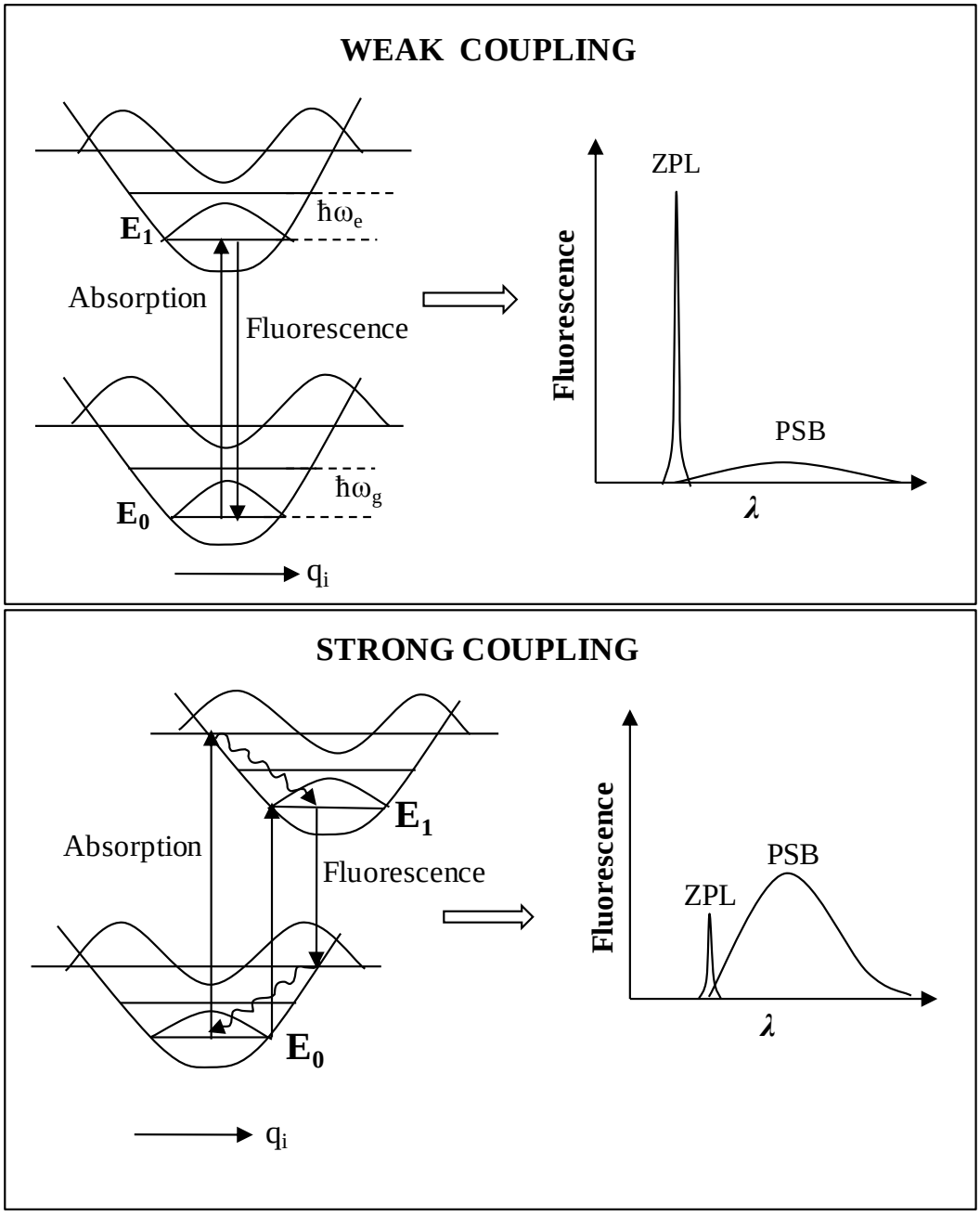

Figure 1-8 Schematic of potential energy curves for weak (upper panel) and strong (lower panel) linear (i.e., $\omega_g=\omega_e$) el-ph couplings. Electronic transitions between ground (E_0) and excited (E_1) states are indicated by vertical arrows in accordance with Franck Condon approximation.

The Debye-Waller factor (DWF), α (also called the Franck-Condon factor), characterizes the spectral intensity of ZPL the and PSB:[67]

$$\alpha = \frac{I_{ZPL}}{I_{ZPL} + I_{PSB}} \tag{1-17}$$

where I_{ZPL} and I_{PSB} are integrated intensities of the ZPL and PSB respectively. For N phonon modes at T~0 K, the DWF is given by: [67-70]

$$\alpha = \exp(-S) \tag{1-18}$$

where S is the Huang-Rhys factor and is defined as:

$$S(T=0) = \frac{M_i \omega_i}{2\hbar} \sum_i (\Delta q_i)^2 \tag{1-19}$$

where ω_i and M_i are the frequency and reduced mass of phonon mode i, respectively, and Δq_i is the change of the equilibrium position corresponding to the lattice normal coordinate q_i. Weak el-ph coupling refers to small Δq_i and correspondingly a small value of S (i.e., S <1). The weak el-ph coupling is manifested in absorption/fluorescence single site spectrum as a very intense ZPL and very weak PSB. The opposite is true for strong coupling (S>1). These two cases are shown in the right side of Figure 1-8. Antenna complexes (CP43, CP47, CP29 etc.) are characterized by a small S ($S \leq 1$) whereas RC complexes are characterized by a large S (for example in bacterial RC S ranges from 3-4). If S is very large ($S \geq 10$), no sharp ZPL is observed in the single site spectrum and the transition is said to be Franck-Condon forbidden.[41]

1.7. Inhomogeneous broadening

The absorption spectra of pigments embedded in a protein matrix are inhomogeneously broadened. The inhomogeniety originates from the presence of slightly different local environments in the protein. Due to small differences in the environment of chromophores at a local level, each chromophore absorbs at a slightly different frequency. Inhomogeneous broadening is characterized by the inhomogeneous/site distribution function (IDF/SDF), G(ω), which is believed to be a Gaussian line shape having inhomogeneous width of Γ_{inh} (fwhm).[61,71,72] The Γ_{inh} is always greater than the Γ_{hom}, and for proteins and glasses, Γ_{inh} values lie, typically, in the range ~100–400 cm^{-1}.[61] The experimental absorption spectrum of a bulk sample in a protein glass is the convolution of the single site absorption spectrum with G(ω). This gives the ensemble spectrum a characteristic width (in cm^{-1}), for small *S*, of $\Gamma_{inh+S\omega_m}$, where *S* (as defined above) is the Huang-Rhys factor and ω_m is the mean phonon frequency in cm^{-1}.[41,61,68]

1.8. Spectral hole burning

To get the dynamical information of molecules buried in the broad absorption profile, we need site-selective techniques, for example, spectral hole burning (HB), fluorescence line narrowing, and single photosynthetic complex spectroscopy. These approaches complement other time domain approaches (like pump-probe and photon echoes) and, in recent years, they have proven to be powerful approaches to investigate the excitonic structure, dynamics, and pigment-pigment and pigment-protein interactions of several pigment-protein complexes.[41,73] These approaches, as compared to conventional spectroscopy at room temperature, increase the spectral resolution by a factor of 10^3-10^5.[41,61,67,68]

Spectral HB, which is the focus of this thesis work, is a low temperature site-selective frequency domain approach. The basic understanding of HB stems from the study of dispersed chromophores embedded in a regular glassy matrix.[61,74-76] However, two fundamental differences exist between HB in photosynthetic complexes (PC) and in regular glass. First, in PC chromophores are excitonically coupled but an ordinary glassy matrix deals with non-interacting chromophores. Thus, in a protein one has to deal with inter- as well as intra- PC structural heterogeneity that leads to diagonal (in site energies) as well as off diagonal (in coupling) disorder.[68] Secondly, dynamics of chromophores in PC are usually explained considering the complex energy-landscapes instead of simple two-level system (TLS) considered for regular glass.[77]

As stated earlier, absorption spectra of pigments in PC proteins, due to inhomogeneous broadening (both intra-and inter-complex) and excitonic coupling, are complicated. However, SHB in such systems still can provide important informations.[41,61,68]

I. Excited state lifetimes of S_1Q_y (0, 0)-states due to nonradiative (EET and ET) and radiative (fluorescence) processes can be obtained by measuring the width of ZPH. The detail is provided in Chapters 3 and 4.

II. Zero-phonon action (ZPA) spectrum, in which ZPHs are burned at different wavelengths under constant fluence (f=I×t, were I is laser intensity and t is time) or intensity, can provide static Γ_{inh} values of the low energy state(s).

III. Vibronic hole burning can provide the Franck-Condon factors and frequencies of various intramolecular vibrational modes of pigments that contribute to the lowest excitonic states. Comparison of these vibrational modes with those of isolated pigments in low temperature glass can give information on the pigment-protein interactions, for example

H-bonding and coordination status of central metal atom. The El-ph coupling parameters (Huang-Rhys factors, phonon frequencies, and also the reorganization energy), which are important parameters for calculation of ET and EET rates, can be also obtained. Usually the presence of large value of the S is an indication of charge transfer (CT) state. The presence of CT state can be further confirmed by high pressure and Stark's HB studies.

IV. In photosynthetic complex, usually, there is lack of correlation between the absorption bands of different states. Burning into higher energy state results, due to fast EET, in a formation broad satellite hole related to lowest excitonic states. Such observation gives qualitative picture on the extent of excitonic interaction and EET.

V. Pure optical dephasing, which originates due to coupling of Q_y-optical transitions with protein TLS, can be studied.

1.8.1. Types and mechanism of hole burning

The basic principle of HB is quite simple. In spectral HB, a narrow line width laser of frequency ω_B is used to selectively excite a subset of chromophores from an inhomogeneously broadened absorption profile. These molecules are excited via their ZPL and are photophysically or photochemically transformed so that they do not absorb at the original frequency. When these molecules return to the ground state, a hole will be formed in the absorption spectrum revealing sharp zero phonon hole (ZPH). As stated earlier, the ZPL is accompanied by the PSB, the ZPH will be accompanied with a broad phonon side band hole (PSBH) on the higher energy side of the ZPH. The burn laser also (non-resonantly) excites ZPLs of other molecules, via their PSBs, that lie lower than ω_B. This process results in the formation of a 'pseudo' PSBH to the lower

energy side of the ZPH.[78] If the laser liner width is very small compared to Γ_{hom}, only individual homogeneous lines burn from the broad absorption profile.[68]

There are two types of HB processes: transient (triplet bottleneck) HB and persistent HB. In triplet HB some long-lived metastable state is populated via intersystem crossing from the excited singlet state. This leads to a loss of ground state population for the time equivalent to the triplet life time, creating a hole in the absorption spectrum.[79,80] The triplet state absorbs well below the singlet ground state and in photosynthetic complexes is believed to be an energy dissipative nonradiative state.

In persistent HB, the hole exists for significantly longer time (for days or even years) even after the burning laser is off, as long as the temperature is kept sufficiently low ($T \leq 10$ K). Two types of persistent HB are recognized: photochemical and nonphotochemical. In photochemical HB, which is not the subject of interest of this thesis, the chromophore undergoes some kind of photoreaction (such as isomerizaion, bond breaking, tautomerization) while it is in the excited state.[81-83] In nonphotochemical HB the chromophore, which is photochemically stable, is photophysically trapped in a new configuration leaving a hole in absorption spectrum.

Based on the optical dephasing process in regular glass it is proposed that extrinsic and intrinsic TLS are needed for a hole formation.[84] Extrinsic TLSs (TLS_{ext}) are related to the chromophore and inner shell of solvent molecules, whereas intrinsic TLSs (TLS_{int}) are related to the host matrix. However, consideration of only TLSs is oversimplistic and extensions beyond this (i.e., multi level) is to be considered.[41] However, in a protein matrix these two TLSs are difficult to distinguish.[41] The optical excitation of chromophores triggers rearrangement of the host environment in the outer shell. This process is accompanied by phonon assisted tunneling, which is the rate limiting step in the HB process, in TLS_{ext}. After phonon assisted tunneling process in

excited state, the chromophore is trapped into a new ground state configuration; see Figure 1-9. At low temperatures the barrier in ground state is higher than the thermal energy, so the chromophore will be trapped in this configuration for sufficiently long time as long as the temperature is low. The schematic shown in Figure 1-9 leads to a blue- shifted anti-hole (photo-product). A configuration other then that shown in Figure 1-9 is considered to account for a red-shifted photoproduct.

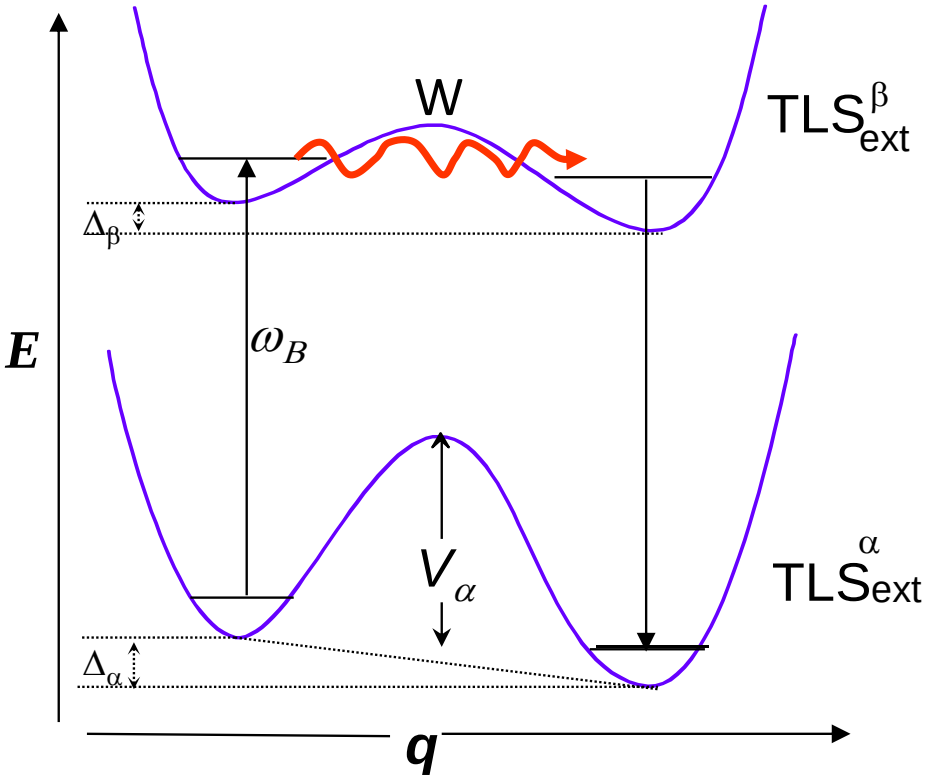

Figure 1-9 Schematic representation of persistent NPHB mechanism. Extrinsic TLS belonging to ground state is labeled as α and β, respectively. Asymmetry parameters in ground and excited states are Δ_α and Δ_β, respectively, and ω_B represents burn frequency.

1.9. Experimental considerations

A Bruker HR125 Fourier transform spectrometer was used to measure the absorption and HB spectra. In absorption and non-resonant HB, the resolution was set at 4 cm^{-1} (low resolution). For resonant HB, a spectral resolution of 0.5 cm^{-1} (high resolution) was used. The intensity of the probe light was kept low (<50 $\mu W/cm^2$) so as to minimize any additional burning while measuring the absorption spectra. Absorption spectra reported are the average of 400 and 100 scans for low and high resolution, respectively. Time required for a low resolution absorption measurement (400 scans with 20 kHz scanner velocity) is ~5 min whereas for a high resolution measurement (100 scan with 20 kHz scanner velocity) is ~15 min. Fluorescence spectra were collected by a Princeton Instruments Acton SP-2300 monochromator equipped with a back-illuminated CCD camera (PI Acton Spec-10, 1340 × 400). To minimize the scattered light, fluorescence was collected perpendicular to the excitation beam. The fluorescence photons traveled to the spectrograph by a multimode optical fiber. The radiative energy transfer contribution, that can lead to a red shift of the fluorescence origin (0, 0), band is minimized by using a thin (1 mm vile) and dilute sample (OD≤0.1). All emission spectra were obtained with a resolution of 0.1 nm. The laser source for both non-resonant HB and fluorescence was 496.5 nm produced from a Coherent Innova 200 Ar^+ laser. A Coherent CR699 ring dye laser (tunable range 650-720 nm with LD688 laser dye) provided frequencies required for the resonant HB and fluorescence excitation measurement for Chl based samples (in this work CP43' and trefoil), whereas a tunable (890-905 nm with MW optics) Coherent CR899 Ti-Sapphire ring laser provided frequencies needed for resonant HB study in BChl based samples (in this work zinc-RC and Zn-β-RC samples). Both ring lasers were pumped by a Spectra-Physics Millenia 10 watt 532 nm diode-pumped solid state laser. The laser line width for both ring lasers was ~0.07 cm^{-1}. However, with intracavity etalon the laser linewidth, when needed, can be narrowed down to ~10

MHz (~3×10^{-4} cm^{-1}). The ring laser power output was stabilized with an external Laser Power Controller (Brockton Electro-Optics Corp.). The laser power in the experiments was precisely set by a continuously adjustable neutral density filter. All the experiments were performed at 5 K inside a Janis 8-DT Super Vari-Temp liquid helium cryostat. The sample temperature was read and controlled with a Lakeshore Cryotronic model 330 temperature controller.

To verify that our nonphotochemical HB process did not lead to any photochemistry the 5 K pre-burn and post-burn absorption spectra, with the post-burn spectrum measured after thermal cycling i.e. 5 K to 150 K and back to 5 K, were routinely compared. All nonphotochemical holes disappear after thermal cycling. This suggests that, under the HB conditions mentioned in this thesis work, no photochemistry occurred in any samples.

1.10. Dissertation outline

As described in earlier sections, Chapter 1 contains all the fundamentals that are needed to understand the work in this thesis. Experimental considerations for data collection are also provided in chapter 1.

Chapter 2 provides details on low-temperature frequency domain study of CP43' complex isolated from Cyanobacterium *synechocystis* PCC 6803 grown under iron stressed conditions. Data are interpreted considering an uncorrelated EET model (as used for the CP43 protein; appendix A provides the abstract and conclusions of this work) between two quasi-degenerate low-energy states A' and B', and additional inter-monomer EET pathways. This study suggests that for CP43' to be an efficient light harvester, Chls contributing to these low-energy states should face towards PSI. This assignment is in favor of the model suggested by Nield et al. (Biochemistry **2003**, *42*, 3180). For comparison an alternate model proposed by Zhang et al.

(Biochim, Biochim. Acta. **2011**, *473*, 55), inconsistent with our data and the Nield model, is provided in Appendix B.

Chapter 3 provides the HB study of a novel zinc reaction center (Zn-RC) of *Rhodobacter sphaeroides* (with six Zn-BChls) and its β-mutant, in which the Zn-BChl in the bacteriopheophytin (BPheo)-binding site on the A side (H_A) has the Zn *penta*-coordinated. It is shown that the excited state life-time of lowest dimer state P870 is essentially the same in both samples. However, the quantum yield of charge separation decreases by 60 % in the mutant. Theoretical fits to the absorption, resonant, and nonresonant HB spectra are also provided.

In Chapter 4, EET in ethynyl-linked chlorophyll trefoil (ChlT1) and its aggregates is investigated. It is shown that under suitable conditions this molecule forms different types of aggregates. It is shown that EET time in two types of ChlT1-based aggregates is slower by a factor of about 5–7 with respect to that observed for the ChlT1 monomer.

Overall conclusions and future directions of the dissertation are provided in Chapter 5.

Abbreviations

Light harvesting (LH); Reaction center (RC); Chlorophyll (Chl); Pheophytin (Pheo); Bacteriochlorophyll (BChl); Bacteriopheophytin (BPheo), Carotenoid (Car); Chlorophyll trefoil (ChlT1); Excitation energy transfer (EET); Electron transfer (ET); Electron-phonon (el-ph); Homogeneous line width (Γ_{hom}); Zero phonon line (ZPL); Phonon side band (PSB); Hole burning (HB); Two-level system (TLS); Zero phonon hole (ZPH)

References

(1) Barnes, C. R. *Bot. Gaz*. **1893**, *18*, 403.

(2) van Niel, C. B. *Arch. Mikrobiol* **1931**, *3*, 1.

(3) Clayton, R.; Sistrom, W. (eds.) *The Photosynthetic Bacteria*, 1978, New York: Planum Press.

(4) Blankenship, R. E.; Madigan, M. T.; Bauer, C. E. *Anoxygenic Photosynthetic Bacteria*, 1995, Dordrecht: Kluwer Academic Publishers.

(5) Sauer, K. In *Bioenergetics of Photosynthesis* (ed. Govindjee), New York: Academic Press, 1975, pp. 115-181.

(6) Knox, R. S. In *Primary Process of Photosynthesis* (ed. J. Barber), Amsterdam: Elsevier, 1977, pp. 55-97.

(7) Nelson, N.; Yocum, C. F. *Annu. Rev. Plant Biol*. **2006**, *57*, 521.

(8) Barber, J. *Quart. Rev. Biophys*. **2003**, *36*, 71.

(9) Krausz, E.; Hughes. J. L.; Smith, P.; Pace, R.; Årsköld, S. P. *Photochem. Photobiol. Sci.* **2005**, *4*, 744.

(10) Taiz, L.; Zeiger, E. *Plant Physiology*, 5th ed.; Sinauer Associates, Inc., Sunderland, Massachusetts, 2010.

(11) Hankamer,B.; Morris, E. P.; Nield, J.; Gerle, C.; Barber, J. *J. Struct. Biol*. **2001**, *135*, 262.

(12) Nield, J.; Barber, J. *Biochim. Biophys. Acta* **2006**, *1757*, 353.

(13) Guskov, A.; Kern, J.; Gabdulkhakov, A.; Broser, M.; Zouni, A.; Saenger,W. *Nat. Struct. Mol.Biol.* **2009**, *16*, 334.

(14) Loll, B.; Kern, J.; Saenger, W.; Zouni, A.; Biesiadka, J. *Nature* **2005**, 438, 1040.

(15) Umena, Y.; Kawakami, K.; Shen, J. –R.; Kamiya, N. *Nature* **2011**, 473, 55.

(16) Jordan, P.; Fromme,P.; Witt, H. T.; Klukas, O.; Saenger, W.; Krauβ, N. *Nature* **2001**, *411*, 909.

(17) Straus, N. A. In *Advances in Photosynthesis*, Bryant, D. (ed.), Kluwer: Dordrecht, 1994, Vol. 1, pp.731-750

(18) Boekema, E. J.; Hifney, A.; Yakushevska, A. E.; Piotrowski, M.; Keegstra, W.; Berry, S.; Michel, K. P.; Pistorius, E. K.; Kruip, J. *Nature* **2001**, *412*, 743.

(19) Nield, J.; Morris, E. P.; Bibby, T. S.; Barber, *J. Biochem*. **2003**, *42*, 3180

(20) Hu, X.; Ritz, T.; Damjanovic, A.; Autenrieth, F.; Schulten, K. *Q. Rev. Biophys.* **2002**, *35*, 1.

(21) Hu, X.; Schulten, K. *Phys. Today* **1997**, *50*, 28.

(22) Deisenhofer, J.; Epp, O.; Sinning, I.; Michel, H. *J. Mol. Biol.* **1995**, *246*, 429.

(23) Deisenhofer, J.; Epp, O.; Miki, K.; Huber, R.; Michel, H. *Nature* **1986**, *318*, 618.

(24) Deisenhofer, J.; Michel, H. *New Compr. Biochem.* **1992**, *23*, 103.

(25) Ermler, U.; Fritzsch, G.; Buchanan, S. K.; Michel, H. *Structure (London)* **1994**, *2*, 925.

(26) Lin, S.; Jaschke, P. R.; Wang, H.; Paddock, M.; Tufts, A.; Allen, J. P.; Rosell, F. I.; Mauk, A. G.; Woodbury, N. W.; Beatty, J. T. *Proc. Natl. Acad. Sci. U. S. A.* **2009**, *106*, 8537.

(27) Kalman, L.; Williams, J. C.; Allen, J. P. *Photosynth. Res.* **2008**, *98*, 643.

(28) D'Souza, F.; Smith, P. M.; Zandler, M. E.; McCarty, A. L.; Itou, M.; Araki, Y.; Ito, O. *J. Am. Chem. Soc.* **2004**, *126*, 7898.

(29) Kamat, P. V. *J. Phys. Chem. C* **2007**, *111*, 2834.

(30) Luo, C.; Guldi, D. M.; Imahori, H.; Tamaki, K.; Sakata, Y. *J. Am. Chem. Soc*. **2000**, *122*, 6553.

(31) Samuel, A. P. S.; Co, D. T.; Stern, C. L.; Wasielewski, M. R. *J. Am. Chem. Soc*. **2010**, *132*, 8813.

(32) Gledhill, S. E.; Scott, B.; Gregg, B. A. *J. Mater. Res*. **2005**, *20*, 3167.

(33) Forrest, S. R. *MRS Bulletin* **2005**, *30*, 28.

(34) Reppert, M.; Acharya, K.; Neupane, B.; Jankowiak, R. *J. Phys. Chem. B* **2010**, *114*, 11884.

(35) van Amerongen, H.; Valkunas, L.; van Grondelle, R. *Photosynthetic Excitons*; World Scientific: Singapore, 2000; p 168.

(36) Rahman, T. S.; Knox, R. S.; Kenkre, V. M. *Chem. Phys*. **1979**, *44*, 197.

(37) Kühn, O.; Renger, T.; Voigt, J.; Pullerits, t.; Sundström, V. *Trends in Photochem. Photobiol*. **1997**, *4*, 213.

(38) Förster, T. *Ann. Phys. (Leipzig)* **1984**, *2*, 55.

(39) Dexter, D. *J. Chem. Phys.* **1953**, *21*, 836.

(40) Sunstrom, V.; Pullertis, T.; van Grondelle, R. *J. Phys. Chem. B* **1999**, *103*, 232.

(41) Jankowiak, R.; Reppert, M.; Zazubovich, V.; Pieper, J.; Reinot, T. *Chem. Rev*. **2011,** *111*, 4546.

(42) Renger, G. In *Bioenergetics*; Gräbner, P. Malazzio, G., Eds.; Birkhäuser Verlag: Basel, 1997; p 311.

(43) Shreve, A. P.; Trautman, J. K.; Frank, H. A.; Owens, T. G.; Albrecht, A. C. *Biochim. Biophys. Acta.* **1991**, *1058*, 280.

(44) van Grondelle, R. *Biochim. Biophys. Acta.* **1985**, *811*,147.

(45) Brixner, T.; Stenger, J.; Vaswani, H. M.; Cho, M.; Blankenship, R. E.; Fleming, G. R. *Nature* **2005**, *434*, 625.

(46) Engel, G. S.; Calhoun, T. R.; Read, E. L.; Ahn, T.; Mancal, T.; Cheng, Y.; Blankenship, R. E.; Fleming, G. R. *Nature* **2007**, *446*, 782.

(47) Read, E. L.; Lee, H.; Fleming, G. R. *Photosynth. Res.* **2009**, *101*, 233.

(48) Moser, C. C.; Keske, J. M.; Warncke, K.; Farid, R. S.; Dutton, P. L. *Nature* **1992**, *355*, 796.

(49) Marcus, R. A. *J. Chem. Phys*. **1956**, *24*, 966.

(50) Fleming, G. R.; Martin, J. L.; Breton, J. *Nature* **1988**, *333*, 190.

(51) Jorter, J. *J. Chem. Phys*. **1976**, *64*, 4860.

(52) Hopfield J. J. *Proc. Natl. Acad. Sci. U. S. A.* **1974**, *71*, 3640.

(53) Parson, W. W.; Warshel, A. J. Phys. Chem. B **2004**, *108*, 10474.

(54) Jia, Y.; DiMagno, T. J.; Chan, C.-K.; Wang, Z.; Du, M.; Hanson, D. K.; Schiffer, M.; Norris, J. R.; Flemming, G. R.; Popov, M. S. *J. Phys. Chem*. **1993**, *97*, 13180.

(55) Lockhart, D. J.; Boxer, S. G. *Proc. Natl. Acad. Sci. U. S. A.* **1988**, *85*, 7499.

(56) Müh, F.; Lendzian, F.; Roy, M.; Williams, J. C.; Allen, J. P. Lubitz, W. *J. Phys. Chem. B* **2002**, *106*, 3226.

(57) Wang, H.; Lin, S.; Woodbury, N. W. *J. Phys. Chem. B* **2008**, *112*, 14296.

(58) Wang, H.; Lin, S.; Allen, J. P.; Williams, J. C.; Blankert, S.; Laser, C.; Woodbury, N. W. *Science* **2007**, *316*, 747.

(59) Small, G. J.; Hayes, J. M.; Silbey, R. J. *J. Phys. Chem*. **1992**, *96*, 7499.

(60) Kirmaier, C.; Holten, D. *Proc. Natl. Acad. Sci. U. S. A.* **1990**, *87*, 3552.

(61) Moerner, W. E. *Topics in current physics, Persistent spectral hole burning: Science and applications*; Springer-Verlag: New York, 1987; p 1.

(62) Hayes, J. M.; Lyle, P. A.; Small, G. J. *J. Phys. Chem.* **1994**, *98*, 7337.

(63) Flecher, G.; Friedrich, J.; *Chem. Phys. Lett.* **1977**, *50*, 32.

(64) Kikas, J. *Chem. Phys. Lett*. **1978**, *57*, 511.

(65) Koedijk, J. M. A.; Wannemacher, R.; Silbey, R. J.; Völker, S. *J. Phys. Chem.* **1996**, *100*, 19945.

(66) Jankowiak, R.; Small, G. J. In *Disorder Effects on Relaxation Processes*; Blumen, A., Richard, R., Eds.; Springer-Verlag: Berlin, 1994; p 425.

(67) Rebane, K. K. *Impurity Spectra of Solids*; Plenum: New York, 1970; p 1.

(68) Jankowiak, R.; Hayes, J. M.; Small, G. J. *Chem. Rev.* **1993**, *93*, 1471.

(69) Personov, R. I. In *Spectroscopy and Excitation Dynamics of Condensed Molecular Systems*; Agranovich, V. M., Hochstrasser, R. M., Eds.; Elsevier Science Ltd: Amsterdam, 1983; p 1.

(70) Osadko, I. S. In *Advances in Polymer Science*; Dusek, K., Ed.; Springer-Verlag: Berlin 1994, p 123.

(71) Reddy, N. R. S.; Lyle, P. A.; Small, G. J. *Photosynth. Res*. **1992**, *31*, 169.

(72) Jankowiak, R.; Richert, R.; Bässler, H. *J. Phys. Chem*. **1985**, *89*, 4569.

(73) Purchase, R.; Völker, S. *Photosynth. Res.* **2009**, *101*, 245.

(74) De Vries, H.; Wiersma, D. A. *J. Chem. Phys.* **1980**, *72*, 1851.

(75) Kharlamov, B. M.; Personov, R. I.; Bykovskaya, L. A. *Opt. Commun.* **1974**, *12*, 191.

(76) Gorokhovskii, A. A.; Kaarli, R. K.; Rebane, L. A. *JETP Lett*.**1974**, *20*, 216.

(77) Berlin, Y.; Burin, A.; Friedrich, J.; Köhler, J. *Phys. L. Rev.* **2007**, *4*, 64.

(78) Dang, N. C. *PhD Thesis*, Iowa State University, **2005**.

(79) Szabo, A., *Phys. Rev. Lett.* **1970**, *25*, 924.

(80) Erickson, L. E. *Phys. Rev. B.* **1975**, *11*, 4512.

(81) Narasimhan, L. R., Littau, K. A., Pack, D. W., Bai, Y. S., Elschner, A. and Fayer, M. D., *Chem. Rev.* **1990**, *90*, 439.

(82) Dick, B. *Chem. Phys.* **1989**, *136*, 429.

(83) Lee, I.-J., Small, G. J. and Hayes, J. M., *Phys. Chem.* **1990**, *94*, 3376.

(84) Hayes, J. M., Stout, R. P., Small, G. J. *J. Phys. Chem.* **1981**, *74*, 4266.

Chapter 2 - Spectroscopic Study of CP43′ Complex and PSI-CP43′ Supercomplex of the Cyanobacterium *Synechocystis* PCC 6803

(A paper accepted for publication to Journal of Physical Chemistry B, 2011)

Ximao Feng, Bhanu Neupane, Khem Acharya, Valter Zazubovich, Rafael Picorel

Michael Seibert, and Ryszard Jankowiak

Abstract

The PSI-CP43′ supercomplex of the cyanobacterium *Synechocystis* PCC 6803, grown under iron-starvation conditions, consists of a trimeric core Photosystem I (PSI) complex and an outer ring of 18 CP43′ light-harvesting complexes. We have investigated the electronic structure and excitation energy transfer (EET) pathways within the CP43′ (also known as the *IsiA* gene product) ring using low-temperature absorption, fluorescence, fluorescence excitation, and hole-burning (HB) spectroscopies. Analysis of the absorption spectra of PSI, CP43′, and PSI-CP43′ complexes suggests that there are 13 chlorophylls (Chls) per CP43′ monomer, *i.e.*, a number that was observed in the CP43 complex of Photosystem II (PSII) (Umena, Y. *et al. Nature* **2011**, 473, 55-60). This is in contrast with the recent modeling studies of Zhang, Y. *et al.* (*Biochim. Biophys. Acta* **2010**, 1797, 457-465), which suggested that IsiA likely contains 15 Chls. Modeling studies of various optical spectra of the CP43′ ring using the uncorrelated EET model (Zazubovich, V.; Jankowiak, R. *J. Lumin.* **2007**, 127, 245-250), suggest that CP43′ monomers (in analogy to the CP43 complexes of PSII core) also possess two quasi-degenerate low-energy

states, A′ and B′. The site distribution functions of state A′ and B′ maxima/full width at half maximum (FWHM) are at 684 nm/180 cm^{-1} and 683 nm/80 cm^{-1}, respectively. Our analysis shows that pigments mostly contributing to the lowest-energy A′ and B′ states must be located on the side of the CP43′ complex facing the PSI core, a finding that contradicts the model of Zhang *et al.*, but is in agreement with the model suggested by Nield *et al*. (*Biochemistry* **2003**, 42, 3180-3188). We demonstrate that the A′-A′ and B′-B′ EET between different monomers is possible, though with a slower rate than intra-monomer A′-B′ and/or B′-A′ energy transfer.

2.1 Introduction

Cyanobacteria account for more than half of the total photosynthetic productivity on Earth, and can be found in almost every conceivable environment, including most marine and freshwater habitats.[1] One of the main reasons that cyanobacteria have become so ubiquitous is that their strong and effective regulatory mechanisms maintain high photosynthetic production levels under various conditions of illumination or nutrient stress.[2] Their adaptation to low-iron environments is an important example. When grown under iron-deficient conditions, the cyanobacterial phycobiliprotein content and Photosystem I (PSI) to Photosystem II (PSII) ratio are reduced. To compensate for this, some cyanobacteria express the *IsiA* gene product. Multiple copies of chlorophyll a (Chl a) binding IsiA protein surround the PSI trimer to compensate for PSI content decreases under the iron-stress conditions.[3-5] This protein is a genetic homologue of PsbC, the CP43 protein of the PSII core, associated with the water-splitting and oxygen-evolving enzyme of photosynthesis. Therefore, it is often called CP43′.[4-6]

Although CP43 and CP43′ have high amino acid sequence homology, they show some key differences. Indeed, in addition to different mass due mainly to a marked shortening of the large E loop on the luminal side of CP43′, the His ligand that binds Chl 46 in CP43 is replaced

with Gln in CP43′ of *Synechocystis* PCC 6803, and a Met residue, which has been implicated as a possible ligand in Chl 37 of CP43, is converted to a Phe in CP43′.[7] Both of these Chls have been suggested to play important roles in the excitation energy transfer (EET) dynamics of CP43, so comparison of the EET properties of these two protein complexes is of great interest.

A breakthrough in understanding the association of the proteins belonging to the core antenna family within the PSI core occurred a decade ago when two laboratories, using electron microscopy, discovered simultaneously that a supercomplex of trimeric PSI is encircled by a ring of 18 IsiA proteins in two different cyanobacterial species (*Synechocystis* PCC 6803[3,7] and *Synechococcus* PCC 7942[8]) when grown under limiting iron conditions. It has been established that while the whole PSI-CP43′ supercomplex has a diameter of 320 Å and a thickness of 90 Å, each of the 18 CP43′ monomer has a width of about 24 Å and a 20^{o} inclination relative to its neighbors.[9,10] Until now, much work has been dedicated to unraveling the spectroscopic properties and structure-function relationships in these complexes.[4,5,11-29]

The addition of the 18-mer CP43′ ring to PSI is an evolutionary adaptation to the reduction of the amounts of PSI and phycobilisomes under low-iron conditions, and it increases the light-harvesting efficiency of the PSI complexes by at least 70%.[3,4,7,8] Many studies using different spectroscopic methods have revealed that the CP43′ ring can transfer energy very effectively to the PSI core.[4,5,7,8] In addition, some groups have suggested that photoprotection of PSI (though PSI is not particularly prone to photodamage) and PSII under unfavorable environmental conditions might be the main function of CP43′ complex[18,21]. Although significant progress has been made in our understanding of these complexes, many open issues remain. For example, the number of Chls constituting a CP43′ monomer is still under debate. It is most often assumed to be the same as the number of pigments present in the CP43 complex.

However, the latter number has varied over time.[30-32] For example, in 2001, the 3.8 Å resolution X-ray structure of a cyanobacterial PSII core[30] revealed the presence of 12 Chl *a* molecules per CP43 monomer. In 2004, the crystal structure of a cyanobacterial PSII core complex at 3.5 Å resolution[31] suggested that each monomer has about 14 Chls. However, more recent structural data obtained at 3.0 Å[32], 2.9 Å[33], and 1.9 Å[34] resolutions, respectively, established that the number of Chls is 13. In contrast, Ref.[5] suggested 16-17 Chls per CP43´ monomer in another cyanobacterium (*Synechococcus* PCC 7942), while the modeling studies discussed in Ref.[10] proposed that each IsiA in the PSI- CP43′ supercomplex from the *Synechocystis* PCC 6803 binds 15 Chls. The latter value was obtained from calculations of optimal energy transfer within the PSI-CP43′ supercomplex.

In the present study, we show that each monomer of CP43′ complex most likely possesses 13 Chls, in agreement with the number of pigments in CP43 of PSII,[32,34] and energy transfer between quasi-degenerate states with uncorrelated site distribution functions (successfully applied previously to explain the various optical spectra of CP43 of PSII[6,35]) can be used to explain the electronic structure and EET in the ring of CP43′ complexes. Regarding the structure of the PSI-CP43′ supercomplex (*i.e.,* the orientation of CP43′ monomers and the PSI trimer in relationship to each other), we argue below that our data are consistent with the model suggested by Nield *et al*.[9] and not with the model proposed recently by Zhang *et al.*[10]

2.2. Experimental section

2.2.1. Sample isolation procedure

All glassware used for cell-growth was first washed with dilute HCl (0.01 times commercial, concentrated HCl) to eliminate any iron adhering to the glass. A pre-culture of cyanobacteria at an optical density of about 1.0 (at 600 nm) was grown for two days in BG-11 mineral medium, lacking iron-containing compounds, and then it was diluted 15 times in the same medium to set the culture at an optical density of 0.1 (at 600 nm). The cultures were then grown for 21 days and harvested by centrifugation at 13800 × g for 15 min at 4°C. For the isolation of CP43′ complex, Synechocystis psaFJ-depleted mutant cells[36] were used (this mutant synthesizes much lower amounts of PSI, thus reducing the risk of PSI contamination). Approximately 15 g cells (wet weight) were suspended in 50 mM MES-NaOH, pH 6.0, 25% (w/v) glycerol, 5 mM $CaCl_2$, and 5 mM $MgCl_2$ at a ratio of 10 mL of buffer per 1 g of cyanobacteria. The suspension was then centrifuged at 13800 × g for 15 min at 4°C, the pellet was suspended in the same original buffer volume with 1 mM PMFS (Sigma), and 50 μm/L DNAase (Roche Diagnostics, Mannheim, Germany) was added. The cells were then broken by sonication (Ultrasonic Processor XL2020, Heat System) for 45 min. Cycles of 1 min and 30 s sonication and 1 min storage of the tubes on ice were employed to avoid sample overheating. The resultant cell extract was clarified by centrifugation at 121 × g for 5 min at 4°C to eliminate any cell debris and large particles. The supernatant was finally centrifuged at 13900 × g for 35 min at 4°C, and the pellet contained thylakoid membranes.

2.2.2. Isolation of CP43′ complex

The above pellet was incubated with the same buffer (without PMFS and DNAase), supplemented with 1 M guanidinium chloride (GuCl) for 30 min at 4°C, with gentle stirring to eliminate most of the phycobillisomes that contaminate the sample. The incubation was followed by a second centrifugation, and the resultant pellet was washed 1-2 more times under the same conditions until the supernatant was almost colorless. The final treated thylakoid membranes were resuspended in 20 mM Bis-TRIS, pH 6.5, 10 mM $MgCl_2$, 20 mM NaCl, 15 mM $MgSO_4$, and 1.5% (w/v) Taurine, and then assayed spectrophotometrically for Chl a using an ε_{663nm} = 86 mM^{-1} cm^{-1} after pigment extraction with 80% (v/v) acetone[37]. The thylakoid membranes were next diluted to 0.15 mg Chl/ml with the same buffer, treated with 1% (w/v) n-dodecyl β-D-maltoside (DM) for 1 h at 4°C, and centrifuged at 9000 × g for 10 min at 4°C. The resultant supernatant was loaded onto a weak anionic-exchange, DEAE (Toyopearl TSK DEAE 650s) column, pre-equilibrated with 20 mM Bis-TRIS, pH 6.5, 10 mM $MgCl_2$, 20 mM NaCl, 15 mM $MgSO_4$, 1.5% (w/v) Taurine, and 0.03% (w/v) DM. The bound green material was washed with about three column volumes of the same buffer and eluted with a 90-550 mM $MgSO_4$ continuous gradient in the same buffer. Fractions at around 250 mM $MgSO_4$ (2 mL each) with maxima at 671.5 nm (fractions with higher wavelength peaks contained some PSI core contamination as assayed by antibodies against the PSI core A protein subunit and were discarded) were saved and dialyzed overnight against 20 mM Bis-TRIS, pH 6.5, 10 mM $MgCl_2$, 20 mM NaCl, 15 mM $MgSO_4$, 1.5% (w/v) Taurine, and 0.01% (w/v) DM. After concentrating about 10 times with Centriprep tubes (30000 MWCO, Millipore), the sample was loaded onto a continuous sucrose

gradient in buffer containing 20 mM Bis-TRIS, pH 6.5, 10 mM $MgCl_2$, 20 mM NaCl, 15 mM $MgSO_4$, 1.5% (w/v) Taurine, 0.01% DM, 0.5 M sucrose, and 4 M GuCl. To make the gradient, 10 mL of buffer solution (supplemented with 0.5 M sucrose) was put into ultracentrifuge tubes, frozen at □20°C for at least 12 h, and then slowly thawed at 4°C. This procedure formed a sucrose gradient with higher density sucrose at the bottom of the tubes. The concentrated sample from above was supplemented with 4 M GuCl, 0.5 mL of sample was loaded onto each tube, and the tubes were then centrifuged at 180000 × g (SW 41Ti rotor, Beckman) for 6 h at 4°C. Two main green bands were observed in the gradient. The band at higher density (faster mobility) was removed and dialyzed overnight against 20 mM Bis-TRIS, pH 6.5, 10 mM $MgCl_2$, 20 mM NaCl, 15 mM $MgSO_4$, and 0.01% (w/v) DM. It had an absorption maximum at 671.5 nm. This preparation was then loaded onto a new DEAE 650s chromatography column, pre-equilibrated with the same dialysis buffer. Under these conditions CP43′ passed straight through the column, and it was subsequently loaded onto a Q-Sepharose (a strong anionic-exchange resin; GE Healthcare) column pre-equilibrated with 50 mM TRIS-HCl, pH 7.8, and 0.03% (w/v) DM. The column was washed with the same buffer, and then with buffer supplemented with 50 mM $LiClO_4$. After washing, green material was eluted with a 50-300 mM $LiClO_4$ gradient in the same buffer. The fractions obtained at around 200 mM $LiClO_4$ were pooled and constituted purified CP43′ complex. The room temperature absorption maximum and the 77K origin fluorescence band of pure CP43′ ring material were at 671.5 and 685 nm, respectively.

2.2.3. Isolation of PSI-CP43′supercomplex

The isolation of PSI-CP43′ supercomplex was performed as described above with some important modifications. Wild type *Synechocystis* PCC 6803 was used instead of the *psaFJ*-depleted mutant since the former contains much more PSI under iron-starvation conditions. Everything was done as explained before, except that only the fractions from the first DEAE column at around 350 mM $MgSO_4$ (with absorption peaks at around 673 nm) were collected, concentrated, and loaded onto the sucrose gradient tubes. After centrifugation, two main green bands were observed. The lower one was collected and dialyzed against buffer containing 20 mM Bis-TRIS, pH 6.5, and 0.01% (w/v) DM. This sample constituted the PSI- CP43′ supercomplex, which had an absorption peak at 673 nm and two low-temperature fluorescence bands. The smaller fluorescence band was at 686 nm (due to CP43′) and the larger one was at 722 nm (due to PSI).

2.3. Results

2.3.1. Room-temperature absorption spectra and SDS-PAGE of CP43′and PSI-CP43′complexes

The room-temperature absorption spectrum of CP43′ in the 350-750 nm spectral range showed a maximum peak in the red at 671.5 nm (Figure 2-1 frame A). Longer wavelength maxima indicate some contamination with PSI complex, and a shorter maximum wavelength is an indication of the presence of some Chls disrupted from their native protein environment. The PSI- CP43′ supercomplex displayed a maximum in the red at around 673.0 nm (Figure 2-1 frame B), due to the presence of the PSI trimer, which absorbs at a longer wavelength than CP43′. Note that the PSI-CP43′ 673.0 nm band is also much broader than that of the CP43′ complex. The SDS-PAGE (12% w/v acrylamide) protein analysis (Coomassie Blue staining) demonstrates the

high purity of our preparations in term of protein content. Indeed, the CP43′ complex contains only the IsiA polypeptide at around 34 kDa (Figure 2-1 A), and the PSI-CP43′ preparation contains two main bands, one at around 34 kDa due to the IsiA protein and the other at around 66 kDa due to the PsaA and PsaB polypeptides of PSI (Figure 2-1 B).

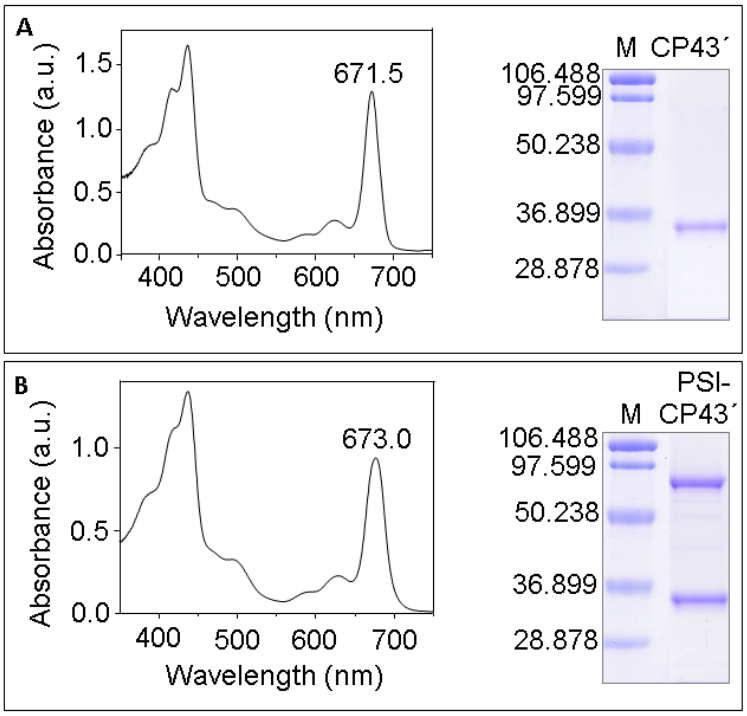

Figure 2-1 Room-temperature absorption spectra in the 350-750 nm spectral range and SDS-PAGE protein analysis of CP43′ complex (Frame A) and PSI-CP43′ supercomplex (Frame B) used in this study. M: molecular weight markers.

2.3.2. Low-temperature absorption and emission spectra

Absorption (curve 1) and emission (curve 2) spectra (T = 5K) of isolated CP43′ rings are shown in Figure 2-2. The absorption spectrum with a maximum near 669.3 nm also shows two broad shoulders near 675 and 681-682 nm. This spectrum is similar to that obtained indirectly as a difference between the absorption spectra of PSI-CP43′ supercomplex and PSI trimeric core

from *Synechocystis*.[28] However, the 675 and 681-682 nm bands were hardly visible in the 5 K absorption spectrum reported for the CP43′ complex from *Synechococcus* PCC 7942.[5] We also note that the intensity of the ~681-682 nm shoulder is sample dependent and decreases in partly damaged samples.

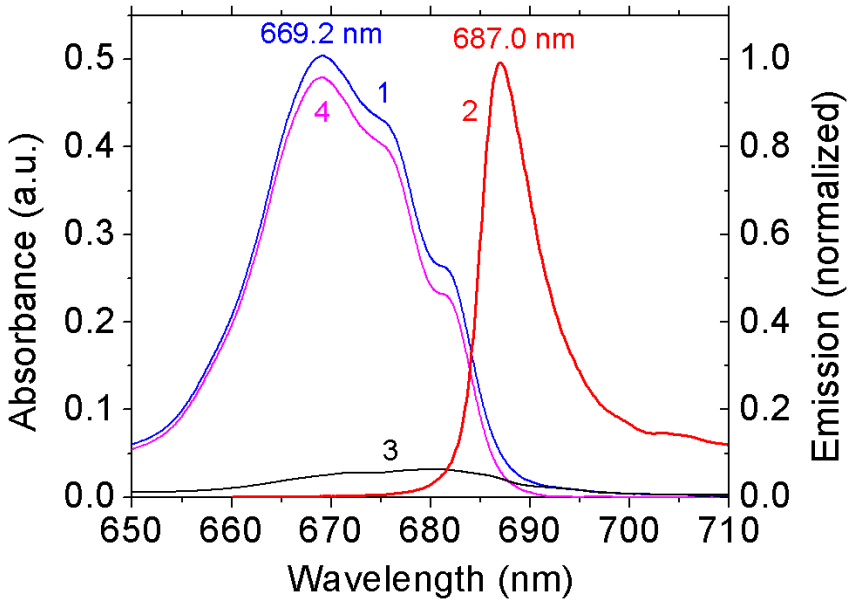

Figure 2-2 Q_y-region 5K absorption (curve 1) and fluorescence (curve 2) spectra of isolated CP43′. Since curve 1 is partly (~8-9%) contributed to by residual PSI (curve 3), curve 4 (4 = 1 - 3) represents the pure CP43′ absorption spectrum. Emission was obtained with an excitation wavelength (λ_{ex}) of 496.5 nm and an excitation laser intensity (I) of 100 μW/cm^2 (collection time 60 sec).

Curve 1 in Figure 2-2, however, appears to possess a small contribution from the PSI trimer. That is, absorption in the long wavelength region (>695 nm) originates exclusively from the PSI complex. To estimate the PSI contribution, the absorption spectrum of the PSI complex[28] (curve 3) was normalized with the CP43′ sample absorption spectrum (curve 1) in the 695-700 nm region. The difference spectrum (curve 4 = 1 - 3) corresponds to the absorption spectrum of "pure" (*i.e.*, without PSI contamination) CP43′ complexes. The integrated area of curve 3 is only

about 8-9% of spectrum 1. Thus, in the following analysis we assume that curve 4 is the absorption of pure CP43′ complex. The emission spectrum (curve 2) in Figure 2-2 peaks at 687.0 nm with a FWHM of ~7 nm, which is very similar to data reported in[18] for the CP43′ complex isolated from *Synechocystis* PCC 6803.

However, different emission peak positions have been observed for isolated CP43′ rings. For example, Andrizhiyevskaya *et al.* [5] observed a fluorescence origin band in CP43′ from *Synechococcus* near 682 nm, while the emission band was shifted to 685 nm in the PSI-CP43′ supercomplex. The authors of Ref.[5] attributed this shift to EET among the CP43′ monomers and/or pigments-pigment interactions between the monomers, or between the CP43′ and PSI complexes in the PSI-CP43′ supercomplex. A 685 nm fluorescence band was also observed in CP43′ (*Synechocystis*) in Ref. [18] These PSI-CP43′supercomplexes, [18] however, could lack some of the 18 CP43′ subunits normally present in intact supercomplexes. We will return to this issue in the modeling section (section 4.5) where the excitation energy transfer (EET) between quasi-degenerate low-energy states with uncorrelated site-distribution functions (SDFs)[6,35] within an individual CP43′ complex, and between the CP43′ subunits within the supercomplex, is discussed in detail. Here it is sufficient to say that our CP43′ and PSI-CP43′ complexes show emission bands with a maximum near 687 nm and 687/720 nm, respectively, and that our 687 nm band and 685 nm the band from [26,28] have similar origins.

Figure 2-3 shows normalized (near 700 nm) 5 K absorption spectra of the PSI-CP43′ supercomplex (black; curve 1) and isolated PSI trimer sample[28] (blue; curve 2). Curve 3 is the difference between spectra 1 and 2 and is ascribed to the absorption spectrum of the pure CP43′ complex. As expected, the difference spectrum closely resembles curve 4 in Figure 2-2 (which is

also seen in Figure 2-3 for easy comparison), proving that isolated CP43′ ring and CP43′ residing within the PSI-CP43′ supercomplex have nearly indistinguishable absorption spectra.

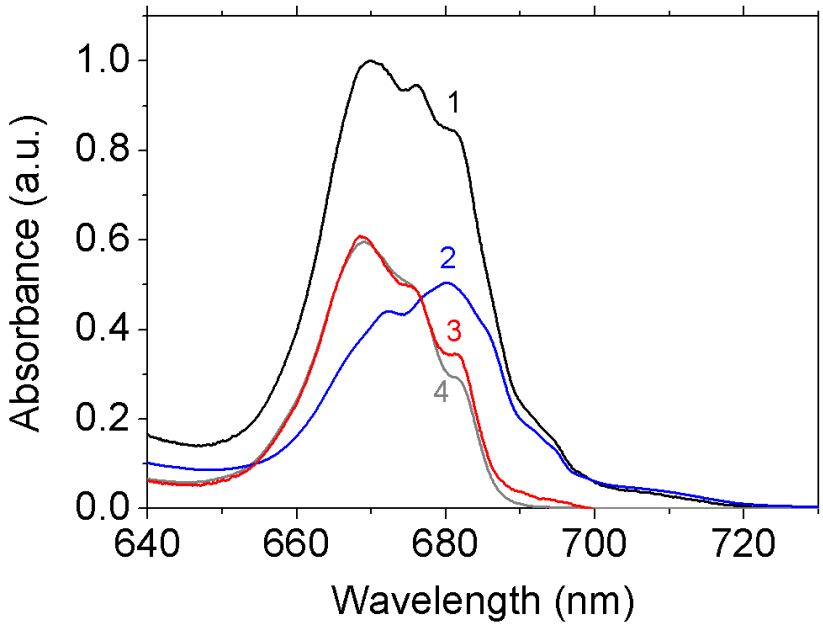

Figure 2-3 5 K absorption spectra of PSI-CP43′ supercomplex (black; curve 1) and PSI[28] (blue; curve 2), and their difference ascribed to pure CP43′ (curve 3). Curve 4 (gray spectrum) is shown for comparison and corresponds to spectrum 4 from Figure 2-2.

2.3.3. Nonresonant persistent and transient hole-burned (HB) spectra

The nonresonant HB spectra obtained with an excitation wavelength of 496.5 nm for the CP43′ complex are shown in Figure 2-4. The low-energy part of the absorption spectrum, which is similar to the absorption spectrum of CP43 of PSII,[6,38-40] is plotted for reference. Spectra labeled 1-8 correspond to the nonresonant HB spectra. At very low fluence (f = 12 J/cm^2), a shallow hole (see curve 1) is observed at ~686.7 nm with a hole-depth of ~2%. When this hole is saturated (see curve 8; f = 7.7 kJ/cm^2), the hole peak position shifts from 686.7 to 685.3 nm, and its depth increases to ~17%. Fluence-dependent (blue-shifted) anti-holes are also observed, in agreement with the non-photochemical nature of persistent hole burning. Since contamination by

PSI trimer is very small, no persistent hole(s) typical of PSI trimer and/or PSI-CP43′ complexes are observed. Sample with a less intense ~681-682 nm shoulder in absorption showed significantly blue shifted nonresonant holes and emission spectra (data not shown). We will argue below that such behavior is consistent with a lack of efficient EET between subunits of the CP43′ supercomplex ring.

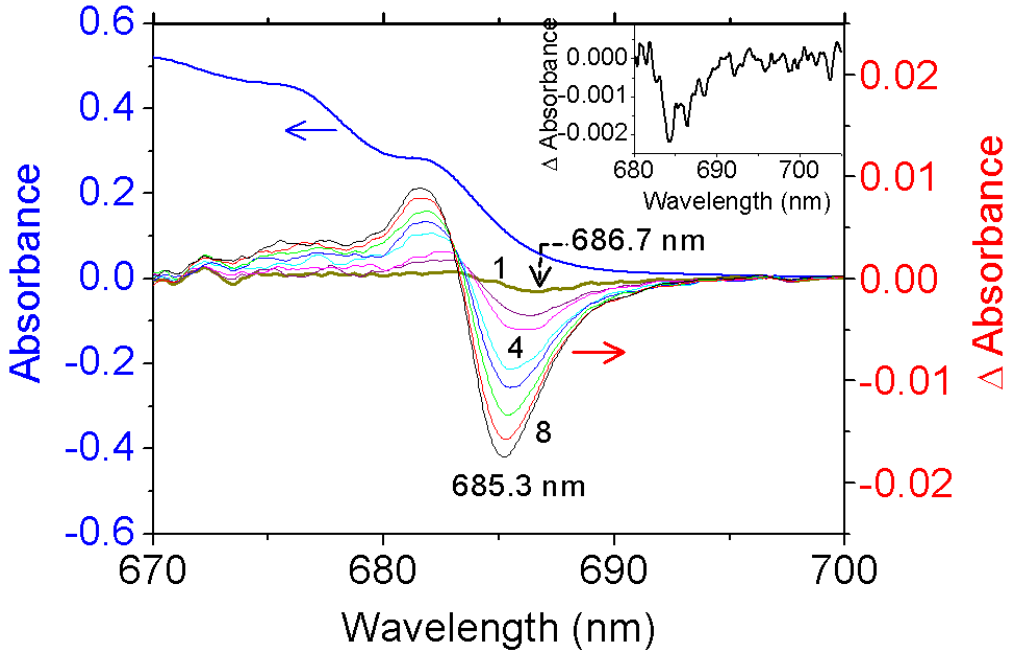

Figure 2-4 The main frame shows the absorption spectrum (top) and HB spectra (labeled 1-8) obtained for CP43′ complex at 5 K (λ_B = 496.5 nm). The fluences used for the shallow (curve 1) and saturated (curve 8) holes were 12 J/cm^2 and 7.7 kJ/cm^2, respectively. The inset shows the transient HB spectrum.

The inset in Figure 2-4 shows a very shallow transient hole spectrum (hole depth of ~1.3%; obtained with I = 600 mW/cm^2), which is the difference absorption spectrum generated with the laser on and with the laser off, measured after the persistent hole (see curve 8 in the main frame) is saturated. The transient hole reflects the extent of the population accumulated at the triplet

bottleneck state via intersystem crossing from the excited singlet state and is further discussed in section 4.6.

2.3.4. Fluence dependence of the emission spectra

We turn now to fluorescence spectra obtained at different stages of nonresonant HB. All emission spectra in Figure 2-5 were obtained with low laser intensity (I =100 μW/cm^2, integration time = 60 sec). Spectrum 1 represents the emission of an unburned sample, while spectra 2-6 were obtained after various stages of nonresonant HB, as shown in Figure 2-4. Curves 2-6 show that with increasing bleaching, the integrated fluorescence intensity decreases, and the emission maximum shifts blue to about 686 nm. This is an indication that there are at least two states/pigments involved in the resulting emission, with somewhat different fluorescence yields. We believe that spectrum 1 in Figure 2-5 originates from the lowest-energy state(s) of intact CP43′ complexes. The position of the emission band near 687 nm does not depend on fluence as long as the fluence is kept lower than ~12 J/cm^2. The same emission maximum was measured for the intact PSI-CP43′ supercomplex (data not shown). However, in the latter case, due to an efficient EET to the PSI trimer, an additional strong band with a maximum near 720 nm was observed that originates from the PSI emission in agreement with Refs.[18,28] (Electronic structure and EET dynamics of the PSI-CP43′ supercomplex will be discussed elsewhere).

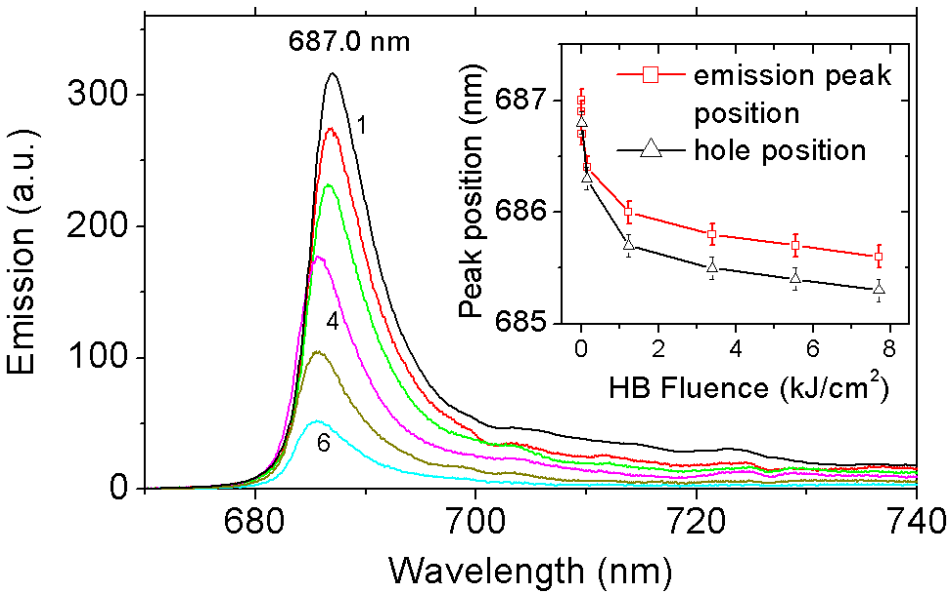

Figure 2-5 5 K fluorescence spectra obtained with CP43′ at different stages of nonresonant hole burning. All emission spectra (labeled 1-6) were obtained with a laser excitation intensity of 100 μW/cm^2 (collection time 60 sec). The inset shows the emission maxima (open circles) and nonresonant hole minima (open triangles) as a function of HB fluence. The excitation wavelength was 496.5 nm for both the HB and emission measurements.

As mentioned above for the HB data, the blue shift of the emission upon burning can be explained assuming that the pigments contributing to the lowest-energy state are continuously burned and, on average, blue-shifted. Moreover, the resulting emission originates, to a progressively larger extent, from the low-energy state or states with modified composition (preferentially localized on Chl molecule(s) at different position within the complex). The nature of these low-energy states will be discussed below, as it is more complicated than that in the (monomeric) CP43[6] (due to the ring structure of the CP43′ complex where EET within a monomer subunit and between neighboring monomers must be possible). The inset in Figure 2-5 shows the position of the nonresonant hole (Figure 2-4) and the emission band (main frame of Figure 2-5) as a function of fluence. Note that emission maxima shown in Figure 2-5 vary more

or less in concert with the minima of the non-resonant holes as a function of HB fluence, and the largest shifts take place at the early stage of burning. Interestingly, similar dynamics of fluence-dependent emission are also observed in the PSII core and the CP47 complex from spinach.[41] The origin and shape of these fluorescence spectra are further discussed in section 4.

2.3.5. ZPH action spectrum and nonresonantly burnt holes

To gain additional insight about the properties of the isolated CP43′ ring, we measured the zero-phonon hole (ZPH) action spectrum, which shows the dependence of the hole depth on the burn wavelength for a fixed burning dose.[28,42] It has been shown before[28] that this type of spectrum can resolve possible contributions to the lowest-energy states of photosynthetic complexes. The ZPH action spectrum (see inverted sharp peaks) of the CP43′ complex (obtained with a constant f = 2.4 J/cm^2) is presented in Figure 2-6. The depth of these holes is smaller than 10%, and the holes were burnt from long wavelength to short wavelength to reduce the contribution from the broad nonresonant low-energy holes. In Figure 2-6, however, the amplitudes of the holes were normalized to the low-energy wing of the absorption spectrum. The ZPH action spectrum has a maximum near 684 nm, which is about 2-3 nm blue shifted in comparison to the shallow nonresonant hole shown in Figure 2-4 or the emission peak in Figure 2-5. The peak of the ZPH action spectrum is closer to the position of the saturated hole at 685.5 nm, suggesting that something besides the lowest-energy (very weak) 686.7 nm state contributes to the action spectrum under our experimental conditions.

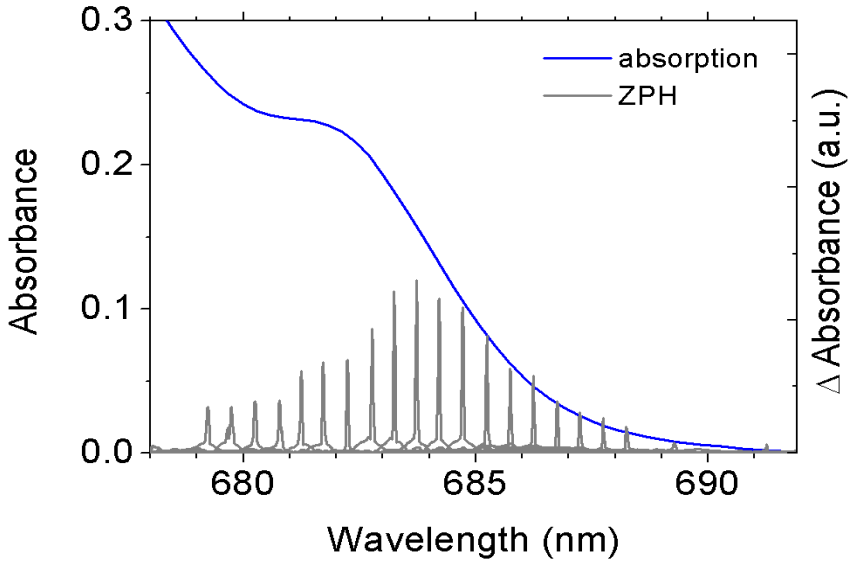

Figure 2-6 The solid curve is the corrected absorption spectrum of CP43′ from Figure 2-2 (curve 4). The gray sharp spikes correspond to an inverted ZPH action spectrum. The holes were burnt with a fixed fluence of 2.4 J/cm^2. See the text for details.

To obtain more information about the nature of the lowest-energy states, we present the saturated resonant holes (obtained with a fluence of 90 J/cm^2) in Figure 2-7 (curves 1 – 4). The burning wavelengths for each of the four spectra are shown in the caption. Curve 4 is clearly composed of the ZPH and a pseudo-phonon sideband. Higher-energy excitations (curves 1 and 2) clearly reveal an additional contribution to the low-energy part of the hole structure (compare the different shapes/bandwidths of the low-energy holes) due to interference from the lowest-energy state(s) bleached by downhill EET. Especially in the hole spectrum with λ_B = 682.7 nm (curve 1), one can see two apparent lower-energy components indicated by two vertical arrows. The shoulder (dashed arrow) near 683.8 nm (located about 20 cm^{-1} from the ZPH) corresponds to the pseudo-phonon sideband. The broader band near 685.3 nm (solid arrow) is due to downhill EET, in agreement with the 685.3 nm saturated hole obtained with an excitation of 496.5 nm (see curve 8 in Figure 2-4). This supports our earlier suggestion that the ZPH action spectrum shown

in Figure 2-6 does not reflect exclusively the lowest-energy state(s). The top spectrum in Figure 2-7 (dashed line) is a shallow HB spectrum (similar to curve 1 in Figure 2-4). Note that its position is near 686.7 nm and likely corresponds to the lowest-energy state. Below we introduce a model of uncorrelated EET within the subunits of the CP43′ ring, which can be used to explain the above optical spectra obtained for the CP43′ ring.

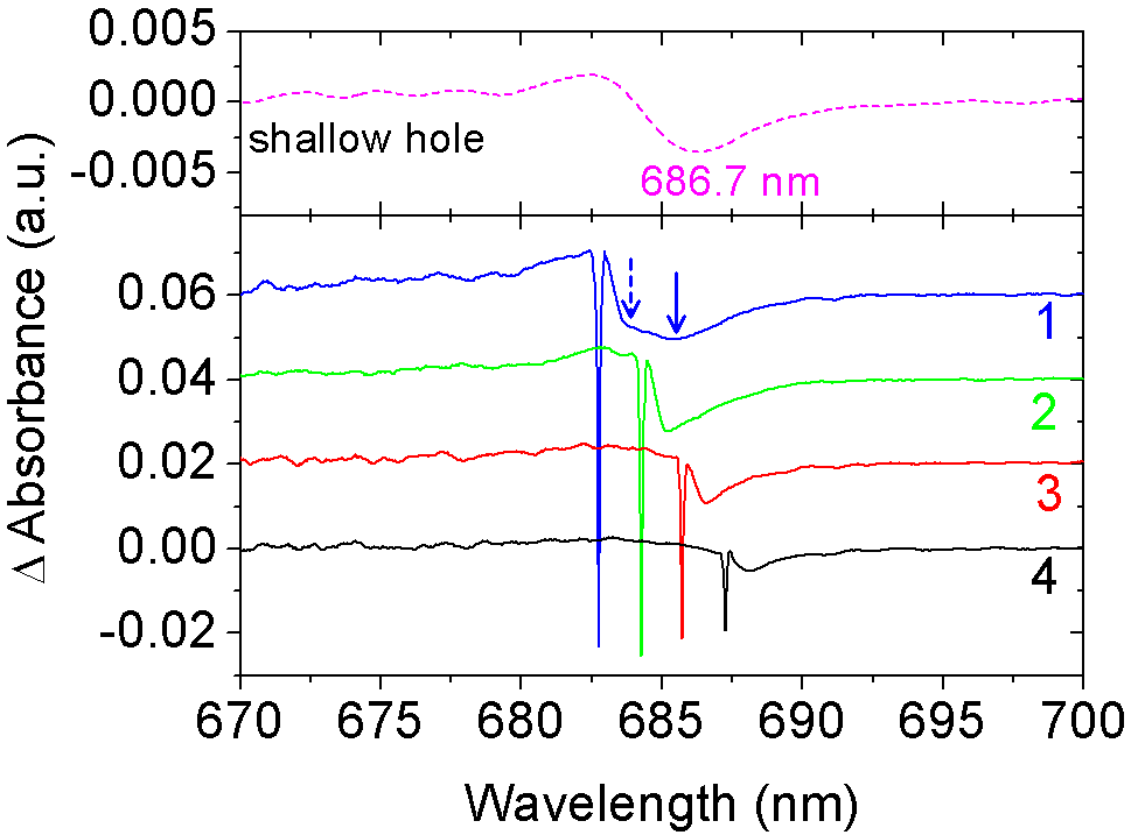

Figure 2-7 Spectra 1 – 4 are resonant HB spectra obtained for CP43′ complexes at 5 K. Four different λ_{Bs} were used: 682.8 nm (1), 684.3 nm (2), 685.8 nm (3), and 687.3 nm (4). All spectra are offset vertically for clarity. The burn dose was 90 J/cm^2 for each spectrum (0.5 cm^{-1} resolution). The nonresonant (nonsaturated) HB spectrum (the pink dashed curve at the top, which is similar to curve 1 in Figure 2-4, and obtained with λ_B = 496.5 nm and a burn dose of 12 J/cm^2) is shown for comparison.

2.4. Discussion

2.4.1. Number of Chl a per CP43′ subunit

The size of our PSI-CP43′ supercomplex particles, based on negative-staining TEM data obtained at NREL (data not shown), is consistent with the literature data,[3] *i.e.*, a supercomplex studied in this work is composed of one PSI trimer and 18 CP43′ monomers. Assuming there are 288 Chls in the PSI core trimer and 18 copies of CP43′ encircling the PSI,[3,43] the approximate number of Chl *a* per CP43′ subunit can be derived by deconvoluting the absorption spectrum of the PSI-CP43′ supercomplex into CP43′ and PSI components, as shown in Figure 2-3. (All spectra were measured under identical conditions with 4 cm^{-1} resolution). A comparison of the integrated absorption of the CP43′ (curve 3) and PSI (curve 2) spectra in Figure 2-3 reveals, assuming 18 CP43′ subunits per supercomplex,[3] that there are about 13 (±1) Chls in each CP43′ monomer (*i.e.*, the same number of pigments as found in the CP43 complex of PSII).[32] Different numbers of pigments per CP43′ monomer were reported by different groups; for example, 10 Chl *a* per subunit were observed in[28] for *Synechocystis*, although comparison of the data from[28] with the spectra reported in the current work demonstrates (data not shown) that the CP43′ preparation studied in[26] was significantly contaminated with PSI complex; as a result, the number of Chls was underestimated. By the same token, results for *Synechococcus*,[5] in which the Chl *a* content was estimated at 17-18, could be explained assuming that the number of CP43′ subunits is higher than 18 per PSI trimer. Formation of a second CP43′ ring around the first one has been observed in case of prolonged iron stress. [26]

2.4.2. On the relative orientation of Chls in the CP43′ring with respect to the PSI trimer – structural considerations

The available models of the PSI-CP43′ supercomplex are inferred from crystal structures of PSI and the CP43′ protein.[9,10] As structural data on CP43′ per se is yet unavailable, the CP43′ (IsiA) is modeled on the basis of a high-resolution crystal structure of CP43,[30] an antenna protein of PSII that is homologous with IsiA.[44,45] The current understanding of the mutual arrangement of CP43′ and PS I core complexes is based on relatively low-resolution (25 Å) electron microscopy data[7], which allows for considerable freedom in orienting CP43′ subunits in relation to the PS I core. As a result, two mutually-exclusive models exist. In the one by Nield *et al*.[9] the CP43′ subunits are oriented with the same side towards the core as CP43 is oriented with respect to the RC in PSII. Twelve Chls were included in the original Nield *et al*. model,[9] which was based on the result given by the low-resolution X-ray structure of PSII.[30] Later studies showed that CP43 may be associated with 13 or even 14 Chls.[31,32] The highest resolution X-ray data so far, however, reveals only 13 Chls per CP43 monomer.[34] This is in contrast with the recent work of Zhang and coworkers,[10] who suggest that CP43′ protein binds 15 Chls. Moreover, in Zhang's model the opposite side of the CP43′ subunit is facing the PSI core. This model is based on theoretical optimization of the energy transfer pathways in the PSI-CP43′ supercomplex. Below, we will refer to the models of Nield *et al*.[9] and Zhang *et al*.,[10] as models I and II, respectively. Although Zhang *et al*.[10] argued that model II is superior to model I with respect to the energy transfer potential (*i.e*., more Chls and Chl-Chl connections, and increased number of paths along which EET occurs[10]), model II appears to be inconsistent with many optical spectra obtained so far for CP43.[6,38-40,46,47] For example, it has been shown that the CP43 core antenna complex of PSII possesses two quasi-degenerate "red"-trap states, A and B,[6,38-40,46,47] The evidence for

similar lowest energy states in CP43′ has been presented by us in Ref[28]. For CP43, a model of uncorrelated EET between the quasi-degenerate bands has been proposed,[6,35] which is consistent with both experimental results and excitonic calculations.[48] The latter reveal that Chl 44 and Chl 37 (using Loll *et al.* notation[32]) are most likely contributing to the low-energy A and B states, respectively, in the CP43 complex.[48] From the viewpoint of optimizing EET from CP43′ to the PSI core under these conditions, Chls 44 and 37 should face the PSI core (model I), as the opposite CP43′ orientation would result in poor antenna performance. Therefore, in subsequent analysis, model I will be used, as this model provides orientation of Chls consistent with the spectroscopic data and previous modeling studies.[6,48]

Figure 2-8 illustrates relative positions of the Chls in model I with the 13th pigment (Chl 47) added based on the higher resolution crystal structure at 3.0 Å of PSII.[32,49] The pigments are numbered according to PDB file 2AXT. The Chls in PSI and CP43′ are represented by the Mg atoms (green circles) and chlorin rings, respectively. The blue-dotted ovals show regions where PSI pigments have the nearest distances to the CP43′ pigments, possibly involved in funneling excitation energy from CP43′ subunits to the PSI trimer. Note that in this structural arrangement Chls 37, 44, and 41 face the PSI complex. Chl 41 is located at the edge of the CP43′ monomer and close to the adjacent CP43′ monomer. Chl 37 and Chl 44 transition dipoles are 12^{o} and 20^{o} off the membrane plane, with their molecular planes perpendicular and almost parallel to the supercomplex radius, respectively. Chl 41 transition dipole is 29^{o} off the membrane plane, and its molecular plane is also parallel to the supercomplex radius. Model II, [10] with clearly labeled Chls, is shown in Appendix B. In model II each CP43′ monomer is associated with 15 Chls, with Chls 37, 41, and 44 placed on the exterior of the PSI-CP43′ supercomplex (*i.e.*, far from the CP43′-PSI interface). It is interesting to note that Chl 41 (close to the RC of PSII in the case of

CP43), according to model I, is located close to a neighboring CP43′ subunit. Hence, it could act as a linker in the inter-subunit (*i.e.*, inter-monomer) EET within the CP43′ ring. It is this inter-monomer EET that should account for the differences observed in the CP43′ emission and persistent/transient HB spectra (*i.e.*, the red-shift) in comparison to CP43, as illustrated below.

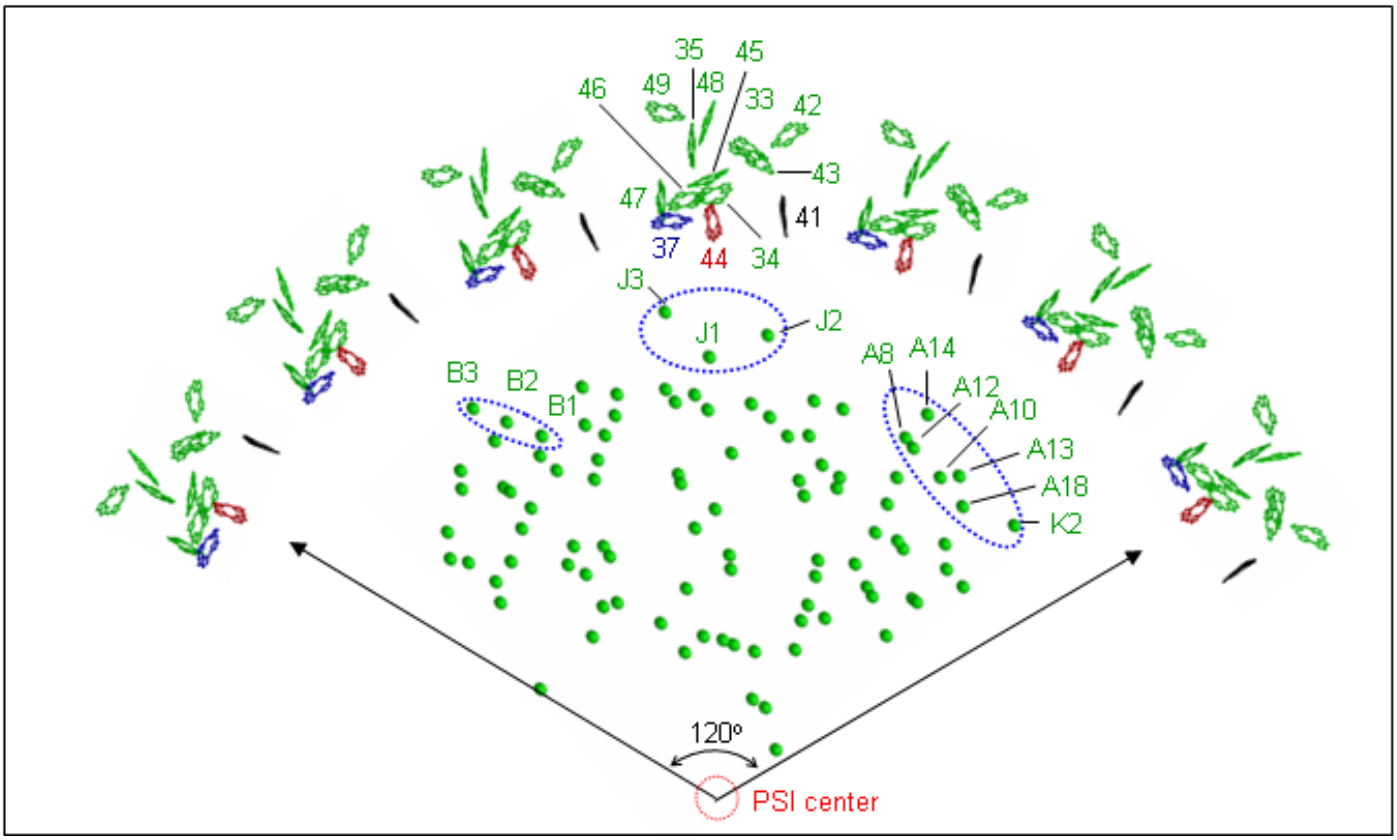

Figure 2-8 Pigment organization in the PSI-CP43′ supercomplex proposed by Nield *et al.*[9] with an extra Chl added (Chl 47) based on Ref.[32] The notation for the PSI pigments are given based on Ref.[43] For clarity, only part of the supercomplex is shown. The view is from the lumenal side. Blue, red, and black Chls correspond to Chls 37, 44, and 41, respectively. See the text for details.

2.4.3. Uncorrelated EET model within the CP43′ ring

As mentioned above, a model of the energy transfer between quasi-degenerate states with uncorrelated SDFs has been successfully applied to characterize the two lowest-energy states in CP43.[6,35] In this model, SDFs of the two Chl molecules (*i.e.*, pigments A and B) contributing to the lowest-energy absorption band of CP43 are uncorrelated, but the respective molecules are connected by relatively fast (~10 ps) excitation energy-transfer processes. In a given CP43 (Please see Appendix A for abstract and conclusions) complex, either of these two Chls could be lower in energy.[35] In the following discussion "pigments A and B" are going to be used as a shorter way of referring to pigments having dominant contribution to states A and B, and "bands A and B" are meant to represent absorption bands belonging to states A and B, respectively. The important feature of this model is that it explains the asymmetric shape of the HB action spectrum resulting from its being a superposition of the sub-SDF of the pigments A and B, which are the lowest-energy pigments in the individual complexes. These sub-SDF contributions to the action spectrum are red-shifted with respect to the true full SDF of the pigments A and B. States A and B of CP43 are assumed to be highly localized on Chls 44 and 37, respectively, with inter-pigment coupling of 5.8-7.6 cm^{-1}. Note that both of these states possess some excitonic character (as evidenced by CD and Stark-SHB data[39,40] and excitonic calculations[48]), but are preferentially localized on a lower site-energy pigment in a respective group. The possible reason(s) for the significant red shift in the transition frequency of the Chls contributing to the A and B bands could be due to H-bonding and/or different ligation state with protein environment.[48] In the following, we employ this EET model, with modifications accounting for the differences between the CP43 monomer and the CP43′ ring, to find out whether the optical spectra reported in section 3 can be explained. Specifically, with the CP43′ ring, one needs to consider the EET

between *neighboring* CP43′ monomers. In the CP43 complex (as discussed in Refs.,[6,35]), one of the two lowest-energy pigments (A or B) can only transfer energy to the other lowest-energy pigment (B or A) in the same CP43 unit. In contrast, in the CP43′ ring composed of 18 subunits (CP43′ monomers), each CP43′ unit is located at a very close distance (~10 Å) with respect to its two neighbors, and energy transfer between them is likely to occur.[9,10] In the case of CP43′, we refer to A′ and B′ pigments to distinguish from A and B pigments of CP43 complex. Therefore, in this case, every A′ pigment (of an individual subunit) has up to five potential energy acceptors (i.e., the B′ pigment of the same CP43′ monomer, as well as two A′ pigments and two B′ pigments of the two adjacent monomers). Similarly, every B′ pigment has up to five potential acceptors (*i.e.*, the A′ pigment of the same CP43′ monomer, as well as two B′ pigments and two A′ pigments of the adjacent monomers). Taking the above into account in the following subsections, we describe the model most suitable for the CP43′ protein, and verify whether one set of parameters can simultaneously fit the absorption, emission, persistent/transient holes, and ZPH action spectra of the CP43′ ring.

2.4.4. The absorption spectrum of isolated CP43′protein

Figure 2-9 shows the CP43′ absorption spectrum from Figure 2-2 corrected for PSI contamination (black curve). Curves a and b in Figure 2-9 are absorption spectra of states A′ and B′, respectively including contributions from delocalized protein phonons and localized Chl vibrations (according to Rätsep *et al.*[50]). For the best fit, we used the Huang-Rhys factor, $S = 0.6$, which is about two times larger than that in the analysis for CP43.[6] Considering maximal depths of the saturated ZPH (~ 42%) in Figure 2-7, the estimated upper limit for S could be as large as 0.8. The oscillator strength of the A′ band is 0.6 Chl equivalents. This is in agreement with

results of [6], where we did not explicitly report this number, although it was available. The oscillator strength of the B′ band is slightly larger than one Chl equivalent, again in implicit agreement with Ref. 6. Note that the low-energy part of the absorption spectrum can be fit very well with the sum of curves a and b. From the fit, parameters of possible SDFs of the A′ and B′ bands can be extracted. We note that somewhat different bandwidths and band positions can also yield a good fit to the low-energy wing of this absorption spectrum. However, the range of possible SDF parameters needs to be narrowed considerably in order to describe all experimental data reported above, including the emission and action spectra, as well as nonresonantly burned holes. That is, the best parameters revealed by our modeling studies (including those described in detail in the next section) are the SDF of band A′ ($SDF_{A'}$), which peaks at 684.0 nm and has a FWHM of 180 cm^{-1}, and the SDF of band B′ ($SDF_{B'}$), which peaks at 683.0 nm with a FWHM of 80 cm^{-1}. Interestingly, these two states have similar parameters to those previously reported for CP43′, where the two bands were found with absorption peaks/inhomogeneous widths of 683.9 nm/160 cm^{-1} and 682.6 nm/70 cm^{-1}, respectively.[28] In that study, however, information about these two bands had been obtained indirectly by fitting the CP43′ ZPH action spectrum, in turn obtained as a difference between the ZPH action spectra of PSI-CP43′ and PSI complexes. Compared with parameters reported for CP43 (A band: 682.9 nm/180 cm^{-1}; B band: 682.9 nm/62 cm^{-1}),[6] the CP43′ complex appears to have a red-shifted A′ band. This difference is reasonable if one takes into consideration slight differences in the protein sequence between CP43 and IsiA complexes.

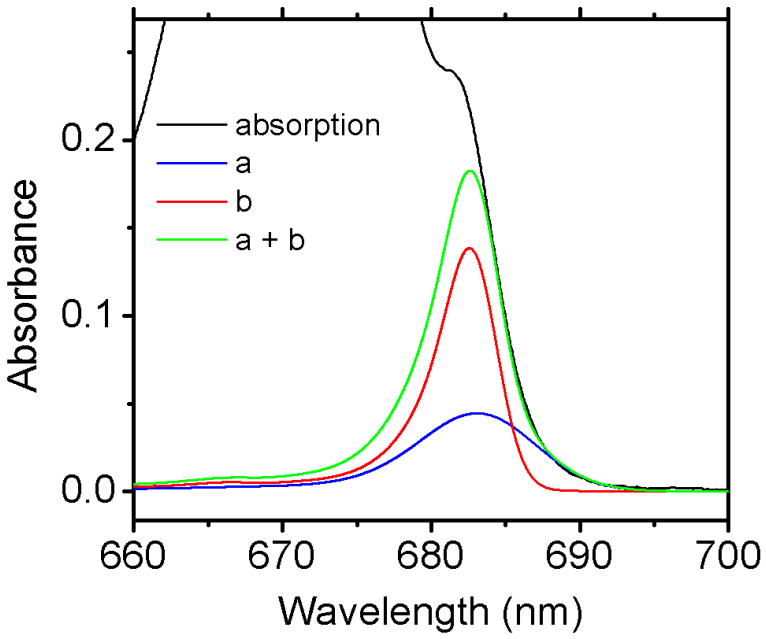

Figure 2-9 Fit of the long-wavelength region of the absorption of CP43′, with contributions from the two lowest-energy states: curve a for band A′ (peak at 684 nm with FWHM of 180 cm^{-1}) and curve b for band B′ (peak at 683 nm with FWHM of 80 cm^{-1}) dressed with phonons and vibrations.

2.4.5. The emission spectrum of isolated CP43′protein

The SDF profiles, derived from data shown in Figure 2-9, are (in a good approximation) the full "true" SDFs of the two lowest-energy pigments in CP43′. They are plotted in frames A and B of Figure 2-10, as curves a and b, respectively. In a particular CP43′ complex, either one of the two pigments could be lower in energy. In contrast to the absorption spectrum, where both the higher- and lower-energy sides are based on the "true" SDFs of the A′ and B′ bands, in isolated CP43 or CP43′ subunits, the emission and ZPH action spectra are mainly contributed to by the sub-ensembles of the two lowest-energy pigments, which are the lowest-energy pigments in their respective individual complexes and are incapable of further downhill EET. The SDFs for these sub-ensembles of A′ (or B′) in CP43′ can be calculated by multiplying the "true" SDF,

a (or b), by the respective probabilities that pigments with zero-phonon lines (ZPLs) at certain wavelengths are incapable of any downhill EET, that is, by the normalized integration curve of the "true" SDFs.[6,35] The resulting distributions are represented by curves f and e for bands A′ and B′, respectively.

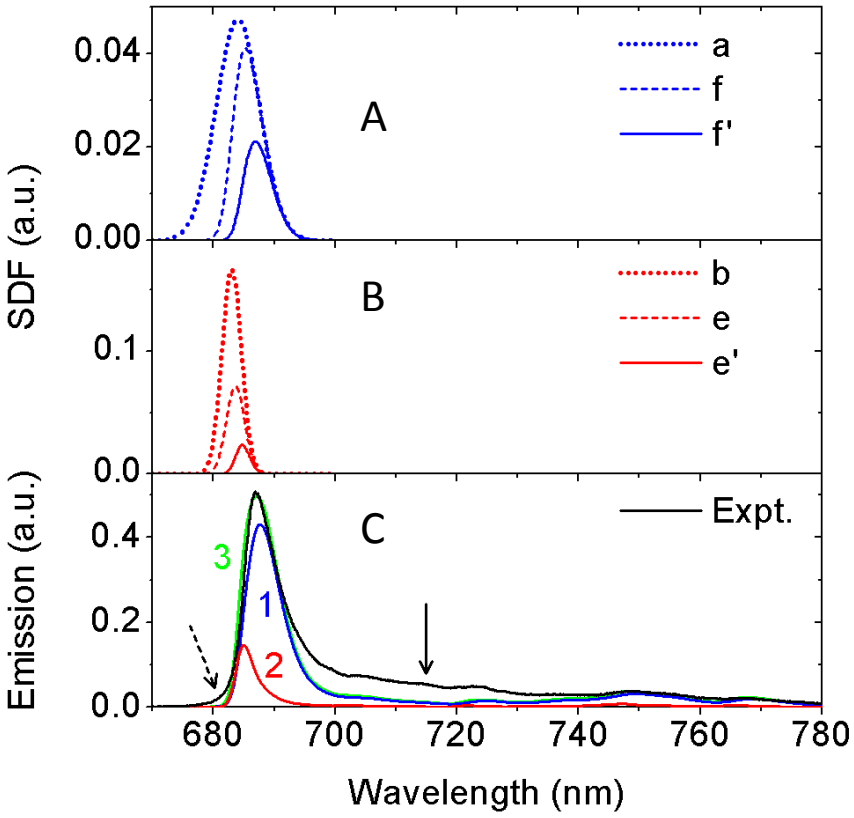

Figure 2-10 (Frame A) Curve a corresponds to the true SDF of band A′ in CP43′. Curves f and f ′ represent the sub-ensembles of band A′, without and with inter-monomer EET taken into account, respectively. (Frame B) Curve b corresponds to true SDF of band B′. Curves e and e′ represent sub-ensembles of band B′, without and with inter-monomer EET taken into account, respectively. (Frame C) Emission spectrum of CP43′ protein at 5 K (black curve). Curve 3 is the sum of curves 1 and 2 (corresponding to contributions of f ' and e' from frames A and B, respectively) dressed with phonons and localized Chl vibrations. For details about the discrepancy indicated by the dashed and solid arrows, see the main text.

In order to expand this discussion to *inter-monomer* EET within the CP43′ ring one has to consider the likelihood of various inter-monomer EET processes (A′-A′, B′-B′, A′-B′, B′-A′). Note that the diameters of the PSI-CP43′ supercomplex and CP43′ monomer are 320 Å and 48 Å, respectively.[3,9,10] In the ring composed of 18 CP43′ units, each monomer has a 20^{o} tilt relative to its neighbors. Therefore, the distances between identical Chl molecules in neighboring CP43′ monomers are about 40 Å. The shortest Chl-Chl distance between neighboring CP43′ monomers is, however, only about 10 Å.[9] Furthermore, using Chl coordinates from the X-ray structure of PSII (PDB 2AXT[32]), the distance between Chl 44 and Chl 37 inside a monomer is about 23 Å, compared to about 45 Å between Chl 37 and 44 pigments of two neighboring monomers. The inter-pigment couplings, for pigments relevant within the structural Model I, are presented in Table 2-1. We note that in this range of couplings Förster approximation must be valid.

Table 2-1 The couplings (in cm^{-1}) between relevant Chl a molecules (Model I) within and between adjacent CP43′ subunits. μ^2=18.5 D.

		Monomer 1			**Monomer 2**		
		Chl 37	**Chl 41**	**Chl 44**	**Chl 37**	**Chl 41**	**Chl 44**
Monomer 1	**Chl 37**	0	1.52	5.74	-1.77	0.09	0.02
	Chl 41	1.52	0	-16.72	-1.06	1.11	-2.55
	Chl 44	5.74	-16.72	0	-1.03	-0.29	1.10
Monomer 2	**Chl 37**	-1.77	-1.06	-1.03	0	1.52	5.74
	Chl 41	0.09	1.11	-0.29	1.52	0	-16.72
	Chl 44	0.02	-2.55	1.10	5.74	-16.72	0

Figure 2-11 presents a schematic diagram of pigment locations and expected EET times in three neighboring CP43′ monomers out of the 18-unit ring as viewed from the PSI trimer. In this figure, for clarity, only Chl molecules corresponding to the two lowest-energy states in a CP43′ monomer (Chl 44 for state A′ and Chl 37 for state B′), and the possible Chl 41 energy transfer linker between two CP43′ monomers, are plotted. The EET rates shown in Figure 2-11 have been calculated based on the Förster mechanism using realistic spectral overlap integrals between Chl 37 and Chl 44.[51] The overlap integral dependence on the donor-acceptor ZPL gap is calculated numerically based on the actual shape of the single-site spectra with the experimentally determined phonon sideband (PSB) and local mode parameters. All parameters in these calculations are the same as in our previous CP43 study,[6] except that in order to achieve good fits of various optical spectra for the CP43′ ring, we used the slightly larger *S* value of 0.6 as discussed above. Note that one of the inter-monomer A′-B′ processes is significantly more likely than the other one, and exhibits rate comparable to the A′-A′ inter-monomer rate. The inter-monomer B′-B′ EET rate is still larger, due to both higher coupling and better spectral overlap.

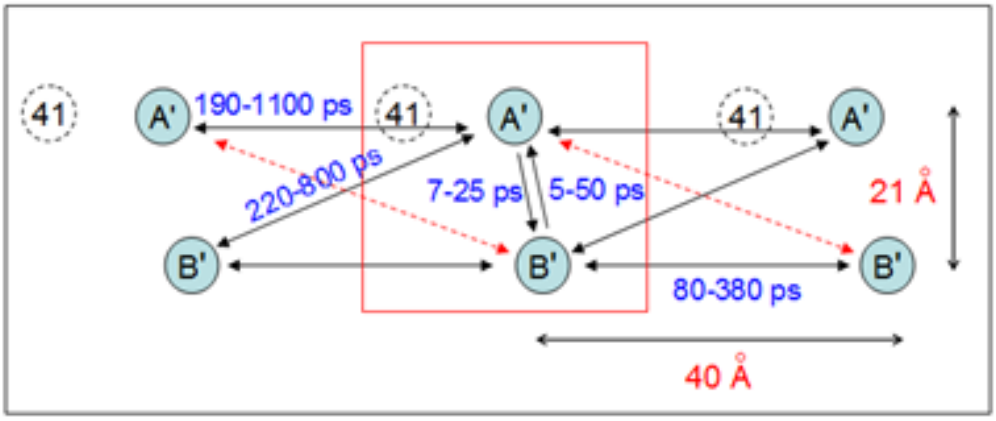

Figure 2-11 Schematic diagram of possible EET pathways within a single monomer and between monomers (*i.e.*, inter-monomer EET) viewed from inside the supercomplex in the membrane plane. Pigments A′ and B′ most likely represent Chls 44 and Chls 37, respectively, with Chls 41 acting as a possible linker in inter-monomer A′-A′ energy transfer. The red box shows the boundary of one CP43′ monomer. Some typical EET times and distances are also shown.

Most of these times (except for one of the A′-B′ processes) are short enough compared to the fluorescence lifetime of several nanoseconds, and respective EET processes are expected to reduce the hole burning and fluorescence yields of the donor pigments, according to

$$\phi_{fl}(\tau_{EET}) = \frac{\tau_{fl}^{-1}}{\tau_{fl}^{-1} + \tau_{EET}^{-1}} \quad \text{and} \quad \phi_{NPHB}(\tau_{EET}) = \frac{\Omega_0 \exp(-2\lambda)}{\Omega_0 \exp(-2\lambda) + \tau_{fl}^{-1} + \tau_{EET}^{-1}}.$$

Here, $\phi_{NPHB}(\tau_{EET})$ is the NPHB yield, $\phi_{fl}(\tau_{EET})$ is the fluorescence yield, $\Omega_0 \exp(-2\lambda)$ is the NPHB rate, τ_{fl} is the fluorescence lifetime, and τ_{EET} is the EET time.

When inter-monomer EET is taken into consideration, each of the A′ and B′ pigments can transfer to several acceptors (one in the same monomer and three in its neighboring monomers). Therefore, sub-SDF of the pigments incapable of downhill EET due to the absence of any further acceptors are shifted to the longer wavelength region, as illustrated by curves f '

and e' in Figures 2-10A and 2-10B, respectively. Note that both of these curves peak at wavelengths significantly longer than the true SDFs (*i.e.*, curves a and b), and only these bands dressed with phonons and localized chlorophyll vibrations should contribute to the emission spectra. The fit of the emission spectrum with the origin-band at 687 nm is shown in frame C of Figure 2-10. Curves 1 and 2 in frame C of Figure 2-10 are curves f ' and e' from frames A and B, respectively, dressed with delocalized protein phonons and localized Chl vibrations. Again, S = 0.6 is a realistic value based on the upper limit for S (~0.8) estimated from the maximal depths of saturated resonant holes (~42%), especially when PSI contamination partly contributes to the absorption near 685 nm (and is poorly burnable). The above contributions fit the emission spectrum reasonably well, assuming the relative contribution from band 2 (red), as discussed above, is reduced by a factor of three in comparison with the intensity of contribution from band 1 (blue). This reduction is in line with observations presented in Figure 2-5, where upon burning and blue-shifting of higher fluorescence yield A′-type pigments, the relative weight of lower fluorescence yield B′-type pigments in emission increases and overall emission decreases. Small changes of the S factor and/or shape of the phonon sideband did not significantly affect the calculated emission spectrum. Agreement between the calculated and experimental spectra, for such a complex system, is remarkably good, although small discrepancies at both high- and low-energy spectral regions still exist. First, it appears, in agreement with the spectral analysis shown in Figure 2-2, that the measured emission spectrum contains a small contribution from the broad PSI core emission, indicated by the solid arrow (PSI core emission maximum lies near 722 nm, FWHM = 22 nm[26]). On the whole, the emission spectrum can be fitted assuming 7-10% of PSI contamination, which is in agreement with our earlier conclusion that contamination of PSI is estimated to be about 8-9% of the CP43′ absorption in our isolated preparations (see Figure 2-2).

On the other hand, the small discrepancy between the calculated and experimental emission spectra on the high-energy side (dashed arrow in Figure 2-10C) could be due to emission coming from pigments with some EET channels unavailable to them, possibly due to damage beyond "normal" static disorder. As a result, their emission should be blue-shifted, in agreement with the measured emission spectra of partly damaged complexes (data not shown). Recall that previously reported fluorescence maxima of CP43′ complexes varied from 682-687 nm.[5] In the framework of the model presented here, the exact position of the fluorescence maximum will depend on the intactness of the inter-monomer EET pathways.

2.4.6. Nonresonant persistent and transient holes

The gray curves in frames A and B of Figure 2-12 show transient (see inset of Figure 2-4) and shallow persistent (curve 1 from Figure 1-4) nonresonant HB spectra of CP43′, respectively. The gray spectrum in frame B reflects the lowest-energy sub-state(s), as discussed above. Although both experimental curves are very noisy, due to extreme shallowness of the holes (*i.e.*, ~1%), the spectra can be fitted using our EET model discussed above. That is to say, the transient spectrum in frame A of Figure 2-12 can be described by the two lowest-energy states, f ' (curve 1) and e' (curve 2), dressed with phonons and localized Chl vibrations. Curve 3 is the sum of curves 1 and 2. The long-wavelength region of the persistent hole in frame B of the same figure is also in agreement with the shape of the f ' band (curve 1); the contribution from the e' band (dashed curve) cannot be assessed in this case due to interference from an anti-hole, a typical feature observed in persistent hole spectra,[35,39] although it appears that state f ' contributes more during the early stage of HB, in agreement with data shown in Figures 2-4 and 2-5.

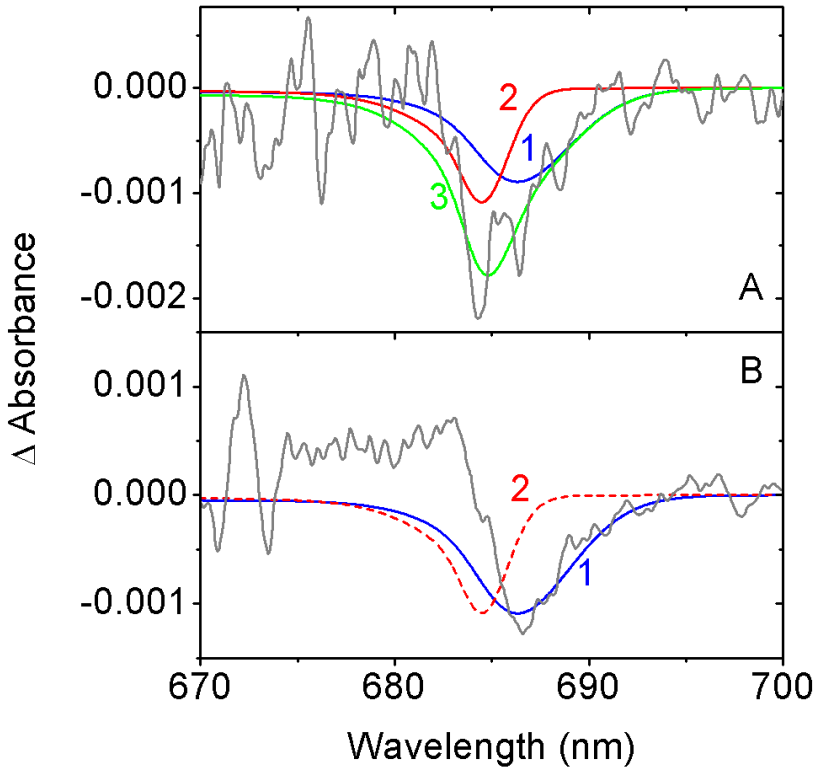

Figure 2-12 (*Frame A*) Fit of the transient hole spectrum (noisy curve) with SDFs of sub-ensembles of the two lowest-energy states, f' and e', dressed with phonons and localized Chl vibrations (curves 1 and 2, respectively). Curve 3 is the sum of curves 1 and 2. (*Frame B*) Fit of the persistent hole spectrum obtained at low fluence (noisy curve) with the SDF of the sub-ensemble of one of the two lowest-energy states, f', dressed with phonons and localized Chl vibrations (curves 1); see text for details.

2.4.7. Analysis of the ZPH action spectrum

Figure 2-13 shows the ZPH action spectrum of CP43′ with hole depths (from Figure 2-6) plotted as open circles. Recall that, if all relevant EET processes in the CP43′ ring (inter-monomer and intra-monomer) are very fast, the ZPH action spectrum would be described only by the sum (weighted by the HB yield) of bands f ' and e' from Figure 2-10. This is clearly not the case. Note, however, that curves f ' and e' discussed above are consistent with the long-wavelength region of the ZPH action spectrum. To obtain a good fit (black solid curve) to the

lower-energy side of the action spectrum, the original curve e ' needs to be multiplied by a factor of three (see red solid curve). Apparently, as in the case of the CP43 complex,[6] the HB yield of the B′ band in CP43′ is about three times higher than in the A′ band.

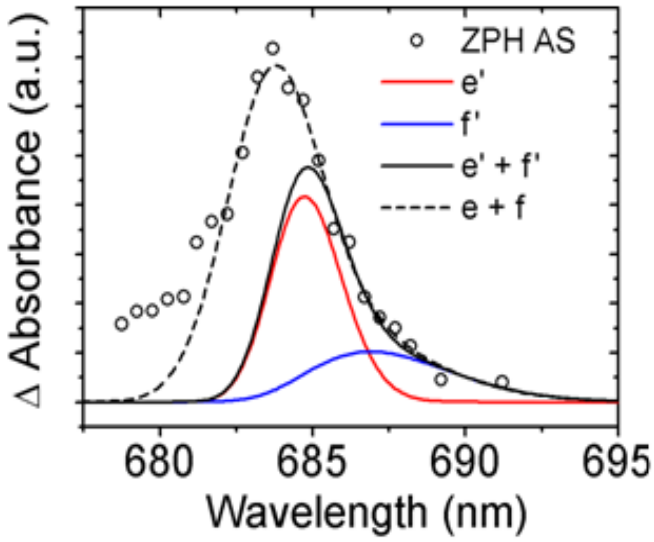

Figure 2-13 Fit of the high-dose ZPH action spectrum (open circles) of CP43′ with sub-ensemble SDFs of the two lowest-energy states (A' and B') without inter-monomer EET (curves f and e) and with inter-monomer EET (curve f ' and e').

The discrepancy between the solid black curve and the high-energy region of the action spectrum implies that inter-monomer EET is relatively slow, in agreement with data in Figure 2-11. That is, for long EET times (*e.g.*, hundreds of ps; see Figure 2-11) pigments described by (e minus e') and (f minus f ') may also experience SHB, though at a slower rate than fractions of pigments described by bands f ' and e', truly incapable of the downhill EET. The dashed line represents the theoretical ZPH action spectrum when contributions (e' minus e) and (f ' minus f) are taken into account. This argument becomes even more convincing, if one notes that the HB action spectrum was measured with 2.4 J/cm^2 and at 0.5 cm^{-1} resolution. Thus, the holes were in fact much deeper than the apparent 10%, and the (e minus e′) and (f minus f ′) fractions were clearly probed

alongside e′ and f ′ fractions. One cannot also exclude that, since the action spectrum was measured from lower to higher energies, some anti-hole absorption (exhibiting high HB/recovery yields) was added at 680-684 nm while burning was performed at longer wavelengths.

2.4.8. Structural implications

As shown in Ref. [9], the PSI-CP43′ supercomplex contains 18 CP43′ monomers in a ring around the PSI trimer. However, *in vivo* the ring is not perfect due to distortions arising from the PSI trimer exhibiting C_3 symmetry. In each PSI monomer, there are three regions where PSI Chls are situated within 20-25 Å of the Chls in CP43′ monomers, as shown by the three blue-dashed ovals in Figure 2-8. Only these molecules are likely energy acceptors that can receive excitation energy from the CP43′ antenna ring and then transfer it to the reaction center of the PSI. Similarly, not all CP43′ monomers have the same likelihood of transferring energy directly to the PSI because of their nonequivalent positions relative to the PSI energy acceptors. Therefore, in addition to the lowest-energy states in each single CP43′ monomer, one should consider the lowest-energy states that constitute minima among several neighboring CP43′ monomers. It appears that pigments responsible for such global lowest-energy states should be relatively close to the above-mentioned PSI acceptors, as this would ensure the most effective excitation energy transfer. One could speculate that C_3-type distortion to the CP43′ ring can cause compression of monomers in certain positions within the ring, with associated additional red shift of the lowest-energy pigments. (This selective compression of course will not occur in the isolated CP43′ ring.) This mechanism could focus excitation energy towards the desired regions of the PSI core.

2.5. Conclusions

From a comparative study of various absorption spectra of PSI-CP43′, CP43′, and PSI complexes, we conclude that, in samples studied in this work, there are about 13 Chls in each of the 18 CP43′ monomers in the PSI-CP43′ supercomplex. The latter is in perfect agreement with the number of pigments observed in CP43 of PSII.[32,34] By analyzing the absorption, emission, persistent/transient HB spectra, as well as the ZPH action spectrum of CP43′ using the modified uncorrelated EET model,[6,35] we suggest, by analogy with the CP43 complex, that there appear to be two nearly degenerate lowest-energy states (with a dominant contribution from pigments A′ and B′) in each monomer. That is, the above states are mostly localized on single pigments. The states, A′ and B′, have site distribution functions peaking at 684.0 nm (FWHM of 180 cm^{-1}) and 683.0 nm (FWHM of 80 cm^{-1}), respectively. We argue that within each monomer, EET between these two quasi-degenerate states occurs. From the fit of the red-shifted emission spectrum, it is clear that EET must also take place among the CP43′ monomers. This is in good agreement with descriptions of nonresonant transient and persistent holes, as discussed above. Both analysis of the HB action spectrum and direct calculation of inter-monomer transfer times indicate that the latter are relatively long. For optimal energy transfer in the PSI-CP43′ supercomplex, it would be useful if the CP43′ monomers possessing the lowest-energy pigments among the neighboring subunits were aligned with the regions of the PSI cores having spatially and energetically optimized pigments. These monomers could then efficiently transfer excitation energy, funneled from other CP43′ monomers, to the PSI core. Finally, assuming that CP43 and CP43′ monomers have similar structures, which is consistent with high amino acid homology between the two proteins, our data support the structural model (regarding the orientation of CP43′ complexes within the ring surrounding the PSI core) proposed by Nield *et al.*[9] This view is in agreement

with our previous modeling studies[6] and excitonic calculations for the CP43 complex of PSII, where we argued that most likely pigments contributing to the lowest A and B states are Chl 44 and Chl 37, respectively. Combination of CP43′ relative orientation according to Nield *et al.* [9] with the above assignment of the two lowest-energy pigments of CP43′ could facilitate very efficient energy transfer from the antenna CP43′ complexes to the PSI reaction center.

Acknowledgement

This work was supported by the NSF ARRA Grant (CHE-0907958). V.Z. acknowledges support by NSERC, R.P. by MICINN (Grant AGL2008-00377) in Spain, and M.S. by the US Department of Energy's Photosynthetic Systems Program within the Chemical Sciences, Geoscience, and Biosciences Division of the Office of Basic Energy Sciences under NREL Contract #DE-AC36-08-GO28308. Partial support for K.A. was provided by the U.S. Department of Energy (DOE) EPSCoR Grant (DE-FG02-08ER46504). We also acknowledge helpful discussions with Mike Reppert (Department of Chemistry, MIT) and TEM studies conducted by Bryan Donohue (NREL).

References

(1) Stewart, I.; Falconer, I. R. In *Oceans and human health: risks and remedies from the seas*; Wash, P. J., Smith, S. L., Fleming, L. E., Eds.; Academic Press, 2008; pp 271-296.

(2) Grossman, A. R.; Schaefer, M. R.; Chiang, G. G.; Gollier, J. L. In *The Molecular Biology of Cyanobacteria*; Bryant, D. A., Ed.; Kluwer Academic Publishers, Dordrecht, 1994; pp 487-517.

(3) Bibby, T. S.; Nield, J.; Barber, J. *Nature* **2001**, 412, 743-745.

(4) Melkozernov, A. N.; Bibby, T. S.; Lin, S.; Barber, J.; Blankenship, R. E. *Biochem*. **2003**, 42, 3893-3903.

(5) Andrizhiyevskaya, E. G.; Schwabe, T. M. E.; Germano, M.; D'Haene, S.; Kruip, J.; van Grondelle, R.; Dekker, J. P. *Biochim. Biophys. Acta* **2002**, 1556, 265-272.

(6) Dang, N. C.; Zazubovich, V.; Reppert, M.; Neupane, B.; Picorel, R.; Seibert, M.; Jankowiak, R. *J. Phys. Chem. B* **2008**, 112, 9921-9933.

(7) Bibby, T. S.; Nield, J.; Barber, J. *J. Biol. Chem*. **2001**, 276, 43246-43252.

(8) Boekema, E. J.; Hifney, A.; Yakushevska, A. E.; Piotrowski, M.; Keegstra, W.; Berry, S.; Michel, K. P.; Pistorius, E. K.; Kruip, J. *Nature* **2001**, 412, 743-745.

(9) Nield, J.; Morris, E. P.; Bibby, T. S.; Barber, *J. Biochem*. **2003**, 42, 3180-3188.

(10) Zhang, Y.; Chen, M.; Church, W. B.; Lau, K. W.; Larkum, A. W. D.; Jermiin, L. S. *Biochim. Biophys. Acta* **2010**, 1797, 457-465.

(11) Sandström, S.; Ivanov, A. G.; Park, Y. -Y.; Öquist, G.; Gustafsson, P. *Physiol. Plant*. **2002**, 116, 255-263.

(12) Kouřil, R.; Yeremenko, N.; D'Haene, S.; Yakushevska, A. E.; Keegstra, W.; Matthijs, H. C. P.; Dekker, J. P.; Boekema, E. J. *Biochim. Biophys. Acta* **2003**, 1607, 1-4.

(13) Andrizhiyevskaya, E. G.; Frolov, D.; van Grondelle, R.; Dekker, J. P. *Biochim. Biophys. Acta* **2004**, 1656, 104-113.

(14) Aspinwall, C. L.; Duncan, J.; Bibby, T.; Mullineaux, C. W.; Barber, J. *FEBS Lett*. **2004**, 574, 126-130.

(15) Michel, K. -P.; Pistorius, E. K. *Physiol. Plant*. **2004**, 120, 36-50.

(16) Sarcina, M.; Mullineaux, C. W. *J. Biol. Chem*. **2004**, 279, 36514-36518.

(17) Dekker, J. P.; Boekema, E. J. *Biochim. Biophys. Acta* **2005,** 1706, 12-39.

(18) Ihalainen, J. A.; D'Haene, S.; Yeremenko, N.; van Roon, H.; Arteni, A. A.; Boekema, E. J.; van Grondelle, R.; Matthijs, H. C. P.; Dekker, J. P. *BioChem*. **2005**, 44, 10846-10853.

(19) Kouřil, R.; ; Arteni, A. A.; Lax, J.; Yeremenko, N.; D'Haene, S.; Rögner, M.; Matthijs, H. C. P.; Dekker, J. P.; Boekema, E. J. *FEBS Lett*. **2005**, 579, 3253-3257.

(20) Elli, A. F.; Jelezko, F.; Tietz, C.; Studier, H.; Brecht, M.; Bittl, R.; Wrachtrup, *J. Biochem*. **2006**, 45, 1454-1458.

(21) Ivanov, A. G.; Krol, M.; Sveshnikov, D.; Selstam, E.; Sandström, S.; Koochek, M.; Park, Y. -I.; Vasil'ev, S.; Bruce, D.; Öquist, G.; Huner, N. P. A. *Plant Physiol*. **2006**, 141, 1436-1445.

(22) Murray, J. W.; Duncan, J.; Barber, J. *Trands Plant Sci*. **2006**, 11, 1360-1385.

(23) Singh, A. K.; Sherman, L. A. *Photosynth. Res.* **2007**, 93, 17-25.

(24) van der Weij-de Wit, C. D.; Ihalainen, J. A.; van de Vijver, E.; D'Haene, S.; Matthijs, H. C. P.; van Grondelle, R.; Dekker, J. P. *Biochim. Biophys. Acta* **2007**, 1767, 1393-1400.

(25) Stork, T.; Michel, K. -P.; Pistorius, E. K.; Dietz, K. –J. *J. Exp. Bot*. **2005**, 56, 3193-3206.

(26) Yeremenko, N.; Kouřil, R.; Ihalainen, J. A.; D'Haene, S.; van Oosterwijk, N.; Andrizhiyevskaya, E. G.; Keegstra, W.; Dekker, H. L.; Hagemann, M.; Boekema, E. J.; Matthijs, H. C. P.; Dekker, J. P. *Biochem*. **2004**, 43, 10308-10313.

(27) Chen, M.; Bibby, T. S. *Photosynth. Res*. **2005**, 86, 165-173.

(28) Riley, K. J.; Zazubovich, V.; Jankowiak, R. *J. Phys. Chem. B* **2006**, 110, 22436-22446.

(29) Berera, R.; van Stokkum, I. H. M.; D'Haene, S.; Kennis, J. T. M.; van Grondelle, R.; Dekker, J. P. *Biophys. J.* **2009**, 96, 2261-2267.

(30) Zouni, A.; Witt, H. -T.; Kern, J.; Fromme, P.; Kraub , N.; Saenger, W.; Orth, P. *Nature* **2001**, 409, 739-743.

(31) Ferreira, K. N.; Maghlaoui, T. M.; Barber, J.; Iwata, S. *Science* **2004**, 303, 1831-1838.

(32) Loll, B.; Kern, J.; Saenger, W.; Zouni, A.; Biesiadka, J. *Nature* (London, U. K.) **2005**, 438, 1040-1044.

(33) Guskov, A.; Kern, J.; Gabdulkhakov, A.; Broser, M.; Zouni, A.; Saenger,W. *Nat. Struct. Mol.Biol.* **2009**, *16*, 334-342.

(34) Umena, Y.; Kawakami, K.; Shen, J. –R.; Kamiya, N. *Nature* **2011**, 473, 55-60.

(35) Zazubovich, V.; Jankowiak, R. *J. Lumin*. **2007**, 127, 245-250.

(36) Jeanjean, R.; Zuther, E.; Yeremenko, N.; Havaux, M.; Matthijs, H. C. P.; Hagemann, M. *FEBS Lett.* **2003**, *549*, 52–56.

(37) Porra, R. J.; Thompson, W. A.; Kriedemann, P. E. *Biochim. Biophys. Acta* **1989**, *975*, 384-394.

(38) Groot, M.; Frese, R. N.; de Weerd, F. L.; Bromek, K.; Pettersson, Å.; Peterman, E. J. G.; van Stokkum, I. H. M.; van Grondelle, R.; Dekker, J. P. *Biophys. J.* **1999**, *77*, 3328.

(39) Jankowiak, R.; Zazubovich, V.; Rätsep, M.; Matsuzaki, S.; Alfonso, M.; Picorel, R.; Seibert, M.; Small, G. J. *J. Phys. Chem. B* **2000**, *104*, 11805–11815.

(40) Hughes, J. L.; Picorel, R.; Seibert, M.; Krausz, E. *Biochem.* **2006**, *45*, 12345–12357.

(41) Neupane, B.; Dang, N. C.; Acharya, K.; Reppert, M.; Zazubovich, V.; Picorel, R.; Seibert, M.; Jankowiak, R. *J. Am. Chem. Soc.* **2010**, *132*, 4214–4229.

(42) Reddy, N. R. S.; Picorel, R.; Small, G. J. *J Phys. Chem.* **1992**, *96*, 6458–6464.

(43) Jordan, P.; Fromme, P.; Witt, H. T.; Klukas, O.; Seanger, W.; Kruss, N. *Nature (London, U. K.)* **2001**, *411*, 909–917.

(44) Zhang, L.; McSpadden, B.; Pakrasi, H. B.; Whitmarsh, J. *J. Biol. Chem.* **1992**, *267*, 19054–19059.

(45) La Roche, J.; Boyd, P. W.; McKay, R. M. L, Gelder, R. J., *Nature* **1996**, *382*, 802–805.

(46) Di Donato, M; van Grondell, R; van Stokkum, I. H.; Groot, M. L., *J. Phys. Chem. B* **2007**, *111*, 7345–7352.

(47) de Weerd, F. L.; van Stokkum, I. H. M.; van Amerongen, H.; Dekker, J. P.; van Grondelle, R. *Biophys. J.* **2002**, *82*, 1586–1597.

(48) Reppert, M.; Zazubovich, V.; Dang, N. C.; Seibert, M.; Jankowiak, R. *J. Phys. Chem. B* **2008**, 112, 9934-9947.

(49) Müh, F.; Renger, T.; Zouni, A. *Plant Physiol. Biochem. (Issy les Moulineaux, Fr.)* **2008**, *46*, 238–264.

(51) Rätsep, M.; Pieper, J.; Irrgang, K. -D.; Freiberg, A. *J. Phys. Chem. B* **2008**, *112*, 110–118.

(52) Herascu, N.; Najafi, M.; Amunts, A.; Pieper, J.; Irrgang, K. -D.; Picorel, R.; Seibert, M.; Zazubovich, V. *J. Phys. Chem. B* **2011**, *115*, 2737–2747.

Chapter 3 - Electron Transfer in *Rhodobacter sphaeroides* Reaction Centers Containing Zn-Bacteriochlorophylls: a Hole-Burning Study

(Paper prepared for submission to J. Phys. Chem. B. 2011)

Bhanu Neupane, Paul Jaschke, Rafael Saer, J. Thomas Beatty, Mike Reppert and Ryszard Jankowiak

Abstract

Nonresonant and resonant transient, photochemical hole-burned (HB) spectra are presented for primary electron donor states of a novel bacterial reaction center (Zn-RC) of *Rhodobacter sphaeroides*, containing six Zn-bacteriochlorophylls (Zn-BChls). A "Zn-β-RC" in which the Zn-BChl in the bacteriopheophytin (BPhe)-binding site on the A side (H_A) has the Zn *penta*-coordinated, was also studied. The fifth ligand comes from a histidine introduced by site-directed mutagenesis. Formation of the $P^+Q_A^-$ state was observed in both types of RC, although under identical experimental conditions a significantly deeper P_- band (corresponding to the lower-energy, special pair, excitonic component) was revealed in the Zn-RC. Assuming a similar lifetime of the $P^+Q_A^-$ state, the quantum yield of $P^+Q_A^-$ formation decreased by ~60% in the Zn-β-RC (compared to the Zn-RC), as was seen in a comparison of analogous (Mg) BChl-containing wild type and β-RCs of *Rb. sphaeroides* [Ch. Kirmaier et al. *Science*, **251** (1991) 922]. However, the average (weakly frequency-dependent) low-temperature electron transfer (ET) rates of the Zn-RC and Zn-β-RC (measured from ZPHs in resonant transient HB spectra)

were both ~1 ps, and similar to a rate previously measured in the *Rb. sphaeroides* native RC [S.G. Johnson et al., *J. Phys. Chem*. 93 (1989) 5953]. Electron transfer rates observed in this work on the Zn-RC yielded a P870* decay rate in good agreement with recent room-temperature, time-domain data [S. Lin et al. PNAS **106** (2009) 8537]. A lack of correlation observed between the holes near 810 nm and 883 nm, accounting for electrochromically induced shifts of the Zn-BChl transitions in the $B_{A,B}$ and $H_{A,B}$ binding sites, produced by formation of $P^{+}BHQ_{A}^{-}$ state, indicates that the 810 nm bleach does not correspond to the P_{+} (upper excitonic component of the dimer) band, and is mostly contributed to by a shift of the B_B absorption band. ZPH-action spectra indicated inhomogeneous broadening (Γ_{inh}) of ~110 cm^{-1} (Zn-RC) and ~120 cm^{-1} (Zn-β-RC). Experimentally determined Γ_{inh} decreased the number of variables in theoretical fits of the absorption and frequency-dependent shapes of resonant HB spectra, leading to more reliable Huang-Rays factors for both low-frequency phonons and a pseudolocalized phonon, ω_{SP}, often referred to as the special pair marker mode.

3.1. Introduction

The purple non-sulfur bacterium *Rhodobacter (Rb.) sphaeroides* is an extremely useful system for studying photosynthetic electron transfer (ET). The core of the relatively simple photosynthetic apparatus in this bacterium is a dimer of a reaction center (RC) complex surrounded by the light-harvesting 1 complex (LH1) and the PufX protein.[1,2,3] The bacterial RC (BRC) contains three proteins called H, M and L; the structurally similar RC M and L proteins consist of five transmembrane helices with pseudo two-fold symmetry, whereas the RC H protein has only one transmembrane helix and a large cytoplasmic domain.[4] The type 2 RC of *Rb. sphaeroides* contains a 'special pair' bacteriochlorophyll (BChl) dimer (sometimes called 'P') bound by RC M and L proteins on the periplasmic side of the membrane. The special pair is flanked by two accessory BChls bound to RC L (in the B_A site) and RC M (in the B_B site), which are the periplasmic ends of two cofactor branches called A and B (see Figure 3-1 frame A). Two bacteriopheophytin *a* (BPhe) molecules (in the H_A and H_B sites) are located between the accessory BChls and two quinones (Q_A and Q_B), which are bound near the cytoplasmic side of the RC. An iron (Fe^{2+}) atom is located between Q_A and Q_B, and a carotenoid is bound near the special pair on the B-branch side.[5] Electrons are transferred through the A-branch pigments, from the special pair through the monomeric BChl in the B_A position[6] and then to the BPhe in the H_A-site, before passing on to the Q_A and finally the Q_B quinone.[7]

The relative redox energies of the different pigments of the *Rb. sphaeroides* RC are among the best understood of any photosynthetic complex, due to their simplicity and ease of spectroscopic measurement.[8,9,10,11] The redox midpoint potentials of each step in the A-branch

result in a series of energetically favorable downhill reactions, and the times for electron transfer (ET) from P* → H_A → Q_A → Q_B at room temperature are 3 ps, 200 ps and 200 μs, respectively. [12] These times reflect the magnitude differences in redox potential of the pigments involved, because this trait is the fundamental driving force of the reaction, although recent work has suggested that protein dynamics also play a significant role in the overall kinetics of the reaction.[13]

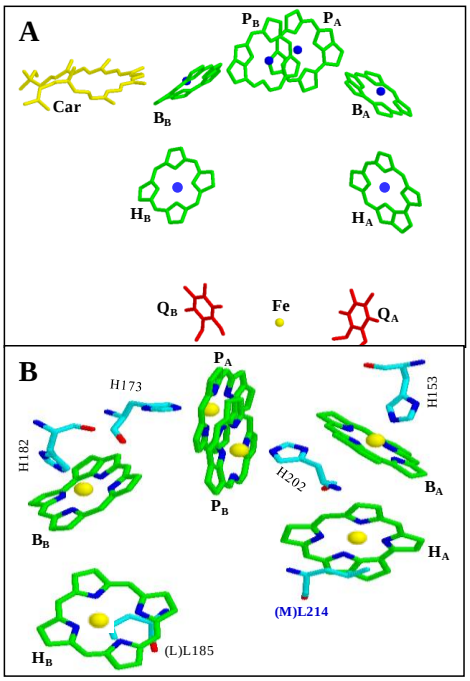

Figure 3-1 Cofactor probable arrangement in the Zn-RC, based on 2.0 Å crystal structure of the WT-RC from *Rb. sphaeroides*, PDB ID 3I4D. *Frame A.* Cofactors are shown in different colors: carotenoid (yellow), Zn-BChls (green; Zn atoms shown as blue sphere), and ubiquinones in red. *Frame B.* Close-up view of Zn-BChls. Atoms are color coded: carbon green, nitrogen blue, and magnesium yellow. Histidines that ligate the BChl Mg^{2+} in the WT-RC are also shown with atoms in different colors: nitrogen blue, oxygen red, and carbon cyan. For clarity, alkyl tail of ubiquinones and Zn-Bchls and all other side chains of Zn-BChls are truncated.

Recently, it was discovered that a mutant of *Rb. sphaeroides* contains a modified BChl biosynthetic pathway that causes it to produces a different type of BChl, where the central Mg^{2+} has been replaced by Zn^{2+} (Zn-BChl), as well as ceasing production of BPhe.[14,15] In this mutant, Zn-BChl is assembled into the RC and LH1 complexes in place of the normal (Mg-)BChl and BPhe.[14,16] More detailed investigation of the so-called Zn-RC, using low-temperature spectroscopy, indicated that it contains 6 Zn-BChl in the P-, $B_{A,B}$- and $H_{A,B}$-sites in place of the four BChls and two BPhes.[16] The change in the cofactor in the H_A-site from a BPhe in the wild type RC (WT-RC) to a Zn-BChl in the Zn-RC, mimics a site-directed mutant of the RC, called the β-mutant RC, that caused a BChl to take the place of BPhe in the H_A-site.[12] This β-mutant RC caused a reduction in ET efficiency from P to H_A to ~50% of the WT-RC, thought to be caused by a converging of the redox-potentials of the B_A and H_A cofactors, due to the change in the H_A cofactor from BPhe to BChl. Therefore it was surprising that the ET reactions of the Zn-RC were found to be nearly identical to those of the WT-RC, despite the Zn-RC cofactor arrangement (with a Zn-BChl in the H_A-site), more closely resembling the β-mutant RC than the WT-RC.[16]

The preservation of efficient ET in the Zn-RC was ascribed to the coordination state of the Zn-BChl bound to the H_A-site. In the WT-RC and Zn-RC P- and $B_{A,B}$-sites, Mg- and Zn-BChl are both penta-coordinated: four ligands come from the BChl molecule itself and the fifth from the RC protein which provides a His residue in an axial position to the central metal[4,17]; see Figure 3-1 frame B. In the WT-RC the H_A-site binds BPhe, which does not contain a metal ion, and possesses a more positive redox potential than B_A-BChl. It was suggested that in the Zn-RC,

the Zn-BChl bound to the H_A-site is not penta- but tetra-coordinated, because a fifth coordinating ligand (His residue) is absent in the H_A-site. Thus, it was thought that the tetra-coordinated Zn-BChl would have a more positive redox potential and would be more similar to BPhe than to a pentacoordinated Zn-BChl in the B_A-site. This difference in coordination state between the cofactors in the B_A and H_A sites of the Zn-RC was proposed to result in a downhill energy landscape enabling efficient ET, and avoiding the deficiency observed in the β-mutant RC where in both B_A- and H_A-sites the BChls are penta-coordinated.

To test the hypothesis that the coordination state of the H_A-cofactor tunes the Zn-RC ET rate and efficiency, we modified one amino acid at position 214 of the M protein (M214) in the RC H_A-site so that a His was present in place of the usual Leu; see Figure 1B. This change is the same as in the original β-mutant RC, producing what we call the Zn-β-RC. It was expected that a His residue at this position would provide a fifth ligand to the Zn^{2+} of Zn-BChl in the H_A-site, and make it penta- instead of tetra-coordinated. By analogy with the original β-mutant RC, the predicted effect of this change would be a two-fold reduction to the ET time compared to the unmodified Zn-RC.[12]

In contrast to the above prediction, using spectral hole burning (HB)[10,11,18], we demonstrate that both the Zn-RC and Zn-β-RC have surprisingly similar P870* decay times. However, the quantum yield of charge separation in Zn-β-RC decreases by 60% in comparison to Zn-RC. We argue that decrease in the quantum yield is related to the difference in coordination state of the Zn-BChl in the H_A-site of the RC, as suggested in previous work.[16] Using high resolution photochemical HB spectra we show, for the first time, that P870

heterogeneity can be measured experimentally. From the simultaneous fit of photochemical (resonant and nonresonant) HB and absorption spectra of P870 we find that electron-phonon coupling parameters in Zn-β-RC and Zn-RC are slightly different. In contrast to earlier simulations[19,20,21,22], we used experimentally determined heterogeneity to fit various optical spectra, providing more reliable electron-phonon coupling parameters. The possible origin(s) of a shoulder observed on the low energy side of the B Q_y-band, near 820 nm in low temperature absorption and HB spectra of the *Rb. sphaeroides* RC, which is often assigned in the literature to P_+[21,22] (*i.e.*, the upper excitonic component of the homodimer special pair) is also discussed.

3.2. Materials and methods

3.2.1. Bacterial strains, plasmids, growth of cultures

Rb. sphaeroides strains were grown as described previously[23] at 30°C in LB medium. Antibiotics were used in *Rb. sphaeroides* cultures at the following working concentrations: spectinomycin 50 μg/mL, tetracycline 2 μg/mL.

3.2.2. RC isolation

Cell lysis and membrane isolation were performed as described previously.[23] Briefly, a *Rb. sphaeroides* culture was pelleted at 3000 RCF at 4°C for 15 minutes. The supernatant was removed and cell pellet was re-suspended in 10 mM Tris-HCl (pH 8.0). Cells were disrupted in a modified French press[23], and membranes isolated by ultracentrifugation at 355,040 RCF for 20 min. Membrane pellets were re-suspended in the same buffer as above. Large scale isolation of RCs from purified membranes was performed as described previously.[24]

3.2.3. Construction of ΔRCLH/ΔBchD strain

Chromosomal DNA from wild type *Rb. sphaeroides* strain NCIB8253 was purified from cells and used as a template for PCR amplification of the *bchD* gene using primers *bchD* forward (5'-AAGACGCCGAACACCGTGCTG-3') and reverse (5'-GCCTGCCCCAGAAGGAGCTC-3') and the following parameters: Platinum Pfx polymerase (Invitrogen) with 7% dimethylsulfoxide and initial denaturation of 94°C for 5 min, followed by 10 cycles of 94°C for 15 sec, 72° to 67°C (-0.5°C per cycle) touchdown for 30 sec, 72°C for 1 min 29 sec, followed by 20 cycles of 94°C for 15 sec, 63°C for 30 sec, 72°C for 1 min 29 sec, then 7 min at 72°C. The PCR product was a 1485 bp section of chromosome 1 that corresponds to the coordinates 1,998,332 to 1,999,721 of NCBI Reference Sequence NC_007493.1. This section encompasses a 254 bp region of the 3' end of the *bchI* gene, starting 72 bp upstream of a native *SacI* site, and runs 1231 bp into the 5' end of the *bchD* gene. This region also includes a native *NruI* site at coordinate 1,999,093. The reverse primer that binds within the *bchD* gene was engineered to introduce a *SacI* site through a single mismatch.

The PCR product was cut with *SacI* and ligated into pUC19. The resulting construct was called pUC19(*bchD*). A 2.0 kb *SmaI* fragment containing the Ω cartridge (which encodes spectinomycin-resistance) was cut out of the plasmid pHP45Ω and gel purified. The pUC19(*bchD*) plasmid was cut with *NruI* and the *SmaI* Ω fragment was blunt ligated into the blunt cut *NruI* site. The resulting construct was called pUC19(*bchD*Ω). Plasmid pUC19(*bchD*Ω) was digested with *SacI* and the *bchD*Ω insert was gel purified. The *bchD*Ω *SacI* fragment was ligated into pNHG1. The resulting plasmid was called pNHG1(*bchD*Ω) and was conjugated into

Rb. sphaeroides strain ΔRCLH.[23] Selection for single-crossovers of pNHG1(bchDΩ) into the chromosome was followed by aerobic growth on spectinomycin-supplemented RCV liquid medium for 5-7 days and then by plating on RCV agar supplemented with spectinomycin and 15% sucrose to counterselect for loss of the pNHG1 plasmid from the chromosome. The confirmed exconjugant was called ΔRCLH/ΔBchD and had a RC^- $LH1^+$ $LH2^-$ $BchD^-$ phenotype, confirmed by absorption spectroscopy of isolated membranes and absorption spectra of acetone/methanol extractions. Finally, the plasmid was conjugated into the ΔRCLH/ΔBchD strain to yield the ΔRCLH/ΔBchD strain with the phenotype of $RC^+LH1^+LH2^-$ $BchD^-$, confirmed as described above.

3.2.4. Spectroscopic measurements

A detailed description of our HB setup can be found in[25,26]. Briefly, low-temperature absorption and HB spectra were recorded with a Bruker HR125 Fourier transform spectrometer at a resolution of either 4 cm^{-1} or 1 cm^{-1}. Nonresonant HB was performed with the green 496.5 nm line from a Coherent Innova 200 Ar^+ ion laser. A tunable (890-905 nm range) Coherent CR899 Ti-Sapphire laser (line width of 0.07 cm^{-1}), pumped by 532 nm Spectra-Physics (Millenia 10s) diode laser, was used for resonant photochemical HB. The intensity of the CR899 laser beam was stabilized electro-optically (Brockton Electro-Optics Corp., LPC) and was attenuated (if needed) using a set of neutral density filters. The sample temperature was maintained at 5 K using a Janis 8-DT Super Vari-Temp liquid helium cryostat. The temperature was stabilized and measured with a Lakeshore Cryotronic model 330 temperature controller. For absorption measurement, samples suspended in buffer solution (containing 10 mM Tris-HCl, 1 mM EDTA ,

pH 8.0, and 0.025 % LDAO detergent) were mixed with 70% glycerol (v/v) to make transparent glass when frozen. The optical density of the sample around 800 nm at 5 K was ~1. The photochemical (transient) HB spectra are obtained by taking difference of absorption spectra measured with burning laser on and off after the nonphotochemical hole burning (NPHB) is complete. However, in the case of BRCs persistent NPHB is negligibly small.

3.3. Results

3.3.1. Low temperature absorption spectra

Low temperature absorption spectra of Zn-RC (red curve a) and Zn-β-RC (blue curve b) Q_y region are shown in Figure 3-2 frame A. Spectra a and b are normalized to the same intensity of the P Q_y-band (Q_y transition of $P_{A,B}$ Zn-BChls). The peak of $P_{A,B}$ Q_y-band at T = 5 K appears near 884 nm, but to be consistent with literature[11,19,20,22] data we refer to this band as P870. In comparison to the Zn-RC, the B Q_y (Q_y transitions of the $B_{A,B}$ Zn-BChls, near 794 nm) and H Q_y (Q_y transitions of $H_{A,B}$ Zn-BChls, near 772 nm) bands in Zn-β-RC are blue-shifted by ~55 and ~80 cm^{-1}, respectively. Also note the increase in intensity of the H band and decrease in the B band in the Zn-β-RC. The P870 band of the Zn-β-RC shows a slight broadening. The red-shifted P870 band in both Zn-RC and Zn-β-RC compared to B and H bands is caused by electron-exchange (short range) effects.[27] As was reported for the original β-mutant RC[16] the absorption spectrum of the Zn-β-RC shows a distinct shoulder (Figure 3-2, see red solid arrow in frame A) near 810 nm. The possible origin of this shoulder will be discussed in section 4.1, but at this point we hasten to add that the intensity of this shoulder even in the WT-RC (which appears near 820 nm at 5 K), varies from sample to sample[16,20,21,28,29] and is almost absent in the R-26[21,30,31]

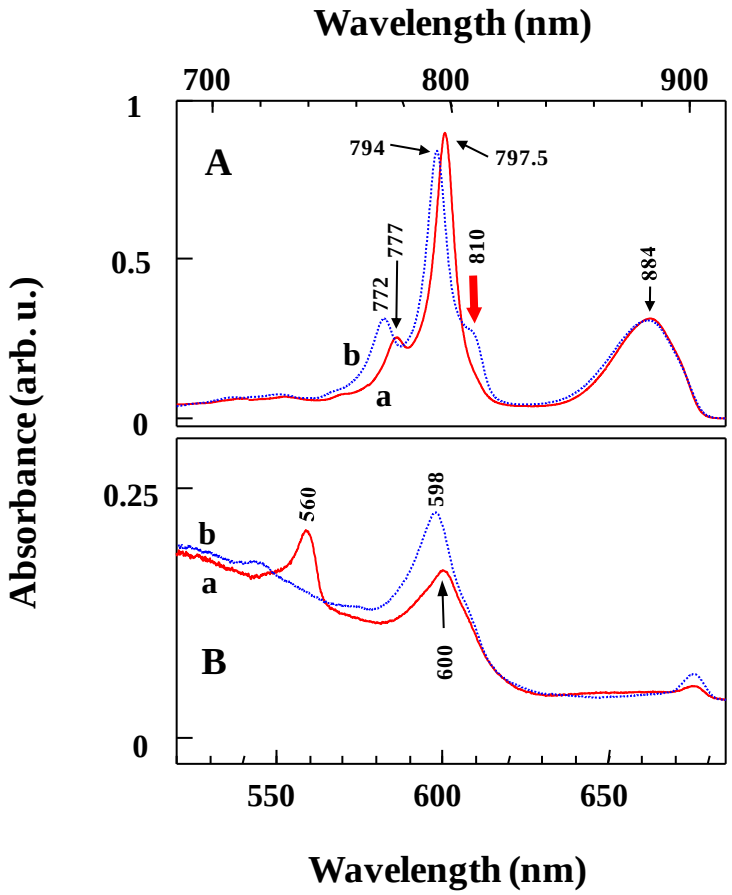

Figure 3-2 Absorption spectra of RCs at 5 K. The Q_y and the Q_x- regions are shown in frames A and B, respectively. Curves a are of the Zn-RC and curves b the Zn-β-RC. Spectra are normalized at the maximum of P870 band.

mutant RC (i.e., the RC of the carotenoid-less mutant of Rb. sphaeroides), suggesting that in some samples Car can be lost during isolation/purification procedures. In comparison to the P870 band of the WT-RC[16,21,28] the P870 band of the Zn-RC (at 5 K) is blue-shifted by ~150 cm^{-1}. This shift is caused by the different light-absorption properties of Zn-BChl and (Mg-) BChl.

The Q_x spectral region of two RCs also shows some differences, as illustrated in Figure 3-2 frame B. As suggested in[16] the Q_x-transitions of the Zn-RC $B_{A,B}$ and $P_{A,B}$ Zn-BChls, which

are believed to be penta-coordinated, lie near 600 nm. However the band at ~560 nm, which in the Zn-RC arises from the Q_x-transition of tetra-coordinated Zn-BChls in $H_{A,B}$ sites[16], completely disappears from the Zn-β-RC absorption spectrum, while the intensity near 600 nm (on the high-energy, blue side) increases. Interestingly, the above mentioned decrease and increase nearly cancel, suggesting that changes occurred at both the H_A and the H_B site (*vide infra*). Because the Zn-β-RC was thought to have single H_A site point mutation, this behaviour is unexpected as the absorption spectra are what would be expected if the Zn atoms of both the $H_{A,B}$ cofactors in Zn-β-RC were penta-coordinated. However, this mutant had an unexpected 2nd site mutation of L86 Q to H. To confirm that this minor mutation (i.e. L86 Q to H) is not associated with the complete disappearance of the $H_{A,B}$ Q_x band mentioned above, another Zn-β-RC (with only the M214L to H mutation) was prepared and studied. We hasten to add that DNA sequencing, performed on both the Zn-RC and Zn-β-RC genes, confirmed that M214 was converted to H. However, optical spectra of both Zn-β-RC samples were nearly indistinguishable, proving that the 2nd site mutation (L86 Q to H) did not affect optical spectra of the RC cofactors (data not shown).

3.3.2. Non-resonant photochemical HB (PHB) spectra

The main frame in Figure 3-3 shows Q_y absorption spectra of the Zn-RC measured without (curve a) and with (curve b) burn laser on after the nonphotochemical HB (hole depth less than 1 %) is complete. The difference spectrum (b-a) shown as curve c corresponds to the transient photochemical HB (PHB) spectrum. The spectra a, b, and c in the lower and upper insets show Q_x and vibronic spectral regions, respectively. The spectral changes observed in spectrum b

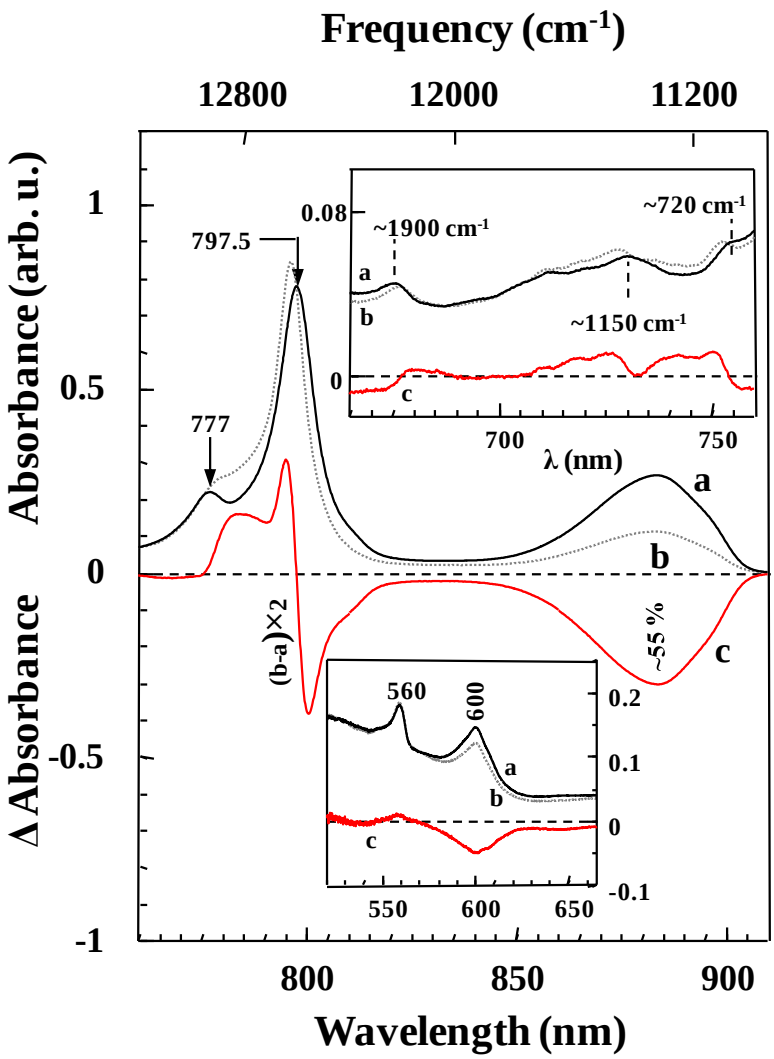

Figure 3-3 Curves a and b in the main frame and both insets correspond to preburn absorption spectrum of Zn-RC and absorption spectrum measured with burn laser on, respectively. For clarity, the Q_x- and vibronic-regions are shown separately in the lower and upper insets. Curves c (multiplied by a factor of two) are transient PHB spectra obtained with the burn wavelength of 496.5 nm and intensity (I) of 300 mW/cm^2.

(main frame) are due to formation of charge-separated transient species, *i.e.*, $P^{+}BHQ_A^{-}$. The formation of $P^{+}BHQ_A^{-}$, which lasts for ~ 100 milliseconds[16], leads to a bleach of P870 band and a shift of transition frequencies of $B_{A,B}$ and $H_{A,B}$ Zn-BChls, as illustrated by curve c of the main frame. This electric field-induced spectral band shift in the 750-820 nm region was previously observed in BRCs and is referred to as *electrochromic shift*.[20,21,28,32] As shown in the upper inset, there is also a shift in vibronic transition frequencies. Since the vibrational bands ~730 and ~754 nm (corresponding to vibrational frequencies of ~1150 and ~720 cm^{-1}, respectively) shift to shorter wavelengths in concert with the B band, they are assigned to the vibrational frequencies of $B_{A/B}$ Zn-BChls. Interestingly, similar modes are observed for BChl in solution.[33,34] In contrast, the weak feature at ~675.5 nm shifts "red" in concert with the H band, but the frequency of ~1900 cm^{-1} (from the H band) is too large and too intense to correspond to a vibrational mode of $H_{A,B}$ Zn-BChls. The presence of this small feature is not critical to the interpretation of our data, and most likely originates from a small sample contamination. This is supported by the fact that the intensity of this band was weakly sample dependent.

The Zn-RC transient PHB spectrum in the Q_x spectral range (Figure 3-3, curve c, lower inset) is dominated by a bleach of Q_x transition corresponding to the $P_{A/B}$ chlorophylls. However, a small contribution from an electrochromic shift of $H_{A,B}$ and $B_{A,B}$ Zn-BChls cannot be ruled out. Under our current experimental conditions, the P870 bleach in curve c is ~55 %, as shown in the main frame of Figure 3-3.

The main frame in Figure 3-4 shows the Q_y absorption spectrum of the Zn-β-RC measured without (curve a) and with (curve b) the burn laser on after the nonphotochemical hole

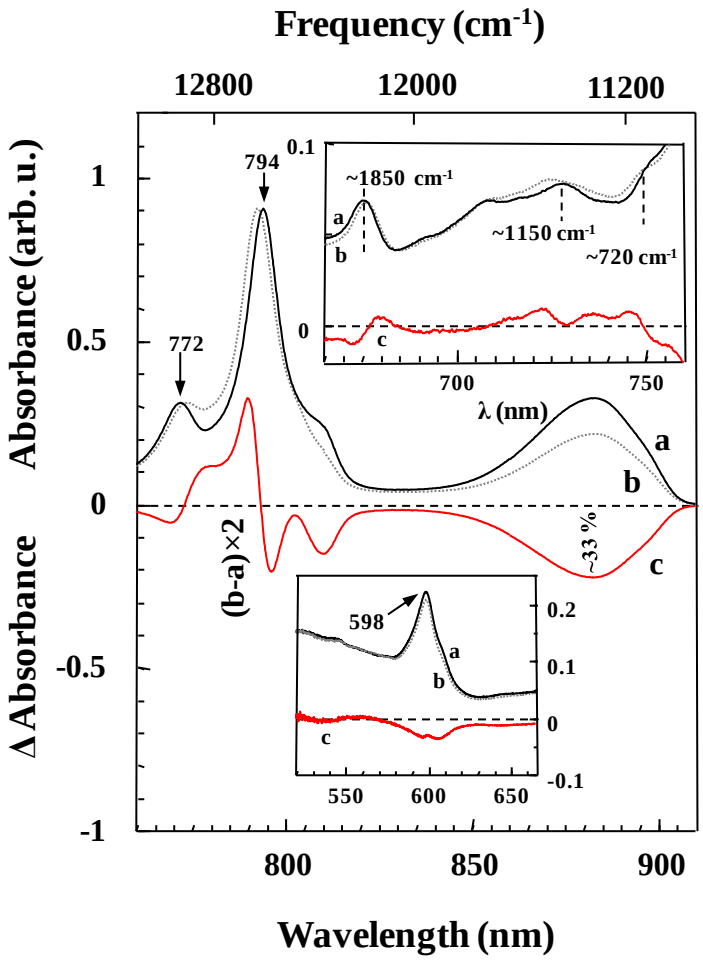

Figure 3-4 Curves a and b in the main frame and both insets correspond to preburn absorption spectrum of Zn-β-RC and absorption spectrum measured with burn laser on, respectively. For clarity, the Q_x- and vibronic-regions are shown separately in the lower and upper insets. Curves c (multiplied by a factor of two) are transient photochemical HB spectra obtained with the burn wavelength of 496.5 nm (I=300 mW/cm^2).

burning was complete. The difference spectrum c (b-a) corresponds to the transient PHB spectrum. The Q_x and vibronic spectral range of the spectra a, b and c are shown in the lower and upper insets, respectively. As in the case of the Zn-RC, the formation of $P^+BHQ_A^-$ results in: (1) P870 band bleaching; (2) an electrochromic shift of the Q_y transition frequency of $B_{A,B}$ (blue

shift) and $H_{A,B}$ (red shift) Zn-BChls, as shown by curve c of the main frame; and (3) shifts of vibronic transition frequencies (see upper inset). Again, vibrational modes of ~1150 and ~720 cm^{-1} (from the B band) shift blue in concert with the B band, therefore, these frequencies most likely belong to the $B_{A,B}$ Zn-BChls. Under similar experimental conditions as those used for the Zn-RC, the bleaching of the P870 band in the Zn-β-RC was ~33%. Assuming similar lifetimes of $P^+Q_A^-$ in both RCs, the decreased yield of $P^+Q_A^-$ formation in the Zn-β-RC could be associated with an increased rate of charge recombination of the $P^+H_A^-$ state in the Zn-β-RC, as suggested for the original β-RC in Ref[12]. We hasten to add that the % hole depth of the saturated nonphotochemical HB spectrum (data not shown) in both the Zn-RC and Zn-β-RC was less than 1 % due to very efficient charge separation in both samples.

Similar to the Zn-RC, the Zn-β-RC transient PHB spectrum in the Q_x region (Figure 3-4, spectrum c in lower inset) is dominated by Q_x bleaching of the $P_{A,B}$ Zn-BChls, with a small contribution from electrochromic shifts of both the B and H bands. However, there are two obvious differences in the transient PHB spectra of the Zn-β-RC (spectrum c in main frame of Figure 3-4) compared to the Zn-RC spectrum shown in Figure 3-3. The bleaching at ~810 nm which in absorption corresponds to the shoulder on the low energy side of the B band (often assigned in the literature[21,22,32] to the upper excitonic component of the special pair, *i.e.*, P_+) is more pronounced in the Zn-β-RC, and the H-band spectral changes around 772 nm, as expected, are very different. These differences are discussed in detail in section 4.2.

3.3.3. Photochemical HB spectra of P870 and theoretical fits

In the low temperature limit, the HB spectrum is defined by $\Delta A = A_t(\Omega, t) - A_{t=0}(\Omega)$, where $A_{t=0}(\Omega)$ is the pre-burn absorption spectrum, and

$$A(\Omega,t) = \int d\omega L_A(\omega-\Omega)N(\omega)e^{-P\sigma\phi L_A(\omega_B-\omega)t} \tag{3-1}$$

is the post-burn absorption spectrum. [11,35] In Eq. 3-1 ω_B is the burn/excitation frequency, P is the photon flux, t is the burn time and $N(\omega)$ is the pre-burn site distribution function (SDF), describing the probabilities of encountering different zero-phonon transition frequencies. $L_A(\omega)$ is the single site absorption profile and is defined by[11,35]

$$L_A(\omega-\Omega_0) = \underbrace{e^{-S}l_0(\omega-\Omega_0)}_{ZPL} + \underbrace{\sum_{R=1}^{\infty} S^R \frac{e^{-S}}{R!} l_R(\omega-\Omega_0-R\omega_k)}_{PSB} \quad . \tag{3-2}$$

The first term in Eq. 3-2 represents the Lorentzian ZPL $l_0(\omega-\Omega_0)$, which peaks at Ω_0 and possesses a homogeneous width Γ_{hom}. The second term is the PSB, consisting of a sum over all R-phonon transitions. On the basis of previous work[20,21,22], only two phonon profiles l_R (R = 1, 2) corresponding to peak frequencies ω_k (k = 1, 2) are required to simultaneously fit the absorption and PHB spectra of P870. We refer ω_1 (hereafter ω_m) to the mean phonon frequency and ω_2 (hereafter ω_{sp}) to the special pair marker mode[11,19,20,22]. Special pair marker modes are intermolecular vibrational modes localized on the special pair.[21,22] As before[11,19,20,22], The phonon line shape l_R (R = 1, 2) is described by a Gaussian (width Γ_G cm^{-1}, fwhm) and Lorentzian (width Γ_L cm^{-1}, fwhm) on the low and high energy sides, respectively.

The experimental PHB spectra (black dotted curves) of P870 and fits (red curves) for the Zn-RC and Zn-β-RC are shown in Figure 3-5 frame A and B, respectively. Note the perfect agreement between experimental curves and their fits. Unlike earlier modeling studies[19,20,21,22], experimentally determined inhomogeneity is used here. The parameters obtained from simultaneous fit of absorption and multiple PHB spectra of P870 for two samples are summarized in Table 3-1. The total Huang−Rhys factor is defined as $S_t = S + S_{sp}$, where S and S_{sp} are Huang−Rhys factors corresponding to protein phonons (ω in cm^{-1}) and special pair marker mode frequency (ω_{sp} in cm^{-1}), respectively.

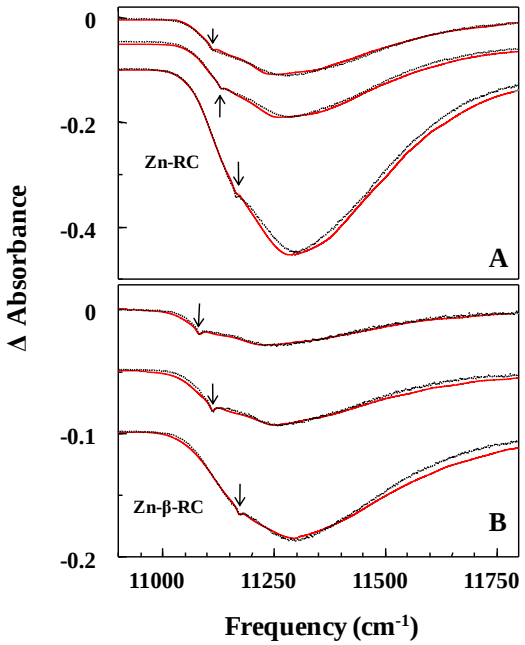

Figure 3-5 Black dotted curves in Frames A and B show experimental photochemical HB spectra of P870 for Zn-RC and Zn-β-RC, respectively. Calculated spectra are shown in red. Solid arrows in both frames refer to laser burn frequencies (ω_B), and correspond to 11111, 11131, 11164.6 cm^{-1} (top to bottom) in Frame A, and 11082, 11112, 11172.3 cm^{-1} (top to bottom) in Frame B, respectively. See Table 3-1 for fitting parameters.

Table 3-1 Electron-phonon coupling parameters

	ω_{sp} cm^{-1}	ω_m cm^{-1}	Γ_G^{ph} cm^{-1}	Γ_G^{sp} cm^{-1}	Γ_L^{ph} cm^{-1}	Γ_L^{sp} cm^{-1}	S ±0.1	S_{sp} ±0.1	S_t ±0.1
P870 (Zn-RC)[a,b]	120	25	35	30	55	30	2.4	1.5	3.9
P870(Zn-β-RC)[a,b]	130	25	35	55	70	55	2	1.5	3.5

Notes: a) SDF peak/width of 11120/110 cm^{-1} (black solid curve in Figure 6 frame A) and 11130/130 cm^{-1} (black solid curve in Figure 6 frame B) were used for Zn-RC and Zn-β-RC, respectively. b) Γ_{hom} of ~5 cm^{-1} was used for both samples which is very close to average half width half maximum of experimental ZPH. ph=phonon, sp=special pair, t=total.

3.3.4. Zero phonon hole (ZPH) action spectra and electron transfer times

ZPH action spectroscopy allows investigation of the lowest energy state(s) as well as determination of inhomogeniety of various molecular systems[10,25,26,36,37,38] embedded in a glassy matrix at low temperatures**.** In ZPH action spectroscopy (in absorption mode), the burn wavelength (λ_B) dependence of *nonphotochemical* ZPH depth is probed under a constant irradiation dose, *i.e.*, a constant fluence. Fluence is defined as f=I×t, where I is laser intensity and t is irradiation time. But here, for the first time, we have attempted to extract ZPH action spectra by probing burn wavelength (λ_B) dependence of *photochemical* ZPH depth under constant laser intensity. This allows us to find the inhomogeneous broadening (Γ_{inh}) of the lowest-energy charge separating state.

In Figure 3-6 the black dotted curves in frame A (Zn-RC) and frame B (Zn-β-RC) show the experimental absorption spectra of P870. Fits to the absorption spectra, hardly

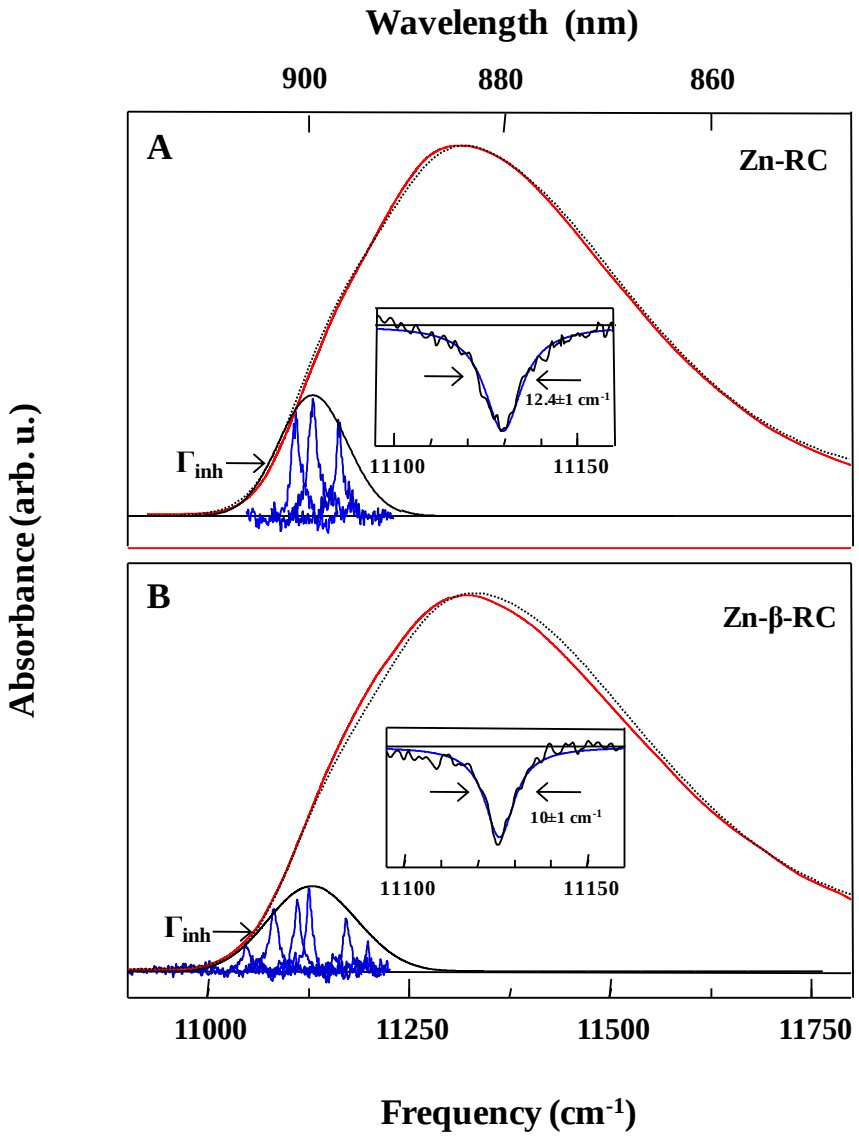

Figure 3-6 Frames A and B show experimental P870 absorption band (black dotted curves) of Zn-RC and Zn-β-RC, respectively. Calculated absorption spectra are shown in red. The blue color sharp spikes in both frames (in the ~11000-11250 cm^{-1} region) show the inverted ZPHs. The ZPHs were measured under identical conditions (I = 250 mW/cm^2, read resolution = 1 cm^{-1}). The insets show a blowup of the experimental (black) ZPHs obtained with the burn wavelength (λ_B) of 898.4 nm (ω_B = 11131 cm^{-1}) (frame A) and 898.7 nm (ω_B = 11127 cm^{-1}) for Zn-RC (frame A) and Zn-β-RC (frame B), respectively. The Lorenzian fits of the ZPHs are shown in blue.

distinguishable from experimental spectra, are shown as red curves. The equations used to simultaneously describe both absorption and PHB spectra were given in section 3.3. The sharp blue spikes in the 11000-11250 cm^{-1} frequency region shown in frames A and B are the inverted ZPH spectra for the Zn-RC and Zn-β-RC, respectively. These inverted sharp ZPH are obtained by fitting Lorentzian curves to the ZPH, and subtracting broad contributions from the transient PHB spectra of P870 measured at different λ_B under constant laser intensity. Representative ZPHs with Lorentzian fits are shown in the insets of Figure 3-6. Solid black curves in frame A (Zn-RC) and B (Zn-β-RC) represent the Gaussian distribution of ZPHs with inhomogeneous broadening (Γ_{inh}) of 100±10 cm^{-1} and 130±10 cm^{-1}, respectively. These curves provide the SDF of the primary donor state (P870) in Zn-RC and Zn-β-RC. Each sharp spike in both frames can be fitted with a Lorentzian profile, as it reflects the homogeneous linewidth (*i.e.*, Γ_{hom} = 1/2 ZPH width[10,11,18]). A weakly λ_B-dependent ZPL width ranging from 9 to 11 cm^{-1} is obtained for both samples. The ET time is obtained from Γ_{hom} using Eq. 3-3[10,11,18]

$$\Gamma_{hom}\,(cm^{-1}) = (1/2\pi cT_1 + 1/2\pi c\tau_{ET}) + 1/\pi cT_2^{*} \approx 1/2\pi c\tau_{ET}\,, \qquad (3\text{-}3)$$

where T_1 is the fluorescence lifetime, T_2^{*} is the "pure" dephasing time, which at (T = 5 K) is very large in comparison to T_1, c is the velocity of light in cm/s, and τ_{ET} is the electron transfer time. Eq. 3-3 provides τ_{ET} since the latter is << T_1. Our data reveal the both Zn-RC and Zn-β-RC have the average ET time of ~1 ps.

3.4. Discussion

3.4.1. Low temperature absorption spectra

It was previously established that in the WT-RC the Q_y transitions of the H_A and B_A cofactors lie at higher energies than the H_B and B_B cofactor transitions.[27,28,39] This is also true for the Zn-RC and Zn-β-RC, because the inter-pigment distance and orientation should not be altered from WT-RC. Excitonic calculations[21,27,40] showed that nearest neighbour V_{nm} coupling (*i.e.*, B_A-H_A and B_B-H_B coupling) is in the range of 100-200 cm^{-1}. This has been confirmed by the recent two color three pulse phonon echo peak shift spectroscopy, which directly measured the B-H coupling of 170 ±30 cm^{-1}.[41] In the absence of a crystal structure of the Zn-RC and Zn-β-RC (research in progress), the coupling constants cannot be calculated at the present time, however, the B-H coupling in the Zn-RC should not alter much from that observed in the WT-RC.

It has been established that the Q_x transition of metalloporphyrins is more sensitive than the Q_y transition to the co-ordination state of the metal center.[42] For example, the Q_x/Q_y transitions of Zn-BChl *a* in solution at room temperature lie at ~560/760 nm (tetra-coordinated) and 580/770 nm (penta-coordinated).[42] Thus, it appears that in solution a change from tetra- to penta-coordination of Zn-BChl results in a relatively large red shift of both the Q_x- and Q_y-transition. In the case of the Zn-β-RC, the change from tetra- to penta-coordination of Zn-BChl in the H_A site results in a red shift of the H band Q_x-transiton, but the Q_y-transition shifts to the blue. It is interesting to note that B Q_y-band also shifts to the blue (Figure 3-2 frameA, curve b). The blue shift of both the B and H Q_y-bands in the absorption spectrum of the Zn-β-RC (Figure 3-2 frame A, curve b) most likely originates from a modification of excitonic interaction (due to modified

pigment site energies) induced by the tetra- to penta-coordination change of the H_A site Zn-BChl. Such a correlated blue shift of both the H and B Q_y-bands might contribute to the efficient H to B excitation energy transfer (EET) in the Zn-β-RC. Figure 2B shows that mutation of the M214 residue from Leu to His results in about a 38 nm red shift in the Q_x transition wavelength of the H_A Zn-BChl. This observation is similar to that reported in[43] where a change from penta- to hexa-coordination of the B_B BChl in the WT-RC resulted in a red shift of Q_x transition (at 77 K) of about 31 nm. Since, as stated earlier, the 560 nm band belongs to Q_x transitions of both $H_{A,B}$ cofactors, one would expect that the intensity of this band should decrease only by half, as only the H_A site was intentionally modified. It is puzzling that this band disappears completely. In the absence of a high resolution crystal structure of both the Zn-RC and Zn-β-RC, at the present time we only can offer three tentative explanations:

1) Optical spectra suggest that the Zn-RC and Zn-β-RC assembles without the H_B cofactor and/or during the isolation procedure this co-factor is lost. The latter possibility cannot be excluded, as it was shown in literature[44] that mutation of the M149 residue from Ala to Trp in the *Rb. sphaeroides* RC led to an RC lacking the H_B (BPhe) cofactor. Interestingly, in this mutant[44] the time constants of active branch charge separation were not altered, as observed in the case of the Zn-RC and Zn-β-RC. A similar conclusion was reached for L185 Leu to His mutant[44], where the H_B BPhe was replaced with BChl. For example, if the absorption spectrum of the M149 Ala to Trp mutant reported in Figure 4a of[44] is compared to the absorption spectrum of the Zn-RC shown in Figure 3-2 of this work, two similar spectral features are revealed. That is, in both cases, unlike in the WT-RC, the $H_{A,B}$ Q_x-band does not split, and the

shoulder on the low-energy side of the B Q_y-band is absent. In addition, careful examination of many low temperature absorption spectra of *Rb. sphaeroides* WT-RCs reported in literature[20,21,28,29,30,31] led us to conclude that the distinct shoulder near 820 nm (at 5 K in WT *Rb. sphaeroides*) is present only in some i.e. the best RC preparation, and most likely (see below) RCs containing Car, and it belongs to the Q_y transition of the B_B BChl. Because B_B is close to the Car and H_B, a possible loss of BChl from the H_B site (as in the M149 Ala to Trp mutant[44]), or loss of Car (as in the R-26 mutant[21,30,31]) gives the B_B band a more monomeric character. This could lead to a blue shift of the Q_y transition wavelength of B_B, resulting in disappearance of the 810-820 nm shoulder (at ~810 nm in the Zn-RC and ~820 nm in the WT-RC). These two observations (*i.e.*, the absence of a 810 nm shoulder on the lower energy side of the B Q_y-band and the absence of H Q_x-band splitting could suggest that Zn-RC and Zn-β-RC lack the H_B BChl. The absence of the H_B BChl would explain why the H Q_x-band near 560 nm completely disappears in the Zn-β-RC (see Figure 3-2 frame B). We suggest that the intensity of the H Q_y-band in the Zn-RC and Zn-β-RC is too weak (compared to the WT-RC[16], and assuming a similar oscillator strength of BChl in the WT-RC and Zn-BChl in the Zn-RC) to account for a contribution of two Zn-BChl pigments in the H Q_y-band transitions of the Zn-RC and Zn-β-RC It is also possible that spectral differences observed around the B Q_y-band (including the 810 nm shoulder) are due to the loss of carotenoid in Zn-RC (see below for further discussion).

2) Another possibility is that Zn-β-RC contains two mutations, *i.e.*, L185 Leu → His and M214 Leu → His, resulting in penta-coordination of both $H_{A,B}$ Zn-BChls. The observation that the

$H_{A,B}$ Q_X-band at ~560 nm completely disappears with a concomitant increase in intensity of the Q_x band at ~600 nm supports this idea. It cannot be excluded that the H_B Zn-BChl (in both the Zn-RC and Zn-β-RC) is ligated by an intervening water molecule, so H_B Q_x transition lies in the range of 590-610 nm and not ~560 nm. In fact, it was reported that ligation by a water molecule can cause a large (~31 nm) Q_x shift[43].

3) It could be conceived that neither penta-coordination of the H_B Zn-BChl nor its absence is possible. In this case one must explain the spectral changes observed in both the Q_x and Q_y transitions by considering redistribution of the oscillator strength between Q_x and Q_y transitions of excitonically coupled $H_{A,B}$ and $B_{A,B}$ chromophores. Although intensity borrowing between Q_y excitonic states is not unusual, point mutation-induced intensity borrowing between Q_x and Q_y transitions, to our knowledge, has not been reported for any RC.

In summary, no final conclusion regarding the number of cofactors can be reached at this point. We suggest that the most likely scenario is given by explanation number 2 (*vide supra*). The spectral changes between the Zn-RC and the Zn-β-RC in the range of 750 to 820 nm can be explained by considering: 1) mutation-induced changes in the H_A site; 2) the presence of more carotenoid in Zn-β-RCs than in the Zn-RCs. However, complete disappearance of Q_x band ~560 nm in Zn-β-RC can only be explained considering that Zn-BChls in $H_{A,B}$ sites are penta-coordinated.

3.4.2. On the nature of the 810 nm shoulder observed on the low-energy side of the B Qy- band in absorption spectra of the Zn-RC and Zn-β-RC

There are conflicting opinions regarding the shoulder present on low energy side of the Q_y B-band in BRCs.[20,21,22,28,32,48] For example, this shoulder (at 5 K) appears at ~850 in the *Rps. viridis*[22,32] and ~820 nm in the *Rb. sphaeroides*[20,21,22,28] WT-RC. Earlier semi-emperical[27] and excitonic[45] calculations did not assign this shoulder to the P_+ excitonic component (*vide supra*). However, on the basis of polarization excitation spectra[46] it was concluded that the shoulder on the low energy side of the B Q_y-band in low temperature absorption spectra of the *Rps. viridis* RC is an upper excitonic component (P_+) of P960 (the special pair). A similar conclusion was reached on the basis of NPHB experiments on the *Rps. viridis* P960.[32] On the basis of λ_B-dependent PHB spectra of P870[47] it was suggested that the shoulder near 820 nm in the *Rb. sphaeroides* WT-RC has significant contribution from P_+. Although Ref.[22] confidently assigns the lower energy side absorption to P_+, our data do not support this assignment. That is, it is not clear why: 1) electron-phonon coupling of the ~820 nm (in *Rb. sphaeroides*) and/or ~850 nm (in *Rps. viridis*) bands is very weak in comparison to P870 and P960, respectively; and 2) linear pressure shift of this band is very weak and is similar to that observed for a monomer. Interestingly, low temperature (5 K) Stark spectra of *Rb. sphaeroides* and the original β-mutant were interpreted[28] as indicating that P_+ of P870 is near 800 nm (underneath the B Q_y-band but not the 820 nm shoulder), and carries a very small oscillator strength relative to the Q_y transition. This assumption was based on a picosecond circular dichroism study of the *Rb. sphaeroides* RC reported in Ref[48]. Picosecond photodichroism studies of the *Rb. sphaeroides* RC at 5 K also

suggested that the low energy shoulder of B Q_y-band is comprised mainly of one of the two BChls that are not part of P.[49] Thus, there is no general consensus on the origin of the above discussed shoulder. However, our data support the conclusions reached in Refs 28 and 48, as discussed above, *i.e.*, the P_+ component in BRCs must be very weak and is obscured by an overlapping B band. Recall, as discussed above, that the variable intensity of this shoulder in various BRCs may indicate the absence of carotenoid and/or lack of the H_B pigment in mutated BRCs. One more indication that the low energy side absorption does not belong to the P_+ excitonic component of the special pair comes from the 77 K absorption spectrum of a M202 His to Leu mutant (the "heterodimer" mutant) reported in Ref.[50], where it was shown that in absorption spectra of the M202 His to Leu mutant the P870 band is very weak, but the lower energy side of B Q_y-band is as intense as in the WT-RC.

Therefore, we conclude that data reported in this work are inconsistent with a previous suggestion[22,47] that the lower energy shoulder observed near 820 nm in WT *Rb. sphaeroides* within the B Q_y-band in low temperature transient spectra of the *Rb. sphaeroides* is an upper excitonic component of P870 (i.e. P_+). If one accepts that the ~810 nm shoulder in Zn-RC and well resolved band near 810 nm band in Zn-β-RC are due to P_+, it is hard to see why a simple point mutation makes the shoulder so much stronger in the Zn-β-RC (see main frames of Figures 3-3 and 3-4). To explain this one would have to assume that the Leu --> His mutation in the H_A site results in a significant change in the relative orientation of transition dipoles of P_A and P_B. This does not seem feasible and, as pointed earlier, the increase in intensity of the 810 nm shoulder in the absorption spectrum (see curve b in Figure 3-2, frame A) and the 810 nm band in

transient spectrum (curve c, main frame of Figure 3-4) in the Zn-β-RC must have a different origin, as discussed above.

In addition, our resonant PHB spectra of P870 also do not support the idea that the 810 nm shoulder is due to P_+. The resonant PHB spectra of the Zn-β-RC burn at the blue (curve a) and red (curve b) edges of SDF are re-plotted in Figure 3-7 (spectra are normalized to the same intensity of P870 bleaching). Unlike the centroid of the P870 bleach, the bleach at ~810 nm does not shift at all. This shows that the feature at ~810 is not correlated with P870. This again proves that the low energy shoulder near 810 nm in absorption spectrum is not necessarily associated

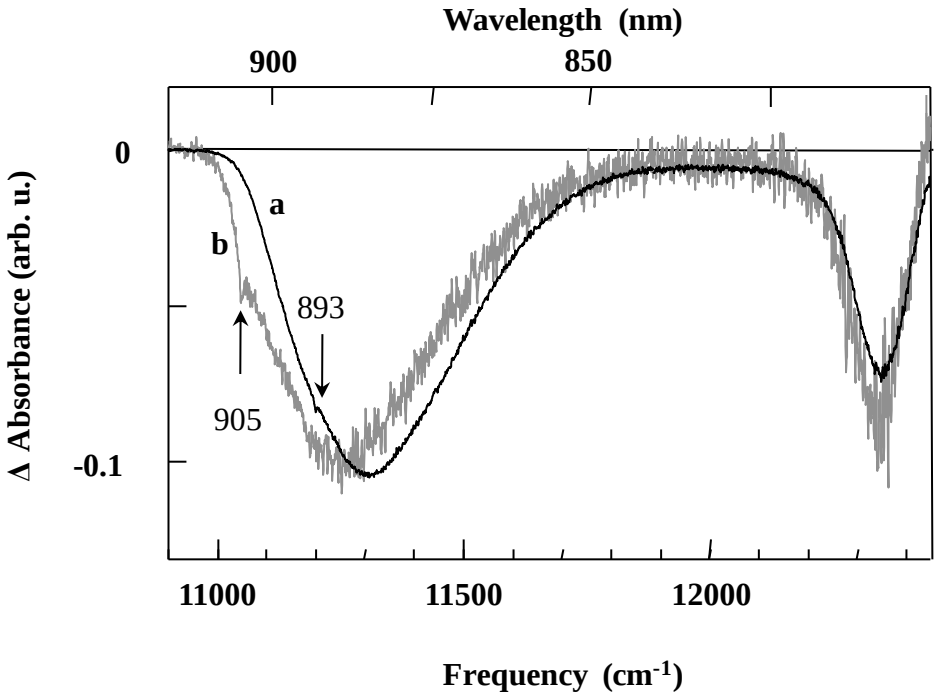

Figure 3-7 Photochemical HB spectra of P870 for Zn-β-RC at λ_B of 893 nm (ω_B=11198.2 cm^{-1}, spectrum a) and 905 nm (ω_B=11049.7 cm^{-1}, spectrum b). Spectra are normalized to same P870 bleach.

only with P_+. As stated earlier, the major contribution to the low energy shoulder in absorption spectrum comes from B_B. If the transition frequency of B_B is slightly perturbed, for example due to the absence of a nearby carotenoid and/or H_B, the B_B band due to modified excitonic interactions and different composition of various excitonic states, could undergo a blue shift leading to decreases intensity of this shoulder. This interpretation is in accord with the variable intensity of 810/820 nm shoulder in various low temperature absorption spectra of various *Rb. sphaeroides* samples[16,20,22,28,31,30]. The absence of the low energy shoulder in the absorption spectrum of the Zn-RC shown in Figure 3-2 may be, as stated earlier, due to loss of carotenoid. Further biochemical studies of Zn-RC and Zn-β-RC should confirm or reject this hypothesis.

Finally, we comment on the different shapes of PHB spectra of the Zn-RC (especially in the range 770-820 nm; see Figure 3-3 curve c in the main Frame) and the Zn-β-RC (see Figure3-4, curve c in the main frame). If one accounts for the shift in absorption between the Zn-RC and Zn-β-RC, the major changes in the two PHB spectra are observed at ~810 nm (corresponding to the lower energy spectrum of the B Q_y-band) and ~775 nm (H Q_y-band). The more pronounced bleaching at ~810 in the Zn-β-RC (consistent with more absorption ~810 nm), as stated earlier, is not associated to P_+ and we believe it comes from an electrochromic shift of B_B. We agree with the findings of Ref.[28] that because of lower effective dielectric constant on M side (i.e. inactive branch) the B branch co-factors (B_B and H_B) show more electrochromic shift than the A branch cofactors (H_A, B_A).

3.5. Conclusions

We have shown that the coordination state of H_A in the Zn-RC does not tune the electron transfer rate. Formation of the $P^+Q_A^-$ state is observed in both the Zn-RC and the Zn-β-RC, although under identical experimental conditions significantly deeper P_- band (corresponding to the lower-energy, special pair, excitonic component) was observed in the Zn-RC. However, the average (weakly frequency-dependent) low-temperature ET times (measured from ZPHs in resonant transient HB spectra) are comparable (within ~1 ps) and similar to those previously observed in the WT-RC[47]. ET rates observed in this work for the Zn-RC are in good agreement with recent room-temperature, time-domain data.[16] Our data suggest, in agreement with Ref.[28,48], that bleaching at ~810 nm is not associated with an upper excitonic component (P_+) of P870, but it originates from an electrochromic shift of the B_B Zn-BChl. ZPH-action spectra revealed inhomogeneous broadening (Γ_{inh}) of ~110 cm^{-1} (Zn-RC) and ~120 cm^{-1} (Zn-β-RC). Simultaneous fit of the absorption and resonant/nonresonant HB spectra for both types of RC, using experimentally determined Γ_{inh}, provided a total Huang-Rays factor of 3.9±0.1 for the Zn-RC and 3.5±0.1 for the Zn-β-RC as compared to value of 3.7 and 3.2 observed for WT *Rb. sphaeroides* and *Rps. viridis* RCs, respectively.[21]

Acknowledgements

This work was supported by the DOE BES (EC9987 Award) to RJ and in part by the DOE EPSCoR/DOE BES (DE-FG02-08ER46504) grant (RJ). Work at the University of British Columbia was supported by a Discovery Grant to JTB from the Canadian Natural Sciences and Engineering Research Council. We acknowledge Dr. V. Zazubovich from Concordia University (Department of Physics, Montreal, Quebec, Canada) for sharing with us his recently updated version of the software to describe HB spectra.

References

(1) Qian, P.; Hunter, C. N.; Bullough, P. A. *J. Mol. Biol*. **2005**, *349*, 948.

(2) Scheuring; S.; Busselez, J.; Levy, D. *J. Biol. Chem*. **2005**, *280*, 1426.

(3) Scheuring, S.; Francia, F.; Busselez, J.; Melandri, B. A.; Rigaud, J. L.; Levy, D. *J. Biol. Chem.* **2004**, *279*, 3620.

(4) Yeates, T. O.; Komiya, H.; Chirino, A.; Rees, D. C.; Allen, J. P.; Feher, G. *Proc. Natl. Acad. Sci. U. S. A.* **1988**, *85*, 7993.

(5) Lancaster, C. R. D., Ermler, U., Michel, H. In *Anoxygenic photosynthetic bacteria*, Blankenship, R. E., Madigan, M. T., Bauer, C. E. (Eds), Kluwer Academic Publishers: Dordrechet, The Netherlands, 1995; pp. 503-526.

(6) Arlt, T., Schmidt, S., Kaiser, W., Lauterwasser, C., Meyer, M., Scheer, H. & Zinth, W. *Proc. Natl. Acad. Sci. U. S. A.***1993**, *90*, 11757.

(7) Jones, M. R. *Biochem. Soc. Transact*. **2009**, *37*, 400.

(8) Williams, J. C., Allen, J. P. In *The purple phototrophic bacteria*, Hunter, C. N., Daldal, F., Thurnauer, M. C., Beatty, J. T. (Eds), Springer Science: Dordrechet, The Netherlands., 2009; pp. 337-353.

(9) Woodbury, N. W., Allen, J. P. In *Anoxygenic photosynthetic bacteria* Blankenship, R. E., Madigan, M. T., Bauer, C. E. (Eds), Kluwer Academic Publishers: Dordrechet, The Netherlands, 1995; pp. 527-557

(10) Jankowiak, R.; Reppert, M.; Zazubovich, V.; Pieper, J.; Reinot, T. *Chem. Rev*. **2011,** *111*, 4546.

(11) Jankowiak, R.; Hayes, J. M.; Small, G. J. *Chem. Rev* **1993**, *93*, 1471.

(12) Kirmaier, C.; Gaul, D.; DeBey, R.; Holten, D; Schenck, C. C. *Science* **1991**, *251*, 922.

(13) Wang, H.; Lin, S.; Allen, J. P.; Williams, J. C.; Blankert, S.; Laser, C.; Woodbury, N. W. *Science* **2007**, *316*, 747.

(14) Jaschke, P. R.; Beatty, J. T. *Biochemistry* **2007**, *46*, 12491.

(15) Jaschke, P. R.; Hardjasa, A.; Digby, E. L.; Hunter, C. N.; Beatty, J. T. *J. Biol. Chem.* **2011**, *286*, 20313.

(16) Lin, S.; Jaschke, P. R.; Wang, H.; Paddock, M.; Tufts, A.; Allen, J. P.; Rosell, F. I; Mauk, A. G.; Woodbury, N. W.; Beatty, J. T. *Proc. Natl. Acad. Sci. U. S. A.* **2009**, *106*, 8537.

(17) Allen, J. P.; Feher, G.; Yeates, T. O.; Rees, D. C.; Deisenhofer, J.; Michel, H. and Huber, R. *Proc. Natl. Acad. Sci. U. S. A.* **1986**, *83*, 8589.

(18) Moerner, W. E. *Topics in current physics, Persistent Spectral Hole Burning: Science and Applications*, Springer-Verlag: New York, 1987; p 1

(19) Johnson, S. G.; Tang, D.; Jankowiak, R.; Hayes, J. M.; Small, G. J. *J. Phys. Chem.* **1990**, *94*, 5849.

(20) Johnson, E. T.; Nagarajan, V.; Zazubovich, V.; Riley, K.; Small, G. J.; Parson, W. W. *Biochemistry* **2003**, *42*, 13673.

(21) Lyle, P. A.; Kolaczkowski, S. V.; Small, G. J. *J. Phys. Chem.* **1993**, *97*, 6924.

(22) Small, G. J. *Chem. Phys.* **1995**, *197*, 239.

(23) Jaschke, P.R.; Drake, I.; Beatty, J. T. *Photosynth. Res.* **2009**, *102*, 95.

(24) Goldsmith, J. O.; Boxer, S. G. *Biochim Biophys Acta Bioenerg* **1996**, *1276*, 171.

(25) Neupane, B.; Dang, N. C.; Acharya, K.; Reppert, M.; Zazubovich, V.; Picorel, R.; Seibert, M.; Jankowiak, R. *J. Am. Chem. Soc.* **2010**, *132*, 4214.

(26) Dang, N. C.; Zazubovich, V.; Reppert, M.; Neupane, B.; Picorel, R.; Seibert, M.; Jankowiak, R., *J. Phys. Chem. B* **2008**, *112*, 9921.

(27) Warshel, A.; Parson, W. W. *J. Am. Chem. Soc.* **1987**, *109*, 6152.

(28) Steffen, M. A.; Lao, K.; Boxer, S. G. *Science* **1994**, *264*, 810.

(29) Meech, S. R.; Hoff, A. J.; Wiersma, D. A. *Proc. Natl. Acad. Sci. USA* **1986**, *83*, 9464.

(30) Lin, S.; Jackson, J. A.; Taguchi, A. K. W.; Woodbury, N. W. *J. Phys. Chem. B* **1999**, *103*, 4757.

(31) Vos, M. H.; Lambry, J.-C.; Robles, S. J.; Youvan, D. C.; Breton, J.; Martin, J.-L. *Natl. Acad. Sci. USA* **1992**, *89*, 613.

(32) Reddy, N. R. S.; Kolaczkowski, S. V.; Small, G. J. *Science* **1993**, *260*, 68.

(33) Zazubovich, V.; Tibe, I.; Small, G. J. *J. Phys. Chem. B* **2001**, *105*, 12410.

(34) Rätsep, M.; Cai Z.-L.; Reimers J. R.; Freiberg, A. *J. Chem. Phys.* **2011**, *134*, 024506.

(35) Hayes, J. M.; Lyle, P. A.; Small, G. J. *J. Phys. Chem.* **1994**, *98*, 7337.

(36) Feng, X.; Neupane, B.; Acharya, K.; Zazubovich, V.; Picorel, R.; Seibert, M.; Jankowiak, R. *J. Phys. Chem. B* **2011** (in press).

(37) Purchase, R.; Völker, S. *Photosynth. Res.* **2009**, *101*, 245.

(38) Neupane, B.; Dang, N. C.; Kelley, R. F.; Wasielewski, M. R.; Jankowiak, R. *J. Phys. Chem. B* **2011**, *111*, 4546.

(39) Huang, L.; Wiederrecht, G. P.; Utschig, L. M.; Schlesselman, S. L.; Xydis, C.; Laible, P. D.; Hanson, D. K.; Tiede, D. M. *Biochemistry* **2008**, *47*, 11387.

(40) Plato, M.; Moebius, K.; Michel-Beyerle, M. E.; Bixon, M.; Jortner, J. *J. Am. Chem. Soc.* **1988**, *110*, 7279.

(41) Parkinson, D. Y.; Lee, H.; Fleming, G. R. *J. Phys. Chem. B* **2007**, *111*, 7449.

(42) Hartwich, G.; Fiedor, L.; Simonin, I.; Cmiel, E.; Schäfer, W.; Noy, D.; Schertz, A.; Scheer, H. *J. Am. Chem. Soc*. **1998**, *120*, 3675.

(43) Frolov, D.; Marsh, M.; Crouch, L. I.; Fyfe, P. K.; Robert, B.; van Grondelle, R.; Hadfield, A.; Jones, M. R. *Biochemistry* **2010**, *49*, 1882.

(44) Watson, A. J.; Fyfe, P. K.; Frolov, D.; Wakeham, M. C.; Nabedryk, E.; van Grondelle, R.; Breton, J.; Jones, M. R. *Biochim. Biophys. Acta* **2005**, *1710*, 34.

(45) Knapp, E. W.; Scherer, P. O. J.; Fischer, S. F. *Biochim. Biophys. Acta*. **1986**, *852*, 295.

(46) Vermeglio, A.; Paillotin, G. *Biochim. Biophys. Acta*. **1982,** *681*, 32.

(47) Johnson, S. G.; Tang, D.; Jankowiak, R.; Hayes, J. M.; Small, G. J.; Tiede, D. M. *J. Phys. Chem*. **1989**, *93*, 5953.

(48) Xie, X.; Simon, J. D. *Biochim. Biophys. Acta*. **1991**, *1057*, 131.

(49) Kirmaier, C.; Holten, D.; Parson, W. W. *Biochim. Biophys. Acta*. **1985**, *810*, 49.

(50) King, B. A.; de Winter, A.; McAnaney, T. B.; Boxer, S. G. *J. Phys. Chem. B* **2001**, *105*, 1856.

Chapter 4 - Low-Temperature Frequency Domain Study of Excitation Energy Transfer in Ethynyl-Linked Chlorophyll-Trefoils and Aggregates

(Paper published in J. Phys. Chem. B 2011,135, 10391)

Bhanu Neupane, Nhan C. Dang, Richard F. Kelley, Michael R. Wasielewski, Ryszard Jankowiak

Abstract

Using hole-burning spectroscopy, we show that excitation energy transfer (EET) time in ethynyl-linked chlorophyll trefoil (ChlT1) monomer is very fast (~2.5 ps) at liquid helium temperature. This is consistent with data obtained by femtosecond transient spectroscopy experiments performed at room temperature, where an EET time of 1.8 ps was observed (Kelley, R. F. et al. *Angew. Chem. Int. Ed*. **2006**, 45, 7979). This finding further supports the importance of through-bond electronic coupling at low temperature. In addition, we show that ChlT1 (even at very low concentrations) in methyl tetrahydrofuran-ethanol glass (1:200 v/v; T ~5 K) forms different types of aggregates. It is demonstrated that the relative distribution of various types of aggregates (whose possible structures are briefly discussed) depends on cooling rate and matrix composition. For example, EET time in two types of ChlT1-based aggregates is slower by a factor of about 5–7 with respect to that observed for ChlT1 monomer. This indicates that ChlT1 aggregates can retain similar ultrafast energy transfer properties as those observed in natural photosynthetic antennas. It is anticipated that such building blocks could be utilized in future photovoltaic devices.

4.1. Introduction

Natural photosystems contain chlorophylls (Chls) as major building blocks to harvest solar energy in the formation of a charge-separated state. Different protein subunits optimize the overall process of photosynthesis in space, frequency, and time resulting in a photon-to-charge conversion efficiency close to 100 %.[1-4] Inspired by natural photosynthesis, different groups[5-22] are interested in mimicking natural photosynthesis using different types of synthetic molecules, including chlorophyll-trefoils (ChlTs). These molecules consist of three identical zinc-Chl subunits connected by rigid linkers (ethynyl or phenyl-ethynyl) to the central benzene unit facilitating EET through both space and bond energy transfer.[23] The beauty of these molecules is that – depending on solvent polarity, temperature, and their concentration – they self aggregate to form building blocks of different sizes, thus increasing absorption efficiency and also making multidirectional energy flow possible. In this regard, ChlTs seem to be well optimized for very efficient light harvesting[23], mimicking various natural photosynthetic antenna systems.[24-38]

Excitation energy transfer (EET) in ChlTs in THF was previously studied by room-temperature transient absorption spectroscopy[23]. It was shown that EET in ChlT having ethynyl linkers (referred to below as ChlT1; see Figure 4-1) is ~2 ps, about three times faster than in ChlT having phenyl-ethynyl linkers (labeled below as ChlT2).[23] This difference in EET between ChlT1 and ChlT2 is due to more effective through-space and through-bond coupling between zinc-Chl subunits in ChlT1.[23] Very recently, photophysical properties of ChlT1 and ChlT2 (along with their respective monomeric units M1 and M2) were studied at the single molecule level.[39] The later work demonstrated that ChlT1 is more photostable and less structurally flexible than ChlT2. This observed difference in properties between ChlT1 and ChlT2 was interpreted as a direct result of stronger electronic coupling and more rigid linkers in ChlT1.[23,39]

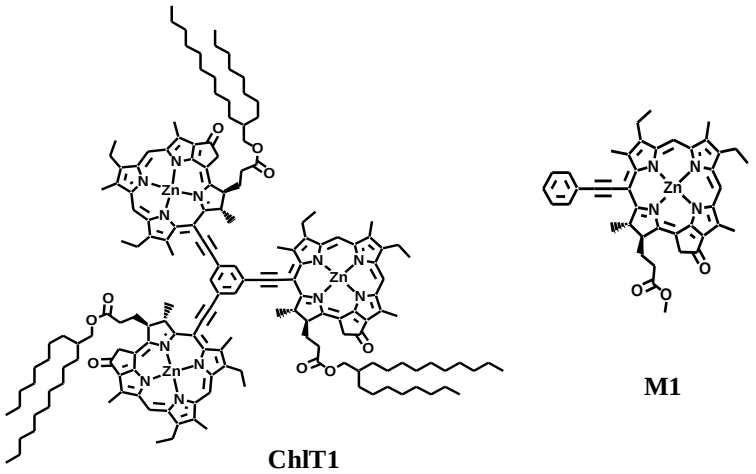

Figure 4-1 Structure of trefoil (ChlT1) and its monomer (M1).

In this work, we further characterize ChlT1 and its aggregates using spectral hole-burning (HB) spectroscopy. This is a well known and powerful frequency domain technique to study EET and excitonic structure in complex biomolecules.[40-44] The low-temperature aggregates (T = 5 K) are formed in 2-methyltetrahydofuran (MTHF) and ethanol glass (~1:200 v/v), while changing the stoichiometric ratio of ethanol, MTHF, and water controls the composition of the room-temperature aggregates. Findings of the HB experiments are compared with femtosecond pump-probe experiments[23] and the recently obtained single trefoil data.[39] We anticipate that further characterization of ChlT1 and its aggregates will provide more information on the structure-function relationship in these interesting systems and will pave the way for design of better artificial antennae for light harvesting in future photovoltaic devices. Possible structures of ChlT1 aggregates are discussed in light of previously published data obtained for Chl *a* aggregates.[45-54] In particular, we point out that not only ChlT1 monomer, but also various self-aggregated trefoils, carry out ultrafast excitation energy transfer. It is shown that EET time is

slower in large aggregates by a factor of about 5–7 with respect to that observed for ChlT1 (2.5 ps).

4.2. Materials and methods

4.2.1 Sample preparation

The approach for synthesis of chlorophyll trefoil (ChlT1) and its monomeric subunit (M1) is described in Ref[23]. Sample preparation for spectroscopic measurements was done in a nitrogen-purged atmosphere using 2-methyltetrahydrofuran (Acros Organics, extra dried over molecular sieve, 99+% purity and molecular weight of 86.13) and ethanol (Pharmaco-Aaper, absolute ACS/USP grade, 99.98 % purity with 0.02% water) as solvents. Solvent stoichiometry and concentrations of ChlT1 and M1 used are given in the figure captions. Cooling time required for reaching 5 K, for slow- and fast-cooling samples, was ~20 and ~2 minutes, respectively.

4.2.2 Spectroscopic measurement

The detail description for the measurement of HB and fluorescence spectra in provided in Chapter I. For resonant Raman spectra, a He-Ne laser (λ=630 nm, I~10 mW/cm^2) was focused on a glass slide with a concave well that could hold ~60 μL of solution, and spectra were measured using a confocal Raman Microspectroscope (Horiba Jobin-Yvon microscope and iHR 550 spectrometer) at a resolution of ~2 cm^{-1}. During measurement, the sample was covered with a microscope slide to prevent possible solvent evaporation and signal fluctuation.

4.3. Results

4.3.1. Absorption, nonresonant HB, and fluorescence spectra for fast- and slow-cooled samples of ChlT1 at 5 K

The 5 K absorption spectra obtained for sample 1s (s stands for slow cooling; curve a) and sample 2f (f indicates fast cooling; curve a) are shown in Figure 4-2 in frames A and B, respectively. Note that absorption spectrum of the slowly cooled sample is slightly broader and red shifted with more absorption, particularly in the spectral range of 680-710 nm. HB spectra in both frames (labelled 1-6) were obtained using the same fluence of 6, 18, 120, 360, 540, and 1440 J/cm^2. Spectra labeled 1 and 6 in both frames represent HB spectra obtained in the very early stages of the HB process (i.e. so called shallow holes) and saturated holes. The depth of the saturated holes in frames A and B is 21% and 19%, respectively. Note that the shape and spectral position of curves 1-6 depend on the cooling rate. The centroid of the Q_y hole minimum for sample 1s (blue data points) and sample 2f (red data points) is plotted as a function of fluence in the inset of frame B. It is apparent that hole position in a slowly cooled sample (1s) shifts faster (by a factor of 2) towards higher energies when compared with the fast-cooled sample (2f). This different behaviour is caused by a different degree of aggregation as these molecules were designed to self-assemble.[23]

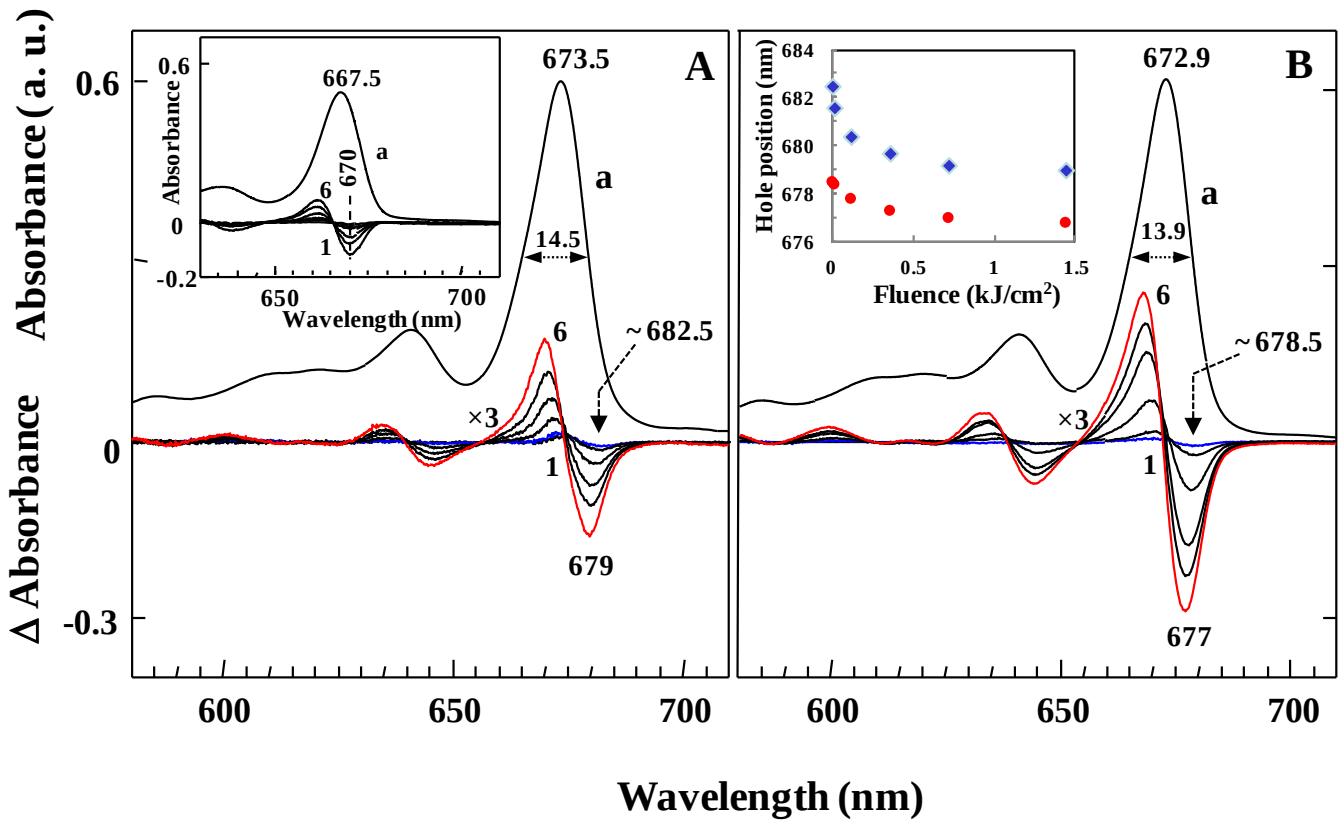

Figure 4-2 *Frame A:* **Curve a, shows the absorption spectrum of sample 1s at 5 K. Spectra labeled 1-6 are nonresonant holes obtained at various stages of hole burning (from low to high fluence) at a burning frequency of 496.5 nm. Inset in frame A shows absorption (curve a) and HB spectra (labeled 1-6) for M1 obtained under identical condition as that for sample 1s.** *Frame B*: **Absorption spectrum (curve b) and nonresonant holes (labeled 1-6) for fast-cooled sample (2f). For clarity, spectra labeled 1-6 in both frames are magnified by a factor of 3. Centroid of the Q_y hole minimum as a function of fluence for sample 1s (blue diamonds) and 2f (red circles) is plotted in the inset of frame B. Trefoil concentration, c~2×10^{-5} M; stoichiometric ratio of solvent (MTHF: C_2H_5OH ~1:200 v/v).**

Data presented in Figure 4-2 clearly show that sample 2f, with its blue-shifted absorption origin band and nonresonant HB spectra, has more contribution from ChlT1 monomers (i.e. it represents a less aggregated sample) than sample 1s. Note the difference in full-width-at-half-

maximum (fwhm) and HB characteristics. Spectral differences observed in frames A and B of Figure 4-2 are not surprising as a similar effect of cooling rate on absorption and emission spectra was previously observed for Chl *a* molecules.[44,50] For clarity of discussion, the following nomenclature is adopted below: monomer trefoils are labelled ChlT1 (as above), while different types of aggregates will be referred to as Ai (i = 1, 2, 3, 4) aggregates. For example, the aggregates with the most blue- and red-shifted origin bands are labelled as A1 and A4, respectively. We will argue below that both samples 1s and 2f consist of four types of aggregates, i.e. A1-A4, but their relative contribution is very different. A summary of the various aggregates formed in both types of samples, as well as the corresponding spectral band positions and relative contributions, are summarized in Table 4-1 (see also section 4.1 for discussion).

Table 4-1 Spectral characteristics and relative contribution of trefoils (ChlT1) and A1-A4 aggregates in slowly (1s) and fast-cooled (2f) samples at 5 K.

Pigment nomenclature and spectral maxima			**Relative contribution**	
Name	***Absorption (nm)***	***Fluorescence (nm)***	***Fast cooling***	***Slow cooling***
ChlT1	~676.5±1	678±1	**major**	minor
A1	a)	a)	minor	**moderate**
A2	~682.5±1	~685±1	very minor	**major**
A3	~703±2[b)]	~720±2	minor	minor
A4	c)	-	c)	c)

a) The maximum of the A1-type aggregates appears to be near 677 nm, although its exact position cannot be provided. Nevertheless, data shown in Figures 4-2 and 6 indicate that

A1 is present in both sample 1s and 2f but at different concentration. Trefoil-based A1 aggregates appear to be only slightly red-shifted in comparison to ChlT1, but they have a lower energy (0,0)-band than the A2 aggregates; see text for details.

b) The lowest excitonic state is near 710 nm, although the absorption peak appears to be ~703±2 nm; see Figure 4-3B.

c) The positive increase in absorption beyond 730 nm is an indication that such aggregates exist in minor amounts in both slow- and fast-cooling samples at 5 K; see Figure 4-3B. Absorption beyond 740 nm was not measured for these samples. Nevertheless, such aggregates are clearly revealed at room temperatures in water-based solvents (see Figure 4-5A).

The possible nature of all aggregates is discussed in section 4.2. For completeness, we add that absorption and HB spectra for monomer sample M1 (see inset of Figure 4-2A) were also measured at identical conditions as those for sample 1s. Since M1 consist of only one chlorophyll unit, its Q_y (0,0) origin band is significantly blue shifted, with an absorption maximum near 667.5 nm. In this case, as expected for isolated (non-interacting) pigments in a glassy matrix, the nonresonant hole does not shift with fluence. Below we focus on ChlT1 and its possible aggregates that could be used as artificial antenna systems in future photovoltaic devices.

The major contribution in sample 1s originates from A2 aggregate, and contributions from A1, A3, A4 in sample 2f are minor; therefore, the difference of two normalized saturated HB spectra obtained for samples 1s and 2f can reveal a contribution from ChlT1 in sample 2f. Such normalized saturated persistent HB spectra for samples 1s (curve a) and 2f (curve b) are re-plotted in Figure 4-3A. Curve c in frame A represents the difference between curves b and a, and

is assigned to the low-energy state of ChlT1 monomer (~676.5 nm). Saturated HB spectra (curves a and b from frame A) and corresponding absorption spectra (curves c and d, respectively) are shown with a longer wavelength range in frame B for comparison. The spectral feature peaking near 703 nm is an indication of a new type of aggregate, referred to below to as an A3 aggregate. To guide the eyes, the broad hole (*fwhm*~500 cm^{-1}) observed in curve a is fitted with an inverted Gaussian (curve e), peaking at ~710 nm and suggesting this is the position of the lowest energy

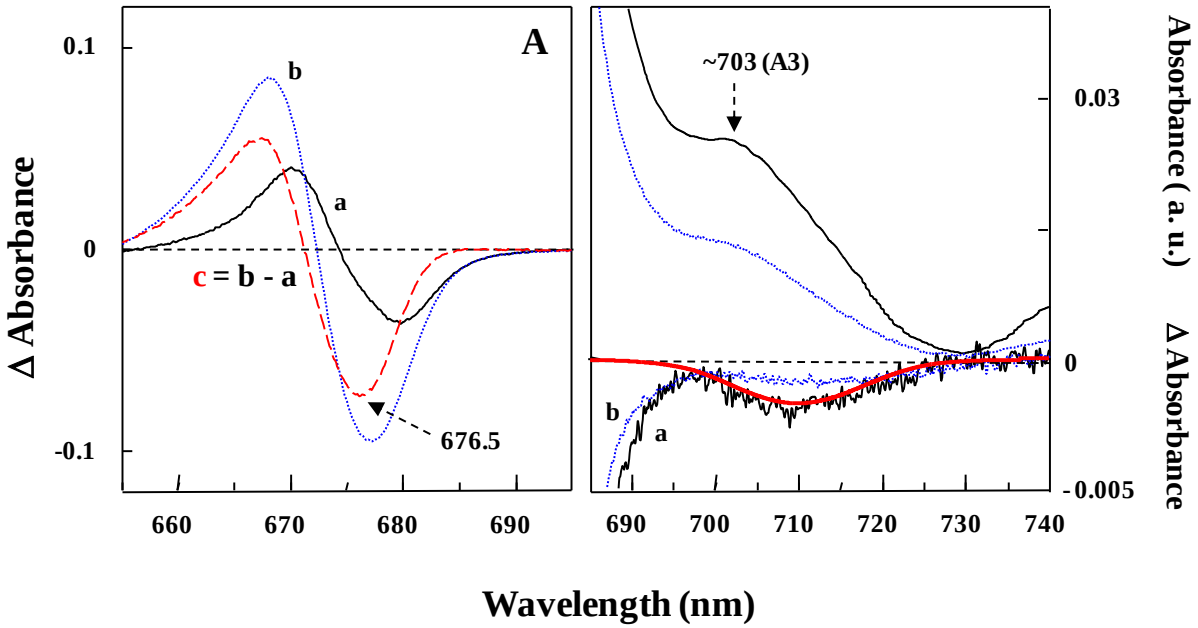

Figure 4-3 ***Frame A:*** **Saturated nonresonant HB spectra for samples 1s (spectrum a) and 2f (spectrum b) normalized at 685.0 nm. The difference between spectra a and b is shown as curve c.** ***Frame B:*** **Curves a and b are the saturated nonresonant holes obtained for samples 1s and 2f, respectively, in the longer wavelength range. Corresponding absorption spectra are shown for comparison. Simple Gaussian fit to the broad hole in curve a is shown as curve e.**

state in the type A3 aggregate. Interestingly, the absorbance doesn't go to zero beyond 730 nm, indicating the presence of another form of aggregate, labeled below as A4 (see also Figure 4-

5A). Proof that aggregates A1 and A2 also exist at low temperatures (even at relatively low ChlT1 concentrations) is provided in section 3.2.

At this point we turn to normalized fluorescence spectra obtained for samples 1s and 2f that are presented in Figure 4-4 as curves a and b. Note that the (0,0)-band in spectrum a is red-shifted by 6.5 nm in comparison with spectrum b; in addition, spectrum a shows an additional emission band near 720 nm as indicated by an asterisk. As expected, the emission maximum is red-shifted upon aggregation. Presence of similar emission bands was previously observed for special Chl *a* dimers (i.e. (Chla•H_2O)$_2$) in different solvents as demonstrated in Refs[45,53,54]. In the

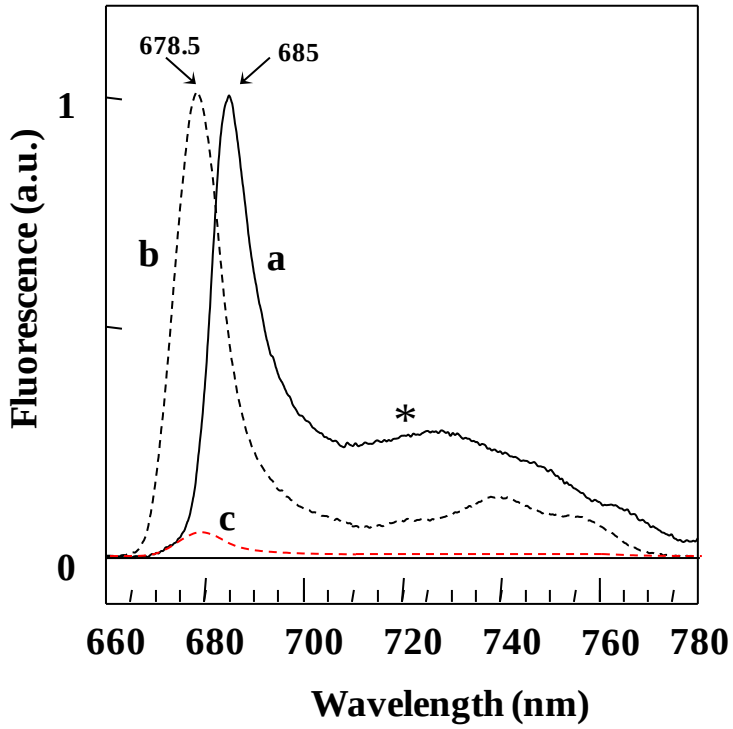

Figure 4-4 Curves a and b are normalized 5 K fluorescence spectra obtained for samples 1s and 2f, respectively. Both spectra were obtained at the same excitation wavelength of 496.5 nm with a laser power density of 0.5 mW/cm^2.

case of our trefoil samples, the ~720 nm emission band is assigned to type A3 aggregates—see section 4.2 for discussion. Based on the emission maximum in curve b (i.e. 678.5 nm) and the

position of the shallow nonresonant hole at the same wavelength (678.5 nm; curve 1 in frame B of Figure 4-2), we conclude that the fluorescence band with the (0,0)-band at 678.5 nm (curve b) is contributed to by trefoils (ChlT1; major contribution) and type A1 aggregates (minor contribution). Hole position and relative blue shift as a function of fluence strongly depend on the degree of aggregation. The emission maximum near 685 nm is assigned to type A2 aggregates, but a small contribution from ChlT1 monomer and A1 aggregates cannot be excluded as shown by spectrum c, which corresponds to spectrum b scaled by a factor of 0.08. (Note that HB and fluorescence quantum yields in case of aggregates may not be same, so their relative contributions may differ).

4.3.2 Room temperature study

To confirm whether the abovementioned aggregates, i.e. A1-A4, observed in low-temperature spectra are formed at room temperature, we measured the absorption spectra of ChlT1 samples at 298 K with a varying stoichiometric ratio of water. Results are presented in Figure 4-5A. The observed change in spectral position, band width, and relative absorption intensity with an increased concentration of water (see curves a-d; with d having the largest concentration of water) is apparent. The continuous increase in absorbance in the longer wavelength region clearly indicates formation of various aggregates. Similar behaviour was previously observed for aggregated Chl *a* molecules.[46] It appears that all four types of aggregates mentioned above are present. It is interesting to note A4 (~740 nm) and A3 (~700 nm) types of aggregates are preferentially formed with an increase in water concentration. Figure 4-5B shows the resonance Raman spectrum obtained for trefoils embedded into the MTHF:ethanol:water mixture (1:45:45 v/v) to provide more insight into the aggregation process; see section 4.2 for discussion.

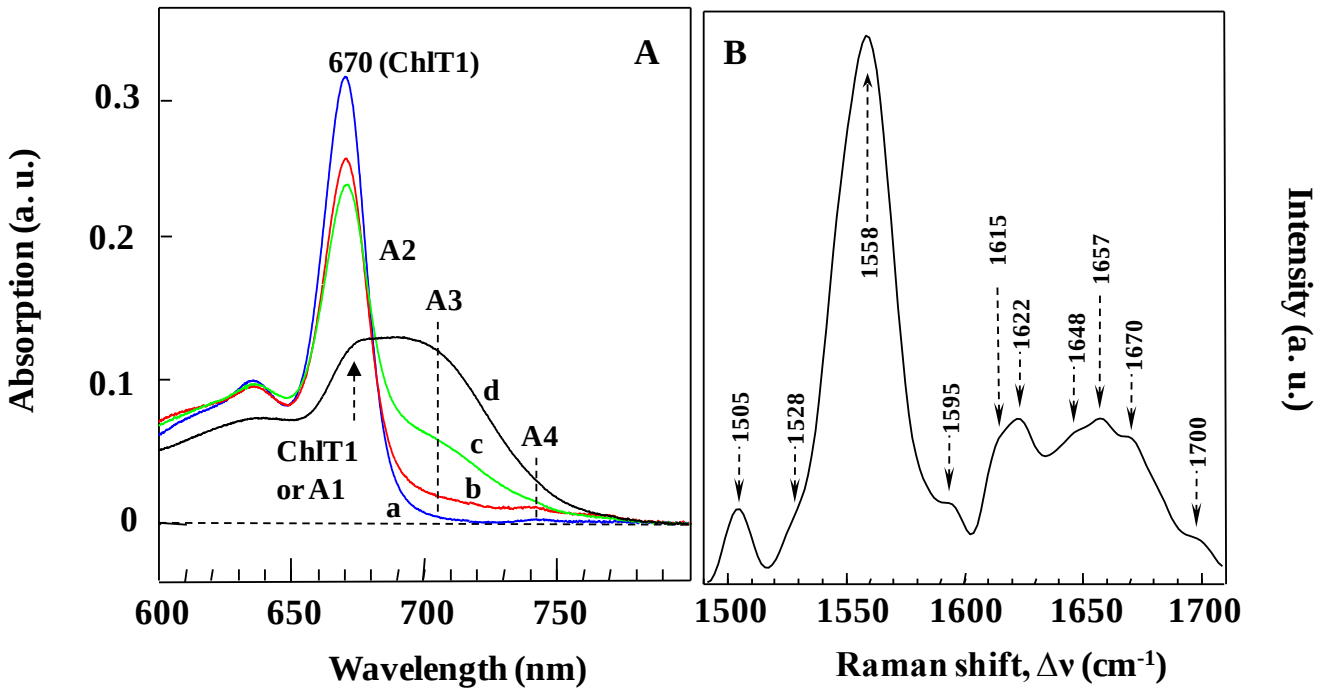

Figure 4-5 ***Frame A:*** **Spectral changes observed in the absorption spectrum of trefoils with an increasing amount of water at T = 298 K. In spectra a-d, the solvent stoichiometry reported as H_20:C_2H_5OH:MTHF (v/v) was 0:16:1, 2:14:1, 3:13:1, 8:8:1, respectively. The trefoil concentration was ~1.5×10^{-5} M.** ***Frame B*****: Resonant Raman spectrum of a trefoil sample (~10^{-4} M) prepared in a H_20:C_2H_5OH:MTHF (45:45:1 v/v) mixture.**

4.3.3 ZPH action spectra

ZPH action spectroscopy[42,43] allows investigation of the position of the lowest energy state of various molecular systems embedded in a glassy matrix at low temperatures. In this approach (absorption mode), the burn wavelength (λ_B) dependence of shallow (~10%) ZPH depth is measured under constant fluence.[42,43] Inverted ZPH holes obtained for samples 1s (blue) and 2f (red) at 5K are shown in figure 4-6A. Holes were burnt using a fluence of ~1 J/cm^2 at a resolution of 0.5 cm^{-1}. As expected, a comparison of the ZPH action spectra for the slow- and fast-cooled systems differ with deeper, narrower, and red-shifted holes observed for the slowly cooled sample (1s). The latter indicates different compositions of the low-energy state with

significantly lower contribution from trefoils. Estimated EET times using Eq. 4-1[40,41] (from the holewidths corrected for resolution) are plotted as a function of λ_B in frame B of Figure 4-6.

$$\Gamma_{hom} = (1/2\pi cT_1 + 1/2\pi c\tau_{EET}) + 1/\pi cT_2^* \approx 1/2\pi c\tau_{EET} \quad (4\text{-}1)$$

In Eq. 4-1: Γ_{hom} is the homogeneous linewidth (half-width at half-maximum of ZPH), T_1 is the fluorescence lifetime, T_2^* is the "pure" dephasing time, and τ_{EET} is the excitation energy transfer time.[40,41,43] For example, the ZPH width of 4.5 cm^{-1}, after correction for our resolution, corresponds to an EET time of ~2.5 ps.

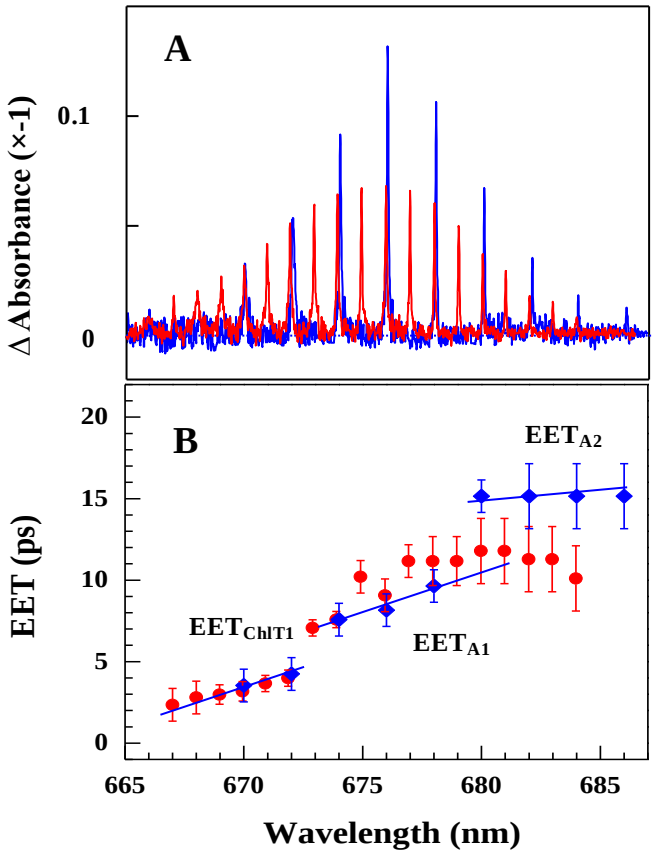

Figure 4-6 *Frame A*: Inverted zero-phonon-hole (ZPH) action-spectra for sample 1s (blue spikes) and sample 2f (red spikes) at T = 5 K. *Frame B:* Plot of EET times as a function of burning wavelength for samples 1s (blue data points) and 2f (red data points). Solid lines in panel B are to guide the eye.

Frame B of Figure 4-6 shows measured EET times for a slowly cooled sample (blue data points) and a fast-cooled sample (red data points). The slanted solid lines in frame B are to assist graph interpretation. Contributions from A3 and A4 aggregates in the matrix (MTHF: C_2H_5OH ~1:200 v/v) were too low to measure corresponding ZPH action spectra. Nevertheless, three distinct EET time regions within the 667-686 nm region indicate that EET dynamics depend on extent and type of aggregation (*vide infra*).

4.4. Discussion

4.4.1 Low-temperature absorption, HB, and fluorescence spectra

It is well known that Chls and Chl-like molecules are highly susceptible to aggregation. The level of aggregation depends primarily on concentration, temperature, and matrix composition.[44,45,50-53] However, cooling rate was also reported to affect the degree of aggregation and shape of optical spectra for Chl *a*, as reported in Refs.[44,50] Typically, red-shifted and broader absorption origin bands for Chl like molecules indicate aggregation.[44-54] This is clearly observed when the absorption spectrum in frame A of Figure 4-2 for sample 1s is compared with the absorption spectrum shown in frame B for sample 2f. The difference in sample composition is more pronounced when the nonresonant holes (curves 1-6) shown in frames A and B of Figure 4-2 are compared. Note the different hole positions for shallow and saturated holes. In addition, the blue shift of saturated holes in fast-cooled samples (2f) is a factor of ~2.3 smaller than that in sample 1s (for details see the inset of Figure 4-2). This clearly indicates that sample 1s consists mostly of A2 aggregates. Since the concentration of trefoils and aggregates is very small (*vide infra*), intermolecular EET between aggregates and trefoils can be excluded. Finally, bleaching of type A1 aggregate is not clearly visible in broad nonresonant HB

spectra, as A1 aggregates are expected to be weakly red-shifted in comparison with ChlT1 and its hole could overlap with the anti-hole of ChlT1 and A2 aggregates. That is, the energy difference between the lowest energy state of ChlT1 and A1 must be relatively small. However, it cannot be excluded that the larger hole shift is partially caused by modified excitonic interaction in the A2-type aggregate.

The aggregate labelled A3 (peaking near 703 nm) most likely represents a dimer of ChlT1 trefoils. Dimers of Chl *a* with similar origin bands were reported in the literature and depending on the nature of solvent composition, absorbed in the vicinity of 700-704 nm. [44,46,53,54] Different hole depths (see Figure 4-3B) near 710 nm in samples 1s and 2f clearly indicate different contributions from the A3 aggregates where larger contributions are seen in the slowly cooled sample. We suggest the ~710 nm state is the lowest excitonic state of A3 aggregates with emission significantly red-shifted to about 720 nm. Low-temperature emission from the A4 aggregate cannot be easily identified due to overlap with vibronic bands, although its absorption band near 740 nm has been clearly identified (see Figure 4-5A). Chl *a* aggregates with a similar origin band to the A4 aggregates were also reported in Refs.[45,53]. The possible nature of A1-A4 trefoil aggregates is discussed in section 4.2. In summary, regarding fluorescence spectra shown in Figure 4-4, we hasten to add that major contributions in spectra a and b originate from ChlT1 and A2 aggregates, respectively. Finally, we consider the A3 aggregate emission band near 720 nm (see Table 4-1 for details) and note that a similar emission band was reported for Chl *a* dimers[45,54] that showed ~725 nm fluorescence at 5 K

The shallowest hole in the fast-cooled sample (see curve 1 in Figure 4-2B) has the same position as that of the (0,0)-emission band. This indicates, as already mentioned above, the shallowest hole is contributed to by slightly red-shifted A1 aggregates; however, they are not

resolved in fluorescence spectra and exhibit relatively low fluorescence quantum efficiency when compared to trefoils (ChlT1). Thus we conclude that the fluorescence spectrum observed for fast-cooled samples is mostly contributed to by monomer trefoils (ChlT1), while the slowly cooled samples show emission from the A2 aggregate. The latter is also consistent with ZPH action spectra shown in Figure 4-6A.

4.4.2 Room-temperature study and nature of A1-A4 aggregates

Taken as a whole, data presented in Figure 4-5A establish that aggregation increases with water concentration. The absorption spectrum without water (spectrum a) appears to be weakly aggregated with an absorption maximum near 670 nm. The latter band is red shifted by ~5 nm in comparison to that reported in THF[23] at room temperature. This is caused by an increased polarity of ethanol in our matrix due to the solvatochromic shift. Comparison of spectra a-d reveals clearly that four types of aggregates (i.e. A1-A4) are continuously formed at the expense of the monomer trefoils. It is interesting to note the 740 nm band is already observed in spectra a and b. Due to the very large red shift of this absorption band, we assign such species to A4-type aggregates that correspond to oligomers with water or ethanol linkers leading to $(ChlT1{\bullet}H_2O)_n$ and/or $(ChlT1{\bullet}C_2H_5OH)_n$ nanostructures.

The broad feature around 700-705 nm also increases with water concentration; this type of aggregate (assigned to A3-type) could be due to strongly interacting ChlT1 in several different configurations; one of them (a symmetrical sandwich) is illustrated in Figure 4-7. Two possible linkers in our matrix may lead to the following types of A3 aggregates, i.e. $(ChlT1{\bullet}H_2O)_2$ and/or $(ChlT1{\bullet}C_2H_5OH)_2$. A3-type aggregates for Chl *a* molecules (with absorption near 700 nm) have also been observed and are well characterized in the literature.[45,46,48] Therefore, it is not surprising that such aggregates (with an origin band near 703 nm) are observed in our aggregated

trefoil samples. Certainly this type of association offers maximum stacking between chlorin macrocycles, so they are the most red-shifted dimers.

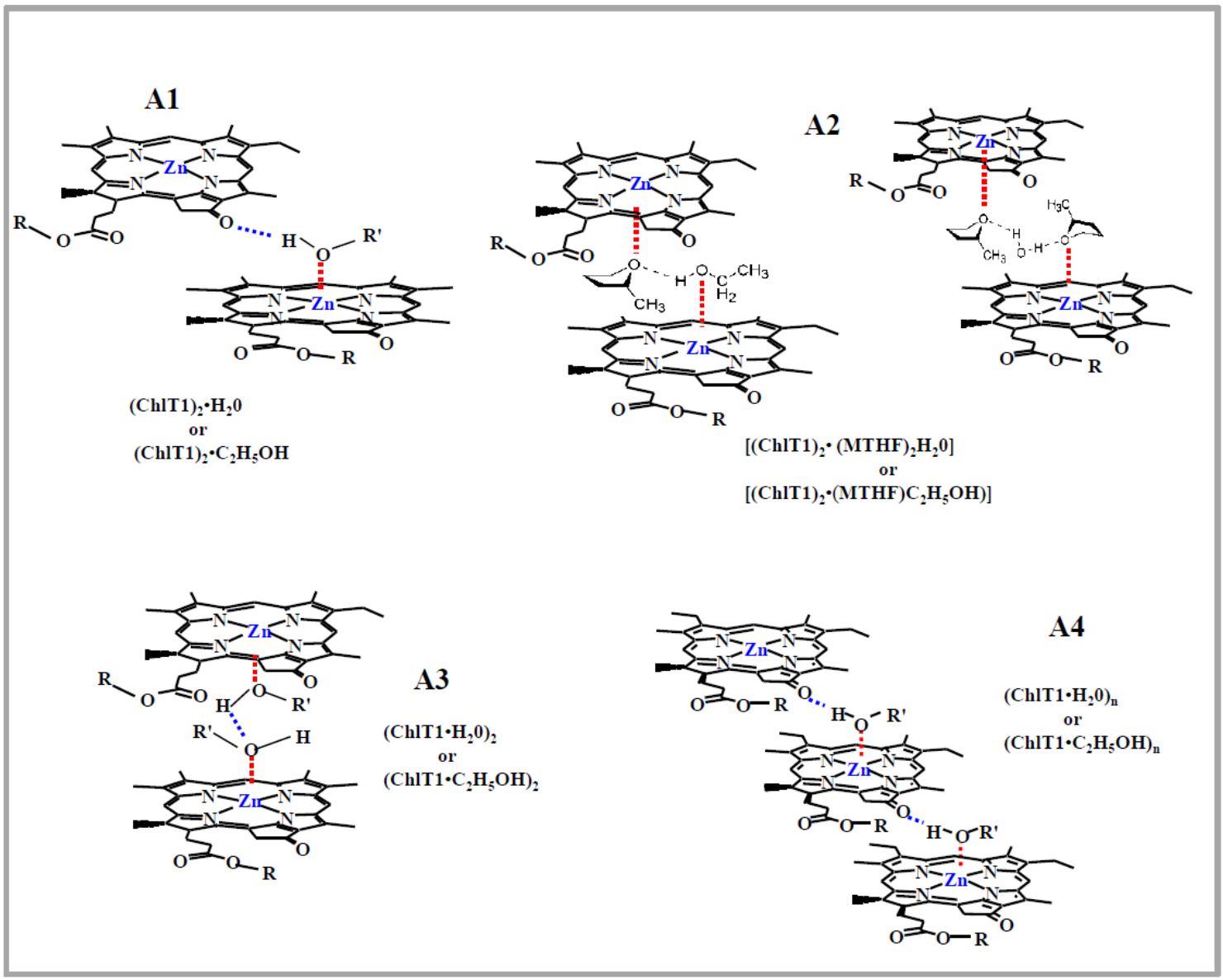

Figure 4-7 Possible nature of the A1-A4 aggregates. R′ could be either H or C_2H_5. R is the long hydrocarbon tail of a chlorophyll unit. For simplicity, only one subunit of each trefoil is shown to participate in aggregate formation. However, participation of multiple Zn-Chl units in aggregate formation is highly feasible.

Regarding the composition of A2-type aggregates, based on position of the absorption origin band, we propose a similar structure as that observed for Chl *a* aggregates formed in aqueous THF solution.[49] That is, we assume that A2-type aggregate, again with two different linkers [$(ChlT1)_2$•$(MTHF)_2H_2O$] or [$(ChlT1)_2$•$(MTHF)C_2H_5OH$], can be formed by direct link of the chlorin macrocycle centers as shown in Figure 4-7. The latter would lead to diminished stacking (due to a larger distance between macrocycles) and a smaller red shift of the origin band than that observed in A3-type aggregates, in agreement with our experimental observations.

Finally, we suggest that $(ChlT1)_2$•H_2O constitutes A1-type aggregate in which the –C=O group of zinc chlorin of one ChlT1 subunit is H–bonded to water and the water oxygen coordinates with the central zinc atom of the chlorin subunit belonging to next ChlT1 (see Figure 4-7). As a result, this type of aggregate does not have strong stacking interactions between the chlorin macrocycles, with a blue-shifted origin band in comparison with the A2-, A3-, and A4-type aggregates, in agreement with our assignment.

Since each ChlT1 molecule contains three identical Zn-Chls equally capable of forming aggregates, all of these subunits can be involved in aggregate formation leading to various types of aggregate configurations. Because of this complex aggregation pattern, ChlT1 studied in this work represent excellent building blocks for construction of large, functional photosynthetic antenna systems.

A Gaussian fit to room-temperature spectrum d of Figure 4-5 (not shown for brevity) also revealed five contributions: i) ChlT1 with a band near 670 nm; and ii) four types of aggregates A1, A2, A3, and A4 with origin bands near 673 nm, 682 nm, 701 nm, and 740 nm, respectively, although at different ratios, proving that these aggregates are also formed at room temperature.

Interestingly, similar band positions were also observed at room and low temperatures for various aggregates of Chl *a* molecules in different solvents.[44-54]

Additional support for aggregation of ChlT1 can be obtained from the resonance Raman (RR) spectrum shown in Figure 4-5B. As demonstrated above, most of the ChlT1 should be aggregated in our solvent mixture (MTHF, ethanol, and water 1:45:45 v/v), given our trefoil concentration. Regarding the RR spectrum, we are specifically interested in four features of the 1640-1700 cm^{-1} modes that describe the frequency of the –C=O stretching mode. Based on literature data,[51] one could suggest the feature near 1700 cm^{-1} originates from a free –C=O group whereas strongly downshifted modes, i.e. ~1670, 1657, and 1648 cm^{-1}, originate from hydrogen-bonded –C=O groups. Both water and ethanol are capable of H-bonding with keto carbonyl groups. A keto carbonyl hydrogen bonded via water (–C=O---HOH) is expected to be most downshifted, so we suggest that 1648 cm^{-1} mode is an indicator of the $(ChlT1{\bullet}H_2O)_n$-type aggregate (i.e. A4). It was reported in Ref.[51] that $(Chl{\bullet}2H_2O)_n$ aggregates possess the stretching frequency of keto carbonyl near 1645 cm^{-1}, in agreement with our assignment. Presence of 1657 and 1670 cm^{-1} bands in the Raman spectrum is also consistent with formation of A4 and A1 aggregates with ethanol (–C=O---HOC_2H_5) and H_2O/ethanol linkers, respectively.

4.4.3. ZPH action spectra and EET times

Presence of deeper zero-phonon holes (see blue spikes in Figure 4-6A) in the spectral range 675-685 nm in a slowly cooled sample (1s) is consistent with the relatively stronger absorption near 682.5 nm, as observed in Figure 4-2A. EET times for samples 1s and 2f vary from about 2.5-11.0 ps (red data points in frame B of Figure 4-6) and 2.5-15.0 ps (blue data points), respectively. Interestingly, EET time is slower at longer wavelengths, i.e. where type A1 and A2 aggregates contribute. Resonant holes burned in the 667-686 nm range revealed that EET time in the region

where mostly ethynyl-linked chlorophyll trefoils (ChlT1) contribute is ultrafast (~2.5 ps), at least at liquid helium temperatures, in agreement with femtosecond transient spectroscopy measurements obtained at room temperature where an EET time of 1.8 ps was observed.[23] A slowly cooled sample has more A2 aggregates where EET time is slower (i.e. about ~15 ps). In the region where there are several contributing assemblies, i.e. in the 670-680 nm spectral range, intermediate EET time values are observed depending on the aggregates' composition. Note that EET time in A1 and A2 aggregates decreases only by a factor of about 5–7 with respect to that observed for monomer trefoils. Apparently donor-acceptor distance and relative orientation of their transition dipoles are responsible for the observed difference in EET between ChlT1 and type A1 and A2 aggregates. This most likely is the reason why observed EET times are strongly dependent on the burning wavelength. These results are consistent with data presented in Figures 4-2, -3, and -4. It is of interest to note that the ultrafast EET times in ChlT1, A1, and A2 aggregates are comparable to that observed in various natural photosynthetic antennae.[33-36,42,43,55-62] We hasten to add that ultrafast EET time in trefoils can have, as discussed in Ref.[23], both through-bond[63] and through-space[64]) contributions. Note that through space (Förster) EET originates from the dipole-dipole approximation of the Coulombic interactions. If the donor-acceptor distance is relatively short and the coupling between chromophores is weak, excitation energy can hop from donor to acceptor site through space. This type of EET can be described by the Förster theory.[64] Through bond EET (Dexter type[63]) requires sufficient overlap of the electronic wavefunctions and is observed at relatively shorter distances than Förster EET. In case of ChlT1 monomer the inter-chromophore distance is ~15 Å so, one expects to have weak coupling matrix elements and, as a result, relatively slow Förster EET. However chromophores in ChlT1 are coupled via a rigid linker allowing a significant contribution from Dexter EET.

In general, EET in ChlT1 can be understood as exciton hopping from one to another subunit. However, in ChlT1 aggregates, several possible EET pathways can exist, as summarized in Figure 4-7. A simple model shown in Figure 4-8 further illustrates possible pathways of EET in A1-, A2- and/or A3-type aggregates. In this figure, Zn-Chls belonging to the same trefoils are

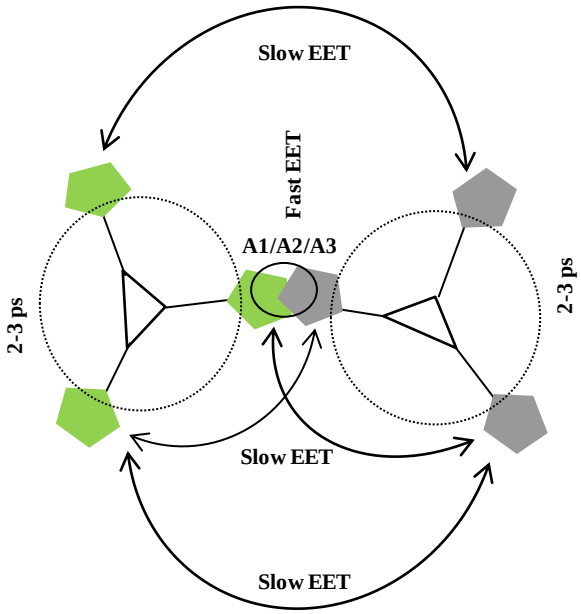

Figure 4-8 Possible model of EET in ChlT1 aggregates; Zn-Chls and rigid linkers are represented by pentagons and triangles, respectively. Zn-Chls belonging to same trefoil are shown in same color.

shown in the same color. EET time between Zn-Chls belonging to the same trefoil is indicated by dotted circles. EET time can be fast because chromophores are coupled via a rigid linker and due to a relatively short (~15 Å) distance between the donor and acceptor. Most likely this EET time slows down when one (or all) of the subunits is (are) engaged in formation of A1/A2/A3 aggregates and could be slower in comparison to EET time observed in a monomer trefoil. EET between zinc subunits belonging to two different trefoils involved in aggregate formation (as indicated by a small solid circle) can still be fast due to a relatively short donor-acceptor

distance. That is, as reported in Ref.[48] for Chl *a* dimers, analogous to our A3-type aggregate, the center-to-center Chl distance is only about 6.5 Å. In the case of A1 and A2 aggregates this distance can be larger than 6.5 Å but still short enough to allow a fast through space EET. Long-range (slow) EET pathways (through space) are also possible as indicated by double-sided solid arrows in Figure 4-8. These pathways seem feasible, at least in terms of distance, as donor-acceptor distance between Zn-Chls can be larger than 15 Å for noncovalently linked moieties. Time scale of the abovementioned EET pathways could be very different if two or three Zn-Chl subunits are involved in aggregate formation. In addition, presence of different facial isomers and hence different EET pathways cannot be excluded. In fact, the range of EET times (see Figure 4-6B) is consistent with several contributions. We note that very fast and very slow EET times reported in[65] for ChlT2 aggregates (using time-domain spectroscopy) are also consistent with the large range of the EET times observed in this work.

4.5. Conclusions

It has been shown that ChlT1 trefoil (consisting of three identical Zn-Chls) is capable of aggregate formation. Four types of aggregates (A1-A4) were identified in matrices with an increasing concentration of water. Aggregation is consistent with Raman spectra where multiple, significantly downshifted –C=O stretching bands were observed. It was shown that the degree of aggregation strongly depends on the rate of cooling. We conclude that fast-cooled samples contain a population of solvated trefoils (ChlT1) and A1/A2 aggregates, while slowly cooled samples are dominated by A2 aggregates with a smaller contribution from solvated ChlT1 and A1 aggregates. EET times obtained from ZPHs revealed three major groups of EET times consistent with the presence of a mixture of ChlT1, A1, and A2 aggregates. The latter is

consistent with absorption, emission, and nonresonant HB spectra. The EET time in ChlT1 is ~2.5 ps and slows down by a factor of 5-7 in A1- and A2-type aggregates. These fast EET times observed in A1 and A2 aggregates are of interest because they are comparable to those observed in various natural photosynthetic antenna complexes.[33-36,43] In this regard, we predict the trefoil studied in this work, in suitable solvents, will form three-dimensional building blocks capable of very efficient EET (research in progress). It is anticipated that such building blocks – mimicking natural photosynthetic antenna systems – could be used in future photovoltaic devices.

Acknowledgement

This work was supported by the DOE EPSCoR (DE-FG02-08ER46504) grant (RJ) and in part by the State of Kansas through the Kansas Technology Enterprise Corporation. Work at Northwestern University (MRW) was supported by the Division of Chemical Sciences, Office of Basic Energy Science, DOE under Grant no. DE-FG02-99ER14999. We also acknowledge Dr. Bret Flanders (Department of Physics, KSU) for the measurement of the resonant Raman spectra of a trefoil samples.

References

(1) Witt, H. T.; Müller, A.; Rumberg, B. *Nature* **1963**, *197*, 987-991.

(2) Barber, J. *Q. Rev. Biophys.* **2003**, *36*, 71-89.

(3) Fromme, P. *Photosynthetic Protein Complexes: A Structural Approach*, Wiley-VCH VerlagGmbH&Co. KGaA: Berlin, Germany, 2008; pp 1-100.

(4) Blankenship, R. E. *Molecular Mechanisms of Photosynthesis*; Blackwell Science Ltd.: London, 2008; pp 42-95.

(5) D'Souza, F.; Smith, P. M.; Zandler, M. E.; McCarty, A. L.; Itou, M.; Araki, Y.; Ito, O. *J. Am. Chem. Soc.* **2004**, *126*, 7898-7907

(6) Lee, A. J.; Ensign, A. A.; Krauss, T. D.; Bren, K. L. *J. Am. Chem. Soc.* **2010**, *132*, 1752-1753.

(7) Hindin, E.; Kirmaier, C.; Diers, J. R.; Tomizaki, K.; Taniguchi, M.; Lindsey, J. S.; Bocian, D. F.; Holten, D. *J. Phys. Chem. B* **2004**, *108*, 8190-8200**.**

(8) Yatskou, M. M.; Koehorst, R. B. M.; van Hoek, A.; Donker, H.; Schaafsma, T. J.; Gobets, B.; van Stokkum, I.; van Grondelle, R. *J. Phys. Chem. A* **2001**, *105*, 11432-11440.

(9) Nakamura, Y.; Hwang, I.-W.; Aratani, N.; Ahn, T. K.; Ko, D. M.; Takagi, A.; Matsumoto, T.; Kim, D.; Osuka, A. *J. Am. Chem. Soc.* **2005**, *127*, 236-246.

(10) Luo, C.; Guldi, D. M.; Imahori, H.; Tamaki, K.; Sakata, Y. *J. Am. Chem. Soc*. **2000**, *122*, 6553-6551.

(11) Kobuke, Y. *Eur. J. Inorg. Chem*. **2006**, 2333-2351.

(12) Imahori, H.; Fukuzumi, S. *Adv. Funct. Mater*. **2004**, *14*, 525-536.

(13) Noy, D.; Moser, C. C.; Dutton, P. L. *Biochimica et Biophysica Acta* **2006**, *1757*, 90-105.

(14) Kamat, P. V. *J. Phys. Chem. C* **2007**, *111*, 2834-2860.

(15) Barbour, L. W.; Hegadorn, M.; Asbury, J. B. *J. Am. Chem. Soc*. **2007**, *129*, 15884-15894.

(16) Forrest, S. R. *MRS Bulletin* **2005**, *30*, 28-32.

(17) Gledhill, S. E.; Scott, B.; Gregg, B. A. *J. Mater. Res*. **2005**, *20*, 3167-3179.

(18) Huijser, A.; Savenije, T. J.; Kotlewski, A.; Picken, S. J.; Siebbeles, L. D. A. *Adv. Mater*. **2006**, *18*, 2234-2239.

(19) Samuel, A. P. S.; Co, D. T.; Stern, C. L.; Wasielewski, M. R. *J. Am. Chem. Soc*. **2010**, *132*, 8813-8815.

(20) Wasielewski, M. R. *J. Org. Chem*. **2006**, *71*, 5051-5066.

(21) Garg, V.; Kodis, G.; Chachisvilis, M.; Hambourger, M.; Moore, A. L; Moore, T. A.; Gust, D. *J. Am. Chem. Soc*. **2011**, *133*, 2944–2954.

(22) Terazono, Y.; Kodis, G.; Bhushan, K.; Zaks, J.; Madden, C.; Moore, A. L; Moore, T. A.; Fleming, G. R.; Gust, D. *J. Am. Chem. Soc*. **2011**, *133*, 2916–2922.

(23) Kelley, R. F.; Tauber, M. J.; Wasielewski, M. R. *Angew. Chem. Int. Ed*. **2006**, *45*, 7979-7982.

(24) Fenna, R. E.; Matthews, B. W. *Nature* **1975**, *258*, 573-577.

(25) Hu, X.; Ritz, T.; Damjanović, A.; Autenrieth, F.; Schulten, K. *Q. Rev. Biophys.* **2002**, *35*, 1-62.

(26) Jordan, P.; Fromme, P.; Witt, H. T.; Klukus, O.; Saenger, W.; Krauβ, N. *Nature* **2001**, *411*, 901-917.

(27) Liu, Z.; Yan, H.; Wang, K.; Kuang, T.; Zhang, J.; Gui, L.; An, X.; Chang, W. *Nature* **2004**, *428*, 287-292.

(28) Guskov, A.; Kern, J.; Gabdulkhakov, A.; Broser, M.; Zouni, A.; Saenger, W. *Nat. Struct. Mol. Biol.* **2009**, *16*, 334-342.

(29) Loll, B.; Kern, J.; Saenger, W.; Zouni, A.; Biesiadka, J. *Nature* **2005**, *438*, 1040-1044.

(30) Brixner, T.; Stenger, J.; Vaswani, H. M.; Cho, M.; Blankenship, R. E.; Fleming, G. R. *Nature* **2005**, *434*, 625-628.

(31) Groot, M.; Frese, R. N.; de Weerd, F. L.; Bromek, K.; Pettersson, A.; Peterman, E. J. G.; van Stokkum, I. H. M.; van Grondelle, R.; Dekker, J. P. *Biophys. J.* **1999**, *77*, 3328-3340.

(32) Prokhorenko, V. I.; Holzwarth, A. R. *J. Phys. Chem. B* **2000**, *104*, 11563-11577.

(33) Renger, T.; Schlodder, E. *ChemPhysChem* **2010**, *11*, 1141-1153.

(34) Hughes, J. L.; Prince, B. J.; Krausz, E.; Smith, P. J.; Pace, R. J.; Riesen, H. *J. Phys. Chem. B* **2004**, *108*, 10428-10439.

(35) Dang, N. C.; Zazubovich, V.; Reppert, M.; Neupane, B.; Picorel, R.; Seibert, M.; Jankowiak, R., *J. Phys. Chem. B* **2008**, *112*, 9921-9933.

(36) Neupane, B.; Dang, N. C.; Acharya, K.; Reppert, M.; Zazubovich, V.; Picorel, R.; Seibert, M.; Jankowiak, R. *J. Am. Chem. Soc.* **2010**, *132*, 4214-4229

(37) Rätsep, M.; Pieper, J.; Irrgang, K.D.; Freiberg, A. *J. Phys. Chem. B* **2008**, *112*, 110-118.

(38) Berlin, Y.; Burin, A.; Friedrich, J.; Köhler, J. *Phys. L. Rev.* **2007**, *4*, 64-89.

(39) Lee, J.-E.; Yang, J.; Gunderson, V. L.; Wasielewski, M. R.; Kim, D. *Phys. Chem. Lett*. **2010**, *1*, 284-289.

(40) Moerner, W. E. *Topics in current physics, Persistent spectral hole burning: Science and applications*; Springer-Verlag: New York, 1987; pp 1-19.

(41) Jankowiak, R.; Hayes, J. M.; Small, G. J. *Chem. Rev* **1993**, *93*, 1471-1502.

(42) Purchase, R.; Völker, S. *Photosynth. Res.* **2009**, *101*, 245-266.

(43) Jankowiak, R.; Reppert, M.; Zazubovich, V.; Pieper, J.; Reinot, T. *Chem. Rev*. **2011** (in press).

(44) Cotton, T. M; Loach, P. A.; Katz, J. J; Ballschmiter, K. *Photochem. Photobiol*. **1978**, *27*, 735-749.

(45) Fong, F. K.; Koester, V. J. *Biochimica et Biophysica Acta* **1976**, *423*, 52-64.

(46) Fong, F. K.; Koester, V. J. *J. Am. Chem. Soc*. **1975**, *97*, 6888-6890.

(47) Fong, F. K.; Wassam, W. A. *J. Am. Chem. Soc*. **1977**, *99*, 2375-2376.

(48) Koester, V. J.; Fong, F. K. *J. Phys. Chem*. **1976**, *80*, 2310-2312.

(49) Uehara, K.; Hioki, Y.; Mimuro, M.; *Phtochem. Photobiol*. **1993**, *58*, 127-132.

(50) Brody, S. S.; Broyde, S. B. *Biophys. J*. **1968**, *8*, 1511-1533.

(51) Koyama, Y.; Umemoto, Y.; Akamatsu, A. *J. Mol. Struct*. **1986**, *146*, 273-287.

(52) Agostiano, A.; Cosma, P.; Trotta, M.; Monsù-Scolaro, L.; Micali, N. *J. Phys. Chem. B* **2002**, *106*, 12820-12829.

(53) Koester, V. J.; Polles, J. S.; Koren, J. G.; Galloway, L.; Andrews, R. A.; Fong. F. K. *J. Lumin*. **1976**, *12/13*, 781-786.

(54) Kooyman, R. P. H.; Schaafsma, T. J.; Kleibeuker, J. F. *J. Photochem. Photobiol*. **1977**, *26*, 235-240.

(55) Melkozernov, A. N.; Bibby, T. S.; Lin, S.; Barber, J.; Blankenship, R. E. *Biochemistry* **2003**, *42*, 3893-3903.

(56) Riley, K. J.; Zazubovich, V.; Jankowiak, R. *J. Phys. Chem. B* **2006**, *110*, 22436-22446.

(57) Damjanović, A.; Vaswani, H. M.; Fromme, P.; Fleming, G. R. *J. Phys. Chem. B* **2002**, *106*, 10251-10262.

(58) Thangaraj, B.; Jolley, C. C.; Sarrou, I.; Baltema, J. B.; Greyslak, J.; Whitelegge, J. J.; Lin, S.; Kouřill, R.; Subramanyam, R.; Boekema, E. J.; Fromme, P. *Biophys. J*. **2010**, *99*, 1-9.

(59) Feng, X.; Neupane, B.; Acharya, K.; Zazubovich, V.; Picorel, R.; Seibert, M.; Jankowiak, R. *J. Phys. Chem. B, 2011*(submitted).

(60) Pawlowicz, N. P.; Groot, M.-L.; van Stokkum, I. H. M.; Breton, J.; van Grondelle, R. *Biophys. J.* **2007**, *93*, 2732-2742.

(61) Franken, E. M.; Neerken, S.; Louwe, R. J. W.; Amesz, J.; Aartsma, T. J. *Biochemistry* **1998**, *37*, 5046-5051.

(62) Milder, M. T. W.; Bruggemann, B.; van Grondelle, R.; Herek, J. L. *Photosynth. Res*. **2010**, *104*, 257-274.

(63) Dexter, D. *J. Chem. Phys.* **1953**, *21*, 836-850.

(64) Förster, T. *Ann. Phys. (Leipzig)* **1984**, *2*, 55-75.

(65) Gunderson, V. L.; Conron, S. M. M.; Wasielewski, M. R. *Chem. Commun*. **2010**, *46*, 401-403.

Chapter 5 - Conclusions and Future Directions

This dissertation reports low-temperature frequency domain study on the CP43′ complex isolated form Cyanobacterium *synechocystis* PCC 6803, Zn-RC and β-Zn-RC mutant from *Rhodobacter spheroides*, and a chlorophyll trefoil.

In Chapter 2, electronic structure and excitation energy transfer (EET) pathways in isolated intact CP43′ protein complex was investigated using a combination of various HB approaches, low-temperature absorption and fluorescence measurements. It was shown that the CP43′ complex possesses two quasi-degenerate trap states A′ and B′ analogous to the CP43 protein. Various low-temperature optical spectra were fitted using an uncorrelated EET model taking into to account of possible intra monomer EET. It was suggested that for the optimal energy transfer from CP43′ to PSI, the low energy chlorophylls that belong to the A′ and B′ states should face towards PSI core. This suggestion is consistent with the model earlier proposed by Nield et al. (*Biochem*istry **2003**, *42*, 3180), but is inconsistent with the recently published model by Zhang et al. (*Biochim. Biophys. Acta* **2010**, *1797*, 457). At the present time, due to lack of high resolution crystal of PSI-CP43′ complex, our low temperature data cannot be fitted by accounting the detail excitonic effects. In future, having atomic coordinates of various pigments of CP43′ form the crystal structure, excitonic calculations can be performed to fit low temperature optical spectra that can provide still more insight on the nature of low-energy states. Various spectroscopic techniques (including the study presented in this dissertation) have proven that the PSI-CP43′ supercomplex is very efficient in terms of charge separation, so this complex could be directly used as a model system in designing bio-solar cell.

In Chapter 3, resonant and nonresonant photochemical HB approaches were used to study electronic structure of the charge separating P870 state of Zn-RC and Zn-β-RC mutant. It was shown that the two samples have similar P870* life times of about 1 ps. From this result it was argued that the coordination state of the H_A site zinc bacteriochlorophyll does not tune the active branch electron transfer. However, the quantum efficiency of charge separation in mutant decreases by 60 %. It was suggested that this difference is due to increased charge recombination in the Zn-β-RC mutant. Experimentally determined heterogeneity was used to fit various optical spectra which provided more reliable electron-phonon coupling parameters for the P870 state of the two reaction centers. One of the key findings of this is that the shoulder present on low

energy side of the Q_y B-band in low-temperature absorption spectra is not an upper excitonic component of the P870 but originates from the Q_y transition of B_B BChl. Right now, Zn-RC and Zn-β-RC crystal structures are not known. However, crystallization is on progress. Fitting the various low temperature optical spectra, knowing the atomic coordinates, accounting for the excitonic interaction can be done in future. The clear answer for complete disappearance of Q_x B-band in Zn-β-RC can be given only from crystal structure. It was suggested by van Brederode et al. (*Biochemistry* **1997**, *36*, 6856) from pump-probe experiment that two different pathways of charge separation exist in *Rb. sphaeroides* WT-RC with P870 (one pathway) or B_A (other pathway) acting as primary electron donor. Recent pump-probe experiment by Romero et al. (*Biochemistry* **2010**, *49,* 4300) also suggests that similar pathways are operational in PSII RC. However, such pathways of charge separation (if exist) have not been explored as yet by frequency domain approaches like HB. Assuming similar arrangement of co-factors, these pathways may exist even in Zn-RCs. Preliminary data obtained via PHB of Zn-β-RC suggest that multiple pathways of charge separation could be explored via HB using two laser experiments. Further experiments are needed before any conclusions could be reached.

In Chapter 4, low-temperature HB, fluorescence, and absorption spectra were used to investigate electronic structure, EET and aggregation pattern in a novel artificial antenna system ChlT1. It was found that EET at 5 K is very fast and is ~2 ps. Room temperature absorption and Raman spectra further confirmed that ChlT1 indeed forms at least four different types of aggregates. It was shown that EET in A1 and A2 aggregates slows only by a factor of 5-7. It is believed that ChlT1 and aggregates can serve as nice artificial antenna in future solar cells.

Appendix A - The CP43 Proximal Antenna Complex of Higher Plant Photosystem II Revisited: Modeling and Hole Burning Study (I)

This work is published in the *J. Phys. Chem. B* 2008, *112*, 9921

Nhan C. Dang, Valter Zazubovich, Mike Reppert, Bhanu Neupane, Rafael Picorel

Michael Seibert, and Ryszard Jankowiak

Abstract

The CP43 core antenna complex of Photosystem II is known to possess two quasi-degenerate "red"-trap states (R. Jankowiak *et al. J. Phys. Chem.* B 2000, 104, 11805). It has been suggested recently (V. Zazubovich and R. Jankowiak, *J. Lum.* 2007, 127, 245) that the site distribution functions (SDFs) of the red states (*A* and *B*) are uncorrelated and that narrow holes are burned in the subpopulations of chlorophylls (Chls) from states *A* and *B* that are the lowest-energy Chl in their complex and previously thought not to transfer energy. This model of uncorrelated excitation energy transfer (EET) between the quasi-degenerate bands is expanded by taking into account both electron-phonon and vibrational coupling. The model is applied to fit simultaneously absorption, emission, zero-phonon action, and transient hole burned (HB) spectra obtained for the CP43 complex with minimized contribution from aggregation. It is demonstrated that the above listed spectra can be well fitted using the uncorrelated EET model, providing strong evidence for the existence of efficient energy transfer between the two lowest energy states *A* and *B* (either from *A* to *B* or from *B* to *A*) in CP43. Possible candidate Chls for the low-energy *A* and *B* states are discussed, providing a link between CP43 structure and spectroscopy. Finally, we propose that persistent holes originate from regular NPHB

accompanied by the redistribution of oscillator strength due to excitonic interactions, rather than photoconversion involving Chl-protein hydrogen bonding as suggested before (J.L. Hughes *et al.*, *Biochemistry* 45, 12345, 2006). In the accompanying paper (II) it is demonstrated that the model discussed in this manuscript is consistent with excitonic calculations, which also provide very good fits to both transient and persistent HB spectra obtained under non-line narrowing conditions.

Conclusions

Absorption, emission, zero-phonon action, and transient HB spectra can be well fitted by allowing for energy transfer between the two lowest energy bands *A* and *B* in CP43. In this model (*B*1*A*1), fluorescence, zero-phonon action, and transient HB spectra can be represented by a sum of the sub-ensembles of the CP43 complexes where either of the two low-energy bands may be the lowest-energy state incapable of downhill energy transfer. Our results are consistent with ~10 ps EET from state *B* to state *A* in CP43. EET in a particular complex is possible either from *A* to *B* or from *B* to *A*. The shape of the transient spectrum is an inverted image of the absorption spectrum of a sub-ensemble of B_s-type and A_s-type pigments, respectively, which are the lowest-energy pigments in their complexes. We have demonstrated that the major emission band originates from sub-bands A_s and B_s, while the absorption spectrum is contributed to by the "true" *A* and *B* bands. We have also proposed that the high-energy photoproduct in persistent HB spectra originate from regular NPHB accompanied by the redistribution of oscillator strength due to modified post-burn excitonic interactions. We have argued that the photoconversion process (suggested to occur via tunneling between alternate configurations of the C=O---H–protein hydrogen bond when the molecule is in the excited state (J.L. Hughes *et al.*, *Biochemistry* 45, 12345, 2006), while feasible, is not required to account for the strong positive absorption

increase in the saturated HB spectra. Finally, based on the above discussion, it appears that the best candidates from the 13 Chls of the CP43 complex that mostly contribute to the *B* band are Chls 34, 37, and 46, while Chls 41 and 44 are likely to contribute to the *A* band. However, definite assignments cannot be made based on this data alone. The choice of Chls contributing to the low energy states can be further narrowed by simultaneous fitting of the absorption and emission spectra and transient/persistent HB spectra using excitonic calculation as demonstrated and discussed in detail in part II (M. Reppert *et al*. *J. Phys. Chem. B* 2008, 112, 9934).

Appendix B - An Alternate Model of PSI- CP43′ Supercomplex

The model of the PSI- CP43′supercomplex proposed by Zhang *et al.*[1] is shown in Figure S-1. For brevity, only one PSI monomer and seven CP43′monomers are shown. The PSI Chls are represented by green or black circles. Among the black ones, M1, PL1, and A21 are connectors between the adjacent PSI monomers, and all others stand for the PSI pigments that are possible acceptors of energy transferred from the CP43′ monomers.[2] The thirteen chlorophylls in CP43′ identified by Loll *et al.*[3] are labeled in the CP43′ monomer #1 using the numbering according to PDB file 2AXT. The squares filled with red in the CP43′ complex show the 14th pigment identified by Ferreira *et al.*,[4] which was not found in Ref.[3] The green triangles represent the 15th pigments, added by Zhang *et al.*[1] based on modeling studies. We hasten to add that the very recent (higher resolution, 1.9 Å) X-ray data of CP43 complex of Umena *et al.*[5] did not reveal two additional Chl discussed above. The possible energy transfer paths between two neighboring CP43′ monomers, based on Ref.[1], are shown as an example, with lines connecting some of the pigments of CP43′ monomer #4 and its neighbors.

By rearranging the relative positions of the CP43′ monomers and the PSI trimer and calculating the energy-transfer potential, Zhang *et al.*[1] claimed that their optimal model is both an efficient light harvester under low-light conditions and an efficient energy dissipater under excessive high-light conditions. Based on their modeling, Zhang *et al.*[1] suggested that there are 15 Chl pigments in each CP43′monomer, two more than the number in its homologous equivalent, CP43 complex of PSII.[3,5] Another difference between the models of Nield *et al.*,[2] discussed in the main body of our paper, and that of Zhang *et al.*[1] is the relative positions of Chls in respect to the PSI trimer. Namely, in the model of Zhang *et al.*[1] Chls assigned by us to the

lowest-energy states are located on the periphery of the CP43′ ring. Assuming that our assignment, based on excitonic calculation of various types of optical spectra[6,7] is correct, we suggest that the arrangement of Chls in the model of Niled *et al.*[2] is more realistic, because if the the Chls contributing to the lowest-energy states were located far from the PSI pigments, the EET from CP43′ ring to the PSI trimer would be very inefficient.

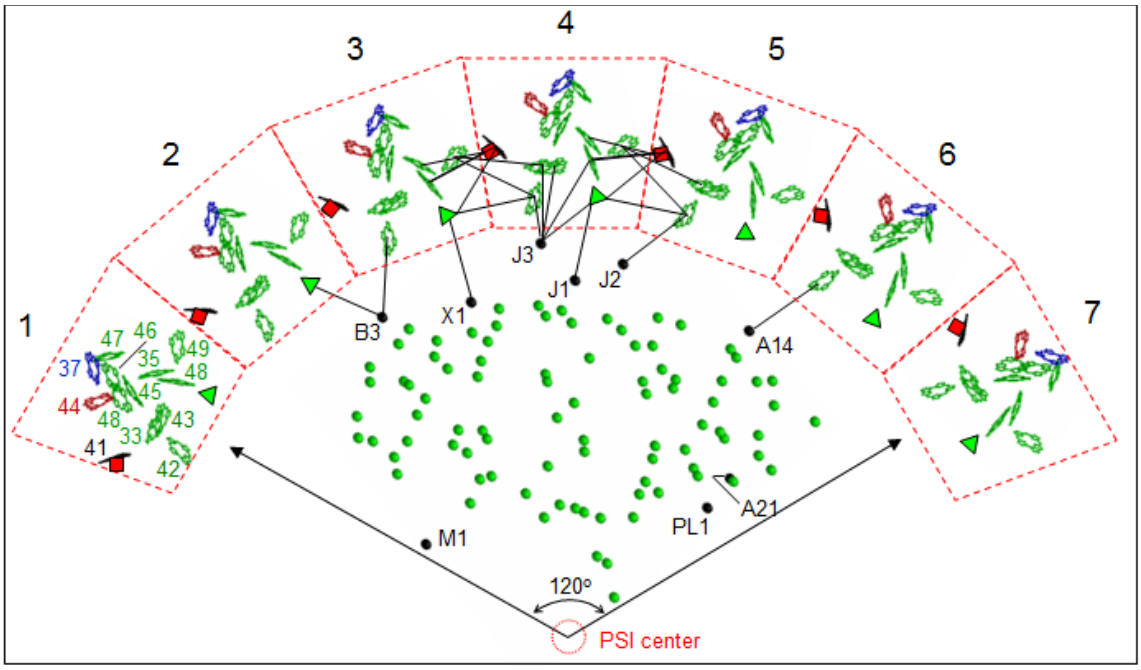

Figure S-1 Pigment organization of the PSI-CP43′ supercomplex in the model proposed by Zhang *et al.*[1] Only one PSI monomer and seven CP43′ monomers are shown for brevity. The pigments in CP43′ monomer #1 are labeled based on the notation of Ref.,[3] and the notation for the PSI pigments are given based on Ref.[8] The black solid lines stand for possible EET paths between PSI and CP43′ complexes and between CP43′ monomers. For clarity, EET paths between monomer #4 and its neighbors are shown as an example for EET between CP43′ monomers.

REFERENCES

(1) Zhang, Y.; Chen, M.; Church, W. B.; Lau, K. W.; Larkum, A. W. D.; Jermiin, L. S. *Biochim. Biophys. Acta* **2010**, *1797*, 457-465.

(2) Nield, J.; Morris, E. P.; Bibby, T. S.; Barber, *J. Biochem.* **2003**, 42, 3180-3188.

(3) Loll, B.; Kern, J.; Saenger, W.; Zouni, A.; Biesiadka, J. *Nature* (London, U. K.) **2005**, *438*, 1040-1044.

(4) Ferreira, K. N.; Maghlaoui, T. M.; Barber, J.; Iwata, S. *Science* **2004**, *303*, 1831-1838.

(5) Umena, Y.; Kawakami, K.; Shen, J. -R.; Kamiya, N. *Nature* **2011**, 473, 55-60.

(6) Dang, N. C.; Zazubovich, V.; Reppert, M.; Neupane, B.; Picorel, R.; Seibert, M.; Jankowiak, R. *J. Phys. Chem. B* **2008**, *112*, 9921-9933.

(7) Zazubovich, V.; Jankowiak, R. *J. Lumin.* **2007**, 127, 245-250.

(8) Jordan, P.; Fromme, P.; Witt, H. T.; Klukas, O; Saenger, W; Krauss, N *Nature* **2001**, *411*, 909-917.